DISSERTATION

USING GOES-16 ABI DATA TO DETECT CONVECTION, ESTIMATE LATENT HEATING, AND INITIATE CONVECTION IN A HIGH RESOLUTION MODEL

Submitted by

Yoonjin Lee

Department of Atmospheric Science

In partial fulfilment of the requirements

For the Degree of Doctor of Philosophy

Colorado State University

Fort Collins, Colorado

Spring 2021

Doctoral Committee:

Advisor: Christian D. Kummerow
Co-Advisor: Milija Zupanski

Michael M. Bell
V. Chandrasekar
Christine Chiu

ABSTRACT

USING GOES-16 ABI DATA TO DETECT CONVECTION, ESTIMATE LATENT HEATING, AND INITIATE CONVECTION IN A HIGH RESOLUTION MODEL

Convective-scale data assimilation has received more attention in recent years as spatial resolution of forecast models has become finer and more observation data are available at such fine scale. Significant amounts of observation data are available over the globe, but only a limited number of observations are assimilated in operational forecast models in the most effective way. One of the most important observation data for predicting precipitation is radar reflectivity from ground-based radars as it provides three-dimensional structure of precipitation. Many operational models use these data to create cloud analysis and initiate convection. In High-Resolution Rapid Refresh (HRRR), the cloud permitting operational model at National Oceanic and Atmospheric Administration (NOAA) that is responsible for short term forecasts over the Contiguous United States (CONUS), latent heating is derived from ground-based radars and added in the observed convective regions to initiate convection. Even though adding heating is shown to improve forecasts of convection, this cannot be done over ocean or mountainous regions where radar data is not available.

Geostationary data are available regardless of radar coverage and its data are provided in similar spatial and temporal resolution as ground-based radar. Currently, geostationary data are only used as a source of cloud top information or atmospheric motion vectors due to lack of vertical information. However, Geostationary Operational Environmental Satellites (GOES)-16 and -17 have high temporal resolution data that can compensate the lack of vertical information.

From loops of one-minute visible images, convective clouds can be detected by finding a region with a constant bubbling. Therefore, this dissertation seeks a way to use these high temporal resolution GOES-16 data to mimic what radars do over land.

In the first two papers presented in the dissertation, two methods are proposed to detect convection using one-minute GOES-16 Advanced Baseline Imager (ABI) data. The first method explicitly calculates T_b decrease or lumpiness of reflectance data and finds convective regions. The second paper tries to automate this process using machine learning method. Results from both methods are comparable to radar product, but the machine learning model seems to detect more convective regions than the conventional method.

In the third paper, latent heating profiles for convective clouds are estimated from GOES-16. Once a convective cloud is detected, latent heating profiles corresponding to cloud top temperature of the convective cloud is searched from the lookup table created using model simulations. This technique is similar to spaceborne radar inferred latent heating developed for National Aeronautics and Space Administration (NASA)'s Global Precipitation Measurement Mission (GPM). Latent heating assigned from GOES-16 is shown to be similar to latent heating derived from Next-Generation Radar (NEXRAD) once they are summed up over each cloud.

Finally in the last paper, latent heating estimated by using the method from the third paper are assimilated into the Weather Research and Forecasting (WRF) model to examine impacts of using GOES-16 derived latent heating in initiating convection in the forecast model. Two case studies are presented to compare results using GOES-16 derived heating and NEXRAD derived heating. Results show that using GOES-16 derived heating sometimes produce deeper convection than it should, but it improves overall precipitation forecasts. This appears related to the much deeper column of heating assigned by GOES than the empirical

relation used by the HRRR operational scheme. In addition, in a case when storms developed over Gulf of Mexico where radar data are not available, forecasts are improved using GOES-16 latent heating.

ACKNOWLEDGEMENTS

First of all, I would like to express my deep and sincere gratitude to my two advisors, Prof. Christian Kummerow and Dr. Milija Zupanski for giving me a chance to study and learn in this wonderful environment and all the insightful guidance that led me become a better scientist as well as a better person. I would like to thank my committee members Prof. Christine Chiu, Prof. Michael Bell, Prof. V Chandrasekar for taking their time to serve on my committee and their valuable feedback on my dissertation. I extend my thanks to Prof. Imme Ebert-Uphoff for encouraging me in many ways especially during this pandemic.

The Kummerow research group always has been the biggest support and help throughout this process. They are the ones that I met on an everyday basis, and I have always enjoyed and been inspired by our fruitful discussions. I feel lucky to have these people as my collegues.

I also thank my friends, especially Jungmin Park and Heejung Jeon for bringing me joy whenever I'm down. Lastly, I thank my family for their endless love and support.

TABLE OF CONTENTS

CHAPTER 1: INTRODUCTION

1.1 Motivation

Numerical weather prediction models have experienced tremendous improvements over the past decades. Such improvements have been possible due to increased computing power and better quality of observation data (Bauer et al., 2015). Despite significant improvements on the forecast model side, observation data is still required to guide the model into the right direction as the weather systems are highly non-linear, and accurate initial conditions are essential. Furthermore, as the regional forecast models can now resolve convective processes, data assimilation at convective scale has become important for an accurate precipitation forecast.

Various observations are assimilated in NOAA's operational models, RAP and HRRR, to achieve accurate precipitation forecast. RAP is a model run with a spatial resolution of 13km and provides boundary condition for HRRR, which has finer spatial resolution of 3km. During an assimilation cycle, RAP combines data from ground-based radar, meteorological aerodome reports (METARs), and geostationary satellite to create cloud analysis, and radar-derived latent heating is used through digital filter initialization to force the model to form convective clouds where they are observed. Latent heating derived from reflectivity fields is used again in HRRR to initiate convection. Although ground-based radar reflectivity is one of the main observations used for convective-scale DA as it provides three-dimensional structure of precipitation, its data are restricted by the availability of radars. The quality of radar data degrades over mountainous regions, and ground-based radars are not available beyond the immediate coast of the United States. Since the southern part of the United States is often affected by storms forming over the

Gulf of Mexico, it would be beneficial to have latent heating data over those regions that are similar to what ground-based radar offers over land.

Geostationary satellite is the only option since it has similar spatial and temporal resolutions as ground-based radar, and its data are available over the entire hemisphere. However, in spite of being available everywhere, its use has been limited due to lack of vertical information especially in presence of thick clouds. Usually in the forecast model, its data are only used as a source of cloud top information or atmospheric motion vectors. Nevertheless, recent progress in data assimilation has been achieved by including these cloud-affected observation data (Pincus et al., 2011).

The Geostationary Operational Environmental Satellite (GOES) series are geostationary satellites over CONUS operated by NOAA. Since the first launch of GOES-1 in 1975, GOES series have continuously observed weather system over CONUS, and provided useful environmental data from space. Current operational GOES series, GOES-16 and -17, can be much more useful than their predecessors as they have higher spatial and temporal resolutions. Mesoscale sector, one of three scan sector used when active convection threatens the United States, has a temporal resolution of one minute, and one of visible bands has the finest spatial resolution of 0.5km. With such high resolution, interesting weather events such as pyrocumulus cloud (red arrow in Figure 1.1) or convective clouds (blue arrows in Figure 1.1) are clearly observable from GOES-16 or -17, and from consecutive one-minute data, bubbling cloud top can be observed as clouds grow. Accordingly, lack of vertical information can be compensated by high temporal resolution of the data, and GOES-16 data can be used to mimic radars to help initiating convection in the forecast models. Therefore, this dissertation explores the use of high spatial and temporal resolution GOES-16 data in detecting convection, estimating latent heating

for convective clouds, and adding latent heating to convective regions in a short-term forecast model. Each result is compared to radar products to examine whether it has similar impacts so that it can be used in the regions without ground-based radar.

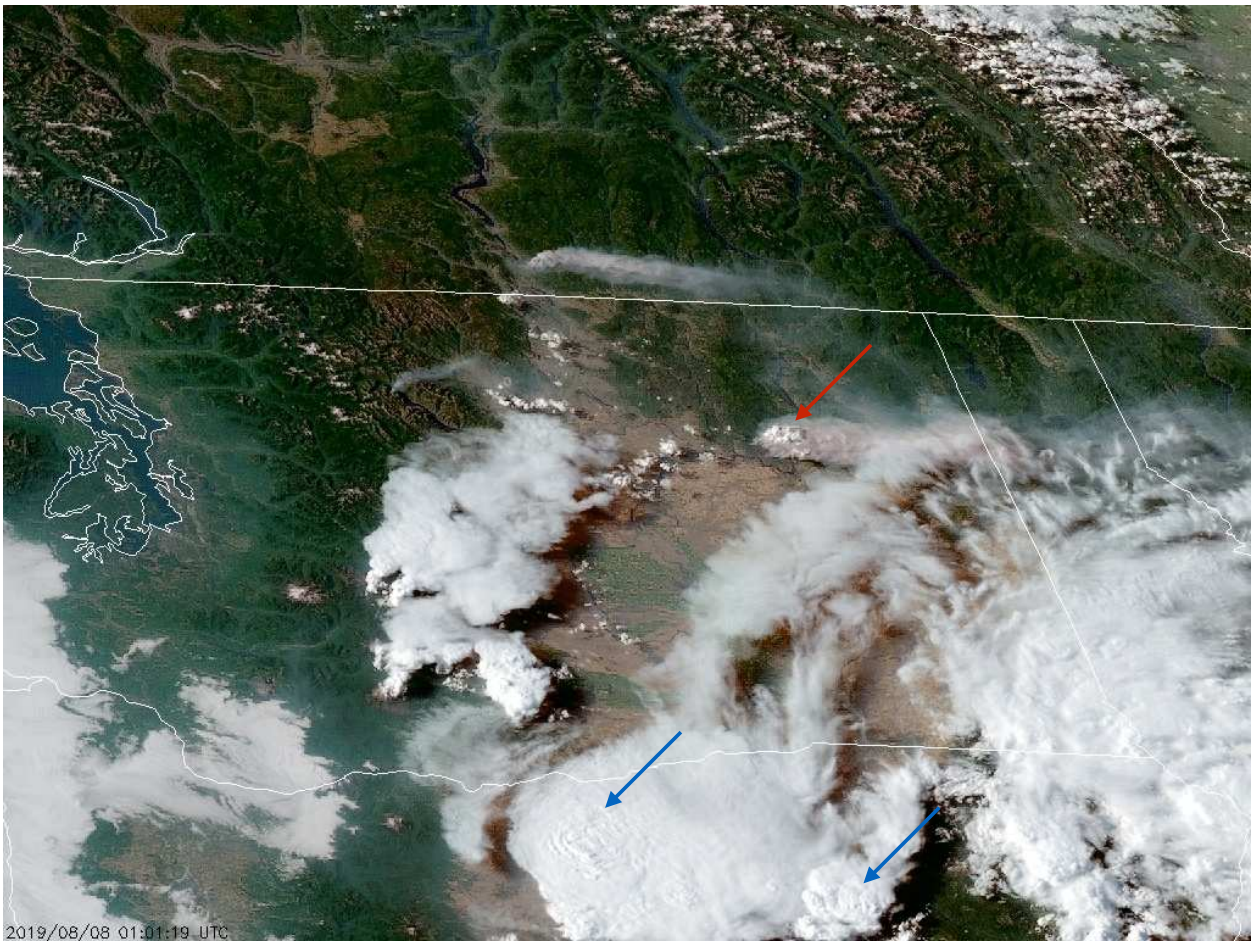

Figure 1 Pyrocumulus cloud (red arrow) and convective clouds (blue arrows) observed by GOES-17 on August 8th, 2019. (http://rammb.cira.colostate.edu/ramsdis/online/loop.asp?data_folder=loop_of_the_day/goes-16/20190808000000&number_of_images_to_display=100&loop_speed_ms=100)

1.2 Outline of dissertation

This dissertation consists of four papers that are either submitted or in preparation. The first paper presented in Chapter 2 proposes two methods to detect convection in early and mature stages using one-minute GOES-16 ABI data. For early convection, the method uses decrease in

T_b at two water vapor channels from ABI, and for mature convective clouds, the method uses high reflectance at channel 2, low brightness temperature at channel 14, and lumpy cloud texture calculated applying the Sobel operator on channel 2 reflectance data. The second paper in Chapter 3 tries to automate the detection process by using machine learning model. Unlike the first paper where it explicitly assigns thresholds to be used, the machine learning model is trained to find a spatial pattern of convective clouds in GOES-16 visible and infrared maps on its own without the use of artificial temperature or texture thresholds.

The third paper in Chapter 4 tries to estimate latent heating profiles for the convective regions detected by the methods from the first paper, and its profiles are compared to radar-derived products to examine if they have similar magnitude. Finally in Chapter 5, latent heating profiles obtained from the method developed in the third paper are added to the forecast model to initiate convection, and its impacts are evaluated. Its results are compared to results using radar-derived latent heating to see if heating from GOES-16 behaves similarly with radar-derived heating so that it can be used in regions without ground-based radar.

CHAPTER 2: A SIMPLIFIED METHOD FOR THE DETECTION OF CONVECTION USING HIGH RESOLUTION IMAGERY FROM GOES-16

2.1 Introduction

While weather forecast models have improved tremendously throughout the decades (Bauer et al., 2015), local scale phenomena such as convection remain challenging (Yano et al., 2018). Precipitation is especially hard to predict as numerical models struggle with initiating convection in the right location and intensity. To address this issue in short term predictions, many models now assimilate all-sky radiances and precipitation-related products where available (Benjamin et al., 2016; Bonavita et al., 2017; Geer et al., 2017; Gustafsson et al., 2017; Jones et al., 2016; Migliorini et al., 2018; Scheck et al., 2020). In some forecast models such as the High Resolution Rapid Refresh (HRRR) model in the United States, latent heating is added, along with precipitation affected radiances, to adjust model dynamics to correspond to the observed convection (Benjamin et al., 2016). Latent heating is only added in convective regions because local scale phenomena tend to develop first by convective clouds before detraining stratiform precipitation. In order to correctly detect convective regions and add heating as frequent as possible, ground-based radars have been used during the short-term forecast. However, ground-based radar data are not available over ocean or mountainous regions. Therefore, this study explores whether high temporal resolution data from recent operational geostationary satellite, Geostationary Operational Environmental Satellites (GOES) – R Series, can provide similar information as radar for the location of convection so that it can be used for initializing forecast models over regions without ground-based radar.

Convection is classically defined from in-cloud vertical air motions (Steiner et al., 1995). However, since vertical velocity is rarely measured directly, the radar community initially adopted radar reflectivity thresholds to define convection and distinguish it from stratiform precipitation (Churchill and Houze, 1984; Steiner et al., 1995). One problem with using reflectivity threshold is its sensitivity to the selected threshold for convection. If the threshold is set high, convective regions where precipitation has just begun are not captured, while a threshold that is set too low will misclassify some stratiform regions as convective. To address this issue, Churchill and Houze (1984) separated precipitation types by using the horizontal structure of precipitation fields (Steiner et al., 1995). They classified a grid point as convective if the grid point had rain rates twice as high as the average taken over surrounding grid points or had reflectivity over 40dBZ (~ 20 mm h^{-1}). Steiner et al. (1995) refined this method with three criteria: intensity, peakedness, and surrounding area. They used the same threshold of 40dBZ for intensity in the first step, but grid points with reflectivity greater than the average reflectivity within a radius of 11km as well as surrounding grid points are also classified as convective. Nonetheless, stratiform regions sometimes can have reflectivity values greater than 40dBZ. Zhang et al. (2008) used two reflectivity criteria for convective precipitation-namely that the reflectivity be greater than 50dBZ at any height and greater than 30dBZ at -10°C height or above. Zhang and Qi (2010) defines a grid point as convective if the vertically integrated liquid water exceeds a threshold of 6.5kg m^{-2}. Qi et al. (2013) developed a new algorithm that combined two previous methods from Zhang et al. (2008) and Zhang and Qi (2010). By combining these two methods and modifying the thresholds, they were able to decrease misclassification of stratiform regions with strong bright band features, but could still miss some convective regions in their initial stage due to a high reflectivity threshold. The HRRR model

uses a much lower reflectivity threshold of 28dBZ to detect convective regions and assigns a heating increment (Weygandt et al., 2016). While this is significantly lower than the thresholds discussed above, its primary purpose is to initiate convection where there is significant echo present, while relying on the model physics to assign the proper precipitation type.

While radars have been the preferred method for detecting convection, they are not the only instruments available. Visible (VIS) and infrared (IR) radiances also contain some information, although largely limited to cloud top properties. Convection detection algorithms using VIS and IR sensors exist for both convective initiation (CI) and mature stages. At the initial stages of convection, cloud tops grow vertically, and decrease in brightness temperature (T_b) is observed accordingly. Many algorithms use decreased cloud top temperature from the growth (related to the in-cloud vertical velocity) to detect convective regions from various geostationary satellites over the globe such as GOES (Sieglaff et al., 2011; Mecikalski and Bedka, 2006), Himawari-8 (Lee et al., 2017), and Meteosat (Autonès and Moisselin, 2010). Temporal trends of T_b are evaluated on several channels around water vapor absorption band or longwave infrared window band and combinations of these channels. Interest fields for CI include temporal trend of T_b at 10.7μm (or 11.2μm) to infer cloud top cooling rates, (3.9μm – 10.7μm) to infer changes in cloud top microphysics, and (6.5μm – 10.7μm) to infer cloud height changes relative to the tropopause (Mecikalski and Bedka, 2006). Main differences between the algorithms are tracking method of a cloud and time period used to calculate T_b change of the cloud. Clouds are usually tracked with atmospheric motion vectors or a simple overlap method, and temporal trends of T_b are calculated over 15 minutes.

Convective clouds in their mature stage cannot be detected by the abovementioned algorithms as their cloud tops do not grow much in the vertical, and T_b decrease is not a main

feature that is applicable to such clouds. Overshooting Top (OT) is one of the clear indications of mature convective clouds, and many existing algorithms used OT feature in such clouds. There are two common approaches to detect OTs: the brightness temperature difference method and the infrared window-texture method (Ai et al., 2017). The brightness temperature difference method uses a difference in T_b between the water vapor (WV) channel and IR window channel ($T_{b,wv} - T_{b,IR}$). Positive values of $T_{b,wv} - T_{b,IR}$ due to the forcing of warm WV from below into the lower stratosphere are used as an indicator of OTs (Setvak et al., 2007). However, since the threshold for the difference between two channels can depend on several factors, Bedka et al. (2010) suggested another method to detect OTs which is called the Infrared window-texture method. This method takes advantage of a feature of OT in that it is an isolated region with cold T_b surrounded by relatively warm anvil region (Bedka et al., 2010). This method, unfortunately, cannot avoid having to choose T_b thresholds that vary according to seasons or regions (Dworak et al., 2012). Bedka et al. 2016 tried to minimize the use of fixed detection criteria. They developed two OT detection algorithms based on IR and VIS channels, and an OT probability was produced through a pattern-recognition scheme. The pattern that the scheme looks for is protrusion through the anvil caused by strong updrafts. Another pattern that is obvious in mature convective clouds with or without OT is "lumpy surface" from constant bubbling (Mecikalski and Bedka, 2006). Cloud top texture in VIS and IR channels has been explored using Spinning Enhanced Visible and Infrared Imager (SEVIRI) on Meteosat-8 satellite in Zinner et al. 2008 and Zinner et al. 2013, respectively. In addition to evaluating spatial texture, Müller et al. (2019) explores spatio-temporal gradients of water vapor channels in SEVIRI to estimate updraft strength. This study suggests a different way to calculate spatial gradients of VIS channel in GOES-R to detect convection.

The use of VIS and IR sensors in detecting convection can benefit significantly with the launch of National Oceanic and Atmospheric Administration's (NOAA's) GOES-R Series which have high resolution, rapidly updating (i.e. 1 minute) imagery. This study makes use of this new data, namely the 1 minute data available from GOES-16 and GOES-17 in "mesoscale sectors" to update methods for detecting convection in different stages. Mesoscale sectors are manually moved around to observe interesting weather events. One is developed for CI using T_b from an IR channel in GOES-R. As in previous papers measuring clout top cooling rate, temporal trends of the data were used but, since GOES-R has high temporal resolution, ten consecutive data with 1-minute interval were used. It has been challenging to correctly track convective clouds with 15 or 30-minute interval data which have been used in previous studies due to changing shape of convective clouds and merging or splitting of clouds. However, since clouds do not change as much within one minute, using one-minute data eliminates some of the errors from cloud movements that needed to be dealt with in some previous studies, and cooling rate is calculated applying linear regression on 1-minute data over 10 minutes, rather than using T_b difference between 15 minutes. Another one is developed for mature convection using both reflectances from a VIS channel and T_b from IR channels. For this algorithm, lumpy and rapidly changing surface and high cloud top height from mature convective clouds were used to detect clouds both with and without OTs. Lumpiness is calculated using Sobel operator which is an edge detection filter in image processing, and the lumpiness is explored at each minute throughout 10 minutes to look for regions with continuous bubbling. These two methods were then combined to provide detection of convection in all stages. The above methods are not intended to replace ground-based radars where these are available. Instead, the focus here is complementing ground-based networks, either off-shore or other regions lacking coverage.

The datasets that were used to detect convection and validate the results are described in Sect. 2, while the methods used to identify initial and established convection are explained in Sect. 3. Sect. 4 highlights the results of each method. Two case studies were examined followed by a one-month statistical study to quantify the operational accuracy of the methods.

2.2 Data

2.2.1 The Geostationary Operational Environmental Satellite R series (GOES-R)

Earth-pointing instruments of GOES-R consist of the Advanced Baseline Imager (ABI) with 16 channels, and the Geostationary Lightning Mapper (GOES-R Series Data Book, 2019). GOES-16 is the first of the two GOES-R series satellites to provide data for severe weather forecast over the United States and surrounding oceans (Schmit et al., 2017). Both T_b and reflectance data from the ABI were used to detect convective regions. Mesoscale data with one minute temporal resolution were used to fully exploit its high temporal resolution of the new instrument.

Reflectance at 0.64μm (Channel 2) and T_b at 6.2μm (Channel 8), 7.3μm (Channel 10), and 11.2μm (Channel 14) were used in the study. Channel 2 is a "red" band with the finest spatial resolution of 0.5km. This fine spatial resolution is useful to resolve lumpy, or bubbling surfaces of clouds in their mature stage. Channel 2 reflectance data were normalized by solar zenith angle so that a single threshold can be used throughout the method regardless of locations of the sun. Channel 14 is an IR longwave window band, which is a good indicator of the cloud top temperature for cumulonimbus clouds (Müller et al., 2018). High reflectance and texture of the cloud top seen in channel 2 and cloud top height inferred from channel 14 are combined to determine locations of mature convective clouds.

Channel 8 and 10 are ABI water vapor channels with 2km spatial resolution. Because Channel 8 sees WV at somewhat higher altitudes than Channel 10, they can observe WV associated with updrafts as they progress upwards, and were therefore used to detect early convection.

2.2.2 Next Generation Weather Radar (NEXRAD) and Multi-Radar/Multi-Sensor (MRMS)

Multi-Radar/Multi-Sensor (MRMS) data developed at NOAA's National Severe Storms Laboratory were used for validation purposes. MRMS integrates the radar mosaic from the Next Generation Weather Radar (NEXRAD) with atmospheric environmental data, satellite data, lightning, and rain gauge observations to produce three dimensional fields of precipitation (Zhang et al., 2016). These quantitative precipitation estimation (QPE) products have a spatial resolution of 1km and temporal resolution of 2 minutes.

A "PrecipFlag" variable contained in the standard MRMS product classifies precipitating pixels into seven categories: 1) warm stratiform rain, 2) cool stratiform rain, 3) convective rain, 4) tropical–stratiform rain mix, 5) tropical–convective rain mix, 6) hail, and 7) snow. Details of the classification can be found in Zhang et al. (2016). It is a rather sophisticated classification of precipitation type as it not only uses reflectivity at various heights, but also takes into account vertically integrated liquid to distinguish convective core from stratiform clouds (Qi et al., 2013). A reduced set of these classes were used to validate the convective classification from GOES ABI data. In this study, warm stratiform rain, cool stratiform rain, and tropical-stratiform rain mix are all assigned a stratiform rain type while grid points with convective rain, tropical-convective rain mix, and hail are assigned a convective rain type. Along with the classification product, MRMS provides a variable called "Radar QPE quality index (RQI)". This product is

associated with quality of the radar data, which is a combination of errors coming from beam blockages and the beam spreading/ascending with range (Zhang et al., 2016). This flag is used to mask out regions with low radar data quality. Only data with RQI greater than 0.5 are used in this study.

2.3 Methodology

This study examines methods to detect convective clouds at each life stage. Convective clouds can be divided into actively growing clouds and mature clouds. Actively growing clouds are usually clouds at the initial stage that grow nearly vertically while mature clouds are capped, but continue to bubble due to the release of latent heat. They often move horizontally after they reach the tropopause. The proposed method to detect actively growing cloud is similar to previous CI studies mentioned in the introduction in the sense that the method uses temporal trends of T_b. The high temporal resolution data simplifies the method because the use of derived wind motion in tracking clouds is no longer necessary. One minute is short enough that cloud motion, at most, is to the adjacent grid points, and clouds can be easily tracked by focusing on overlapped scenes.

The method to detect mature convective clouds is similar to previous studies by Bedka et al. 2016 and Bedka et al. 2019 in terms of using the texture of the cloud top surfaces to infer strong updrafts. Cloud top surfaces of mature convective clouds are much bumpier than any other clouds, and their bumpiness is most evident in VIS images with the finest resolution. The following method uses horizontal gradients of reflectance to represent the bumpiness of cloud tops, and the magnitude of the gradients are used to distinguish convective cores from their anvil

clouds. Cloud top temperatures from channel 14 are used to eliminate low cumulus clouds that might appear bubbling.

2.3.1 Detection of actively growing clouds with brightness temperature data

In the early stage of convection, updrafts of water vapor eventually lead to condensation, the release of latent heat, and convective processes. Operational weather radars cannot observe small hydrometeors, but T_b decrease at water vapor absorption bands of GOES-ABI is observed when these small hydrometeors start to develop. During the early convective stages, T_bs that are sensitive to water vapor will decrease due to condensed cloud water droplets aloft generated by a strong updraft. Two ABI channels around the water vapor absorption bands, channel 8 (6.2μm) and channel 10 (7.3μm), were selected to cover water vapor updrafts at different height levels. These channels were used to find small regions consistent with developing clouds. If a cloud develops continuously for ten minutes and shows a large decrease in T_b over ten minutes in either channel, the cloud is determined to be convective.

To compute the T_b decrease in clouds, a window has to be defined as it is usually difficult to precisely define the boundary of clouds, especially at the early stages of convection. Since most of the early convective clouds are smaller than 10km in diameter, the window was defined as a 10km×10km box which is essentially a 5×5 matrix of satellite pixels consisting of 25 T_bs with 2km resolution. Considering the fact that a convective core usually has the lowest T_b within its neighborhood, the T_b matrix was formed around a pixel only if that pixel had the lowest T_b in the 5×5 matrix. However, this criterion alone could not distinguish convective cores from stratiform clouds and cloud edges which can also exhibit a local minimum. In addition to the lowest T_b, the shape of convective clouds is therefore also considered. As shown in the Figure

2.1a, convective clouds not only have the lowest T_b in their cores in all directions, but also have increasing T_bs away from the core, making their T_b distributions look like an inverted two-dimensional (2D) Gaussian distribution. To select T_b matrices that have this upside down Gaussian shape, an inverted 5×5 Gaussian matrix that has mean and standard deviation of the T_b matrix was created and compared with the T_b matrices. To focus the comparisons on the shape of the T_b distribution (Figure 2.1b), the maximum T_b found in the 5×5 matrix was subtracted from all values, and T_b values were divided by the difference between maximum and minimum T_b to normalize the T_b matrix itself. If the T_b matrix has a shape of a developing cloud (i.e. 2D upside down Gaussian), the absolute value of the difference between the T_b matrix and the upside down Gaussian matrix will be small. A threshold of 10 for this absolute value of the difference between T_b matrix and upside down Gaussian matrix (sum of residuals between normalized T_b and upside down Gaussian) was empirically determined to exclude non-convective scenes. T_b matrices with values greater than 10 are removed from the scene. This is done for all ten consecutive T_b images that are one minute apart. Continuous overlaps of T_b matrices for ten minutes imply that the cloud maintained a convective shape for ten minutes, and therefore, changes in T_b are calculated to assess if the cloud in the T_b matrices was growing. The minimum T_bs of the T_b matrices at each time step were linearly regressed against time to measure a decreasing trend. If the fitted line at each channel had a slope either smaller than -1K/min for channel 10 or -0.5K/min for channel 8, the grid point with the lowest T_b at each time step for ten minutes as well as the neighboring 8 grid points in the window were classified as convective. This procedure is summarized in a flowchart in Figure 2.2.

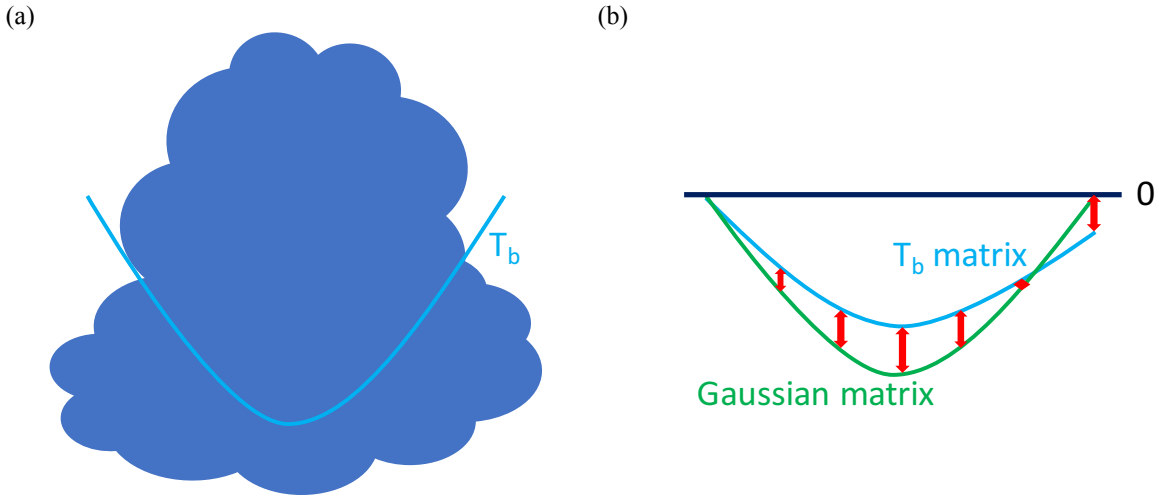

Figure 2.1 (a) A typical shape of a convective cloud and its T_b distribution around the convective core (blue line). (b) Schematic representation of distributions of the inverted Gaussian matrix (green) and the T_b matrix (blue) when the cloud is convective.

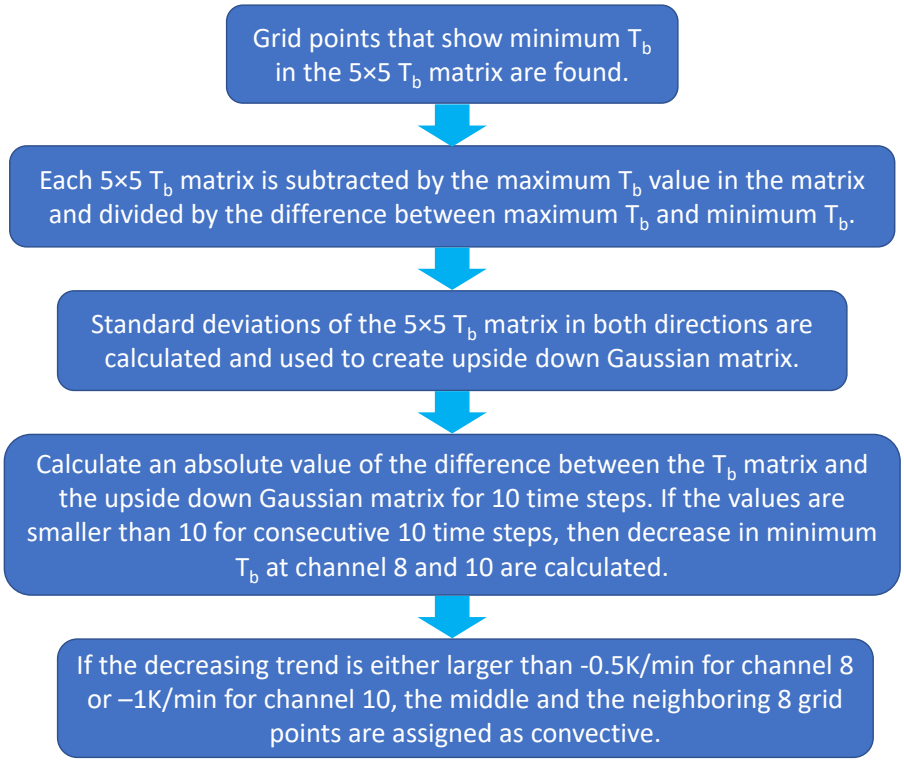

Figure 2.2 A flowchart to summarize the growing cloud detection method.

Water vapor channels have different sensitivity to water vapor, and thus, different values for the threshold are chosen for each channel (channel 8 and 10). Since growth rate can vary depending on the surrounding environment and different evolution stages, it is important to find an appropriate threshold that best represents growth rate for clouds in their early stages. These thresholds are chosen based on the analysis of one-month data during July of 2017. The 5×5 T_b windows that maintained the developing shape and had a decreasing trend of T_b during ten minutes are collected over the one month period. A total of 38293 and 97042 (for channel 8 and 10, respectively) 5×5 windows that show decrease in T_b were collected, and precipitation types from MRMS were assigned for each window. Future MRMS convective flags up to 20 minutes after the detection period were included in the analysis because some time delays were observed in MRMS product when assigning convective flags, especially for early convection. When comparing GOES products to future MRMS products, future locations of GOES products were calculated assuming convection moves at the same speed that clouds moved during the initial ten minutes. Tables 2.1 and 2.2 show results applying different thresholds ranging from -0.1K/min to -2.0K/min. For each row, 5×5 pixel windows that show larger temperature decrease than the corresponding threshold are collected, and they are analysed for potential convection. Numbers in the table represent the number of 5×5 windows that MRMS precipitation flags were assigned to either non-convective or convective at the corresponding 10-minute time window, as well as pixels that were flagged as convective by MRMS in the next 10 and 20 minutes to account for the fact that GOES can detect convection before the radar sees precipitation. However, not all the detection by the method is done early since MRMS product is rather good at detecting early convection as well. The overall accuracy in the last column is calculated by dividing the number of windows that were convective within 20 minutes (sum of convective, convective within 10

min, and convective within 20 minutes) by the total number of the windows (sum of non-convective, convective, convective within 10 min, and convective within 20 minutes). Some convective clouds in the early stage show smaller decreasing trend than the thresholds, but using a smaller value for the threshold can introduce clouds that do not grow into deep convective clouds in the end. Clouds that develop into deep convective clouds are eventually captured by these thresholds in later times as they show rapid intensification sooner or later. However, choosing a large cooling rate for the threshold will lead to less detection of convective clouds as not a lot of windows show large cooling rate. Therefore, thresholds of -0.5K/min and -1.0K/min for channel 8 and 10, respectively are chosen so that it detects reasonable amounts of convections. Cooling rate observed at channel 8 is smaller than channel 10 due to higher absorption at channel 8. Channel 8 senses moisture at higher altitude and thus, when water vapor starts to condensate at lower levels, it is less affected, and its T_b does not decrease as much as in channel 10. The matrix does not have to be detected at both channels, but using two channels tends to find the same vertically growing clouds over time by detecting the cloud using channel 8 first and then using channel 10 later. This method will be called as growing cloud detection method hereinafter.

Table 2.1. Number of non-convective, convective, convective within 10 minutes, and convective within 20 minutes for using different threshold values (channel 8)

Threshold value (K/min)	Non-convective	Convective	Convective within 10 min	Convective within 20 min	Overall accuracy
-0.1	3634	2911	250	89	47.2%
-0.2	740	2264	154	40	76.8%
-0.3	277	1831	117	28	87.7%
-0.4	153	1504	87	21	91.3%
-0.5	104	1266	87	16	92.8%
-0.6	67	1051	44	10	94.3%
-0.7	49	851	30	7	94.8%
-0.8	32	691	27	5	95.8%
-0.9	22	576	21	4	96.5%
-1.0	12	477	19	3	97.7%
-1.1	7	396	16	3	98.3%
-1.2	5	321	14	2	98.5%
-1.3	4	267	9	1	98.6%
-1.4	3	222	9	0	98.7%
-1.5	2	180	8	0	98.9%
-1.6	1	134	7	0	99.3%
-1.7	1	105	7	0	99.1%
-1.8	1	89	6	0	99.0%
-1.9	1	74	4	0	98.7%
-2.0	1	54	2	0	98.2%

Table 2.2. Number of non-convective, convective, convective within 10 minutes, and convective within 20 minutes for using different threshold values (channel 10)

Threshold value (K/min)	Non-convective	Convective	Convective within 10 min	Convective within 20 min	Overall accuracy
-0.1	21900	5041	1339	511	23.9%
-0.2	9225	3982	854	277	35.7%
-0.3	4357	3284	611	163	48.2%
-0.4	2241	2722	429	109	59.3%
-0.5	1234	2268	310	71	68.2%
-0.6	759	1954	233	40	74.6%
-0.7	479	1661	184	28	79.6%
-0.8	318	1430	139	22	83.3%
-0.9	219	1232	102	20	86.1%
-1.0	147	1050	75	14	88.6%
-1.1	103	893	64	11	90.4%
-1.2	77	758	56	10	91.5%
-1.3	55	657	42	9	92.8%
-1.4	41	556	34	5	93.6%
-1.5	28	461	29	5	94.6%
-1.6	17	393	25	3	96.1%
-1.7	14	340	24	3	96.3%
-1.8	11	297	21	2	96.7%
-1.9	9	255	19	2	96.8%
-2.0	5	207	19	1	97.8%

Furthermore, it is interesting to note that some clouds did not produce precipitation even with rapid growth over -2.0K/min (for channel 10). This would be due to mixing between convective cells and their dry environment or highly non-linear nature of chances of precipitation.

2.3.2 Detection of mature convective clouds with reflectance data

Mature convective clouds consist of convective cores and stratiform or cirrus regions where clouds have detrained from the core. The lack of discrete boundaries between different types of clouds makes it difficult to separate convective grid points from surrounding stratiform regions. Overshooting tops and enhanced-V pattern are well-known features in mature convective clouds, but these do not appear until their strongest stage and not in all convective clouds. Using such features associated with the deepest convective cores will create a detection gap between early and mature stages of convection. The method described here tries to minimize the gap, while still accurately detecting convective clouds.

Before evaluating the texture, only the grid points that are potentially parts of deep convection are selected using simple threshold values of VIS (ABI channel 2; 0.65μm) and IR (ABI channel 14; 11.2μm) channels. Channel 2 reflectance is highly correlated with the cloud optical depth (Minnis and Heck, 2012) while Channel 14 brightness temperature is related to cloud top temperature (Müller et al., 2018). These channels are used in GOES-R baseline product retrieval of cloud optical depth and cloud top properties, respectively. Any grid points with reflectance less than 0.8 or T_b greater than 250K during ten time steps (10 minutes) are removed since they generally represent thin or low clouds such as cirrus or growing clouds that can be identified by the CI method described earlier. These thresholds are chosen rather generously to include some convective clouds that have not grown into deep convection yet,

while still avoiding the misclassification of low cumulus clouds and thin anvil clouds as convective. The threshold of 250K is much warmer than typical values used in detecting deep convective features such as overshooting tops (Bedka et al., 2010) or enhanced-V (Brunner et al., 2007). Warmer threshold is intentionally chosen so that the method considers warmer convective clouds without those features in the next step when evaluating lumpiness of the cloud top. The choice of these thresholds is discussed in more detail in section 2.4.3.

Once cold, highly reflective scenes are identified, regions with bubbling cloud top are found. Bubbling cloud top is a distinct feature that appears in convective clouds, even in their early stages. The lumpiness of cloud tops can be numerically represented by calculating horizontal gradients in the reflectance field with the Sobel-Feldman (Sobel) operator which is commonly used in edge detection. The horizontal gradient is calculated at each pixel. The Sobel operator convolves the target pixel and its surrounding eight grid points with two kernels given in Equation (2.1) to produce gradients in the horizontal and vertical direction.

$$G_x = \begin{bmatrix} +1 & 0 & -1 \\ +2 & 0 & -2 \\ +1 & 0 & -1 \end{bmatrix} \quad G_y = \begin{bmatrix} +1 & +2 & +1 \\ 0 & 0 & 0 \\ -1 & -2 & -1 \end{bmatrix} \qquad (2.1)$$

By using Equation (2.2), gradients in each direction are combined to provide the absolute magnitude of the gradient at each point.

$$\text{Magnitude of gradient} = \sqrt{G_x^2 + G_y^2} \qquad (2.2)$$

Flat surfaces will have low gradients while cloud edges or lumpy surfaces will have high gradients. This lumpy feature is most evident in a VIS channel with the finest spatial resolution of 0.5km. IR fields are not very useful as the brightness temperature variations in these lumpy surfaces tend to be quite small due to the IR's 2km resolution, and only cloud edges stand out.

The average of the horizontal gradients over the ten 1-minute time steps is calculated for each grid point, and grid points are removed if the average was less than 0.4 or greater than 0.9. Values below 0.4 or above 0.9 generally imply either stratiform region with a flat surface or cloud edges with very high gradients, respectively. The thresholds are chosen to produce relatively low false alarms comparing results using other thresholds. Results using other thresholds are also shown in section 2.4.3 for a comparison. The remaining grid points were then interpolated into 1km maps to be consistent with the spatial resolution of MRMS dataset. Neighboring grid points were grouped to form clusters, and only the clusters with more than 5 grid points were assigned as a mature convective cloud to remove noise. This method will be called as mature cloud detection method hereinafter.

2.4 Results and discussion

We begin the result section with two case studies that illustrate the technique as well as some of its limitations.

2.4.1 June 28th, 2017

Supercell thunderstorms developed in Iowa and produced several tornado touchdowns. In Figure 2.3a, deep convection had already developed over central Iowa at 19:30UTC, and two convective cells in the red box started to develop in southwest Iowa, although they do not stand out from surrounding low clouds in the VIS image. These two convective clouds became parts of major storm system that formed around 21:30UTC, producing the tornadoes (Figure 2.3b) in the area. MRMS Seamless Hybrid Scan Reflectivity (SHSR), which gives reflectivity at the lowest possible vertical level is shown in Figure 2.3c, and the MRMS PrecipFlag product is shown in Figure 2.3d. Convection is colored in pink and stratiform in green. Although deep convections

over central and northeast part of Iowa were assigned as convective in MRMS at 19:30UTC, the two growing clouds in the red box in Figure 2.3a were not assigned convective flag until 19:48UTC.

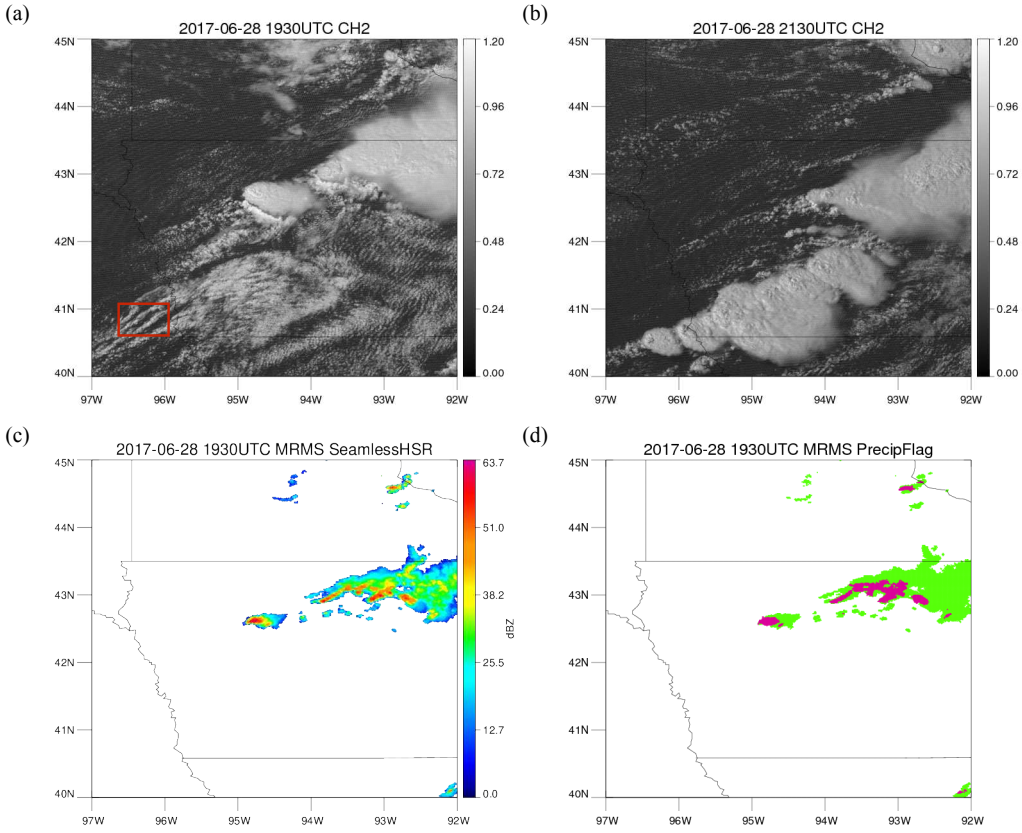

Figure 2.3 (a) GOES-ABI 0.65µm visible channel imagery (0.5km) at 1930UTC 28 June 2017 over Iowa. Numbers on the colorbar represent reflectances. The red box indicates regions where two convective cells are detected by the GOES T_b method. (b) GOES-ABI 0.65µm visible channel imagery at 2130UTC 28 June 2017. (c) MRMS Seamless Hybrid Scan Reflectivity (SHSR) at 1930UTC 28 June 2017. (d) MRMS PrecipFlag at 1930UTC 28 June 2017. Pink represents convective while green represents stratiform.

Figure 2.4a shows brightness temperatures for ABI channel 10 (7.3µm) at 19:27UTC. The two growing convective cells in the blue box are shown in barely visible yellow surrounded by high T_bs. The one on the left was detected using 10-minute data from 19:25UTC, but since both clouds were detected starting at 19:27UTC, a scene from 19:27UTC was used to

demonstrate the method. Figure 2.4c and 2.4d show T_b matrices that exhibited the correct shape for developing cells (Gaussian shape) at 19:27UTC and 19:36UTC. However, not all of the matrices in these figures showed the evolution of the developing cells (decreasing minimum T_b over 10K) between the two time steps. The two matrices in the blue box satisfied both criteria of maintaining the shape of developing cells and growing vertically over ten time steps while other matrices did not satisfy either one of the criteria. These two matrices contain early convective clouds that grow into deep convection shown in Figure 2.3b, and they are correctly captured by this method.

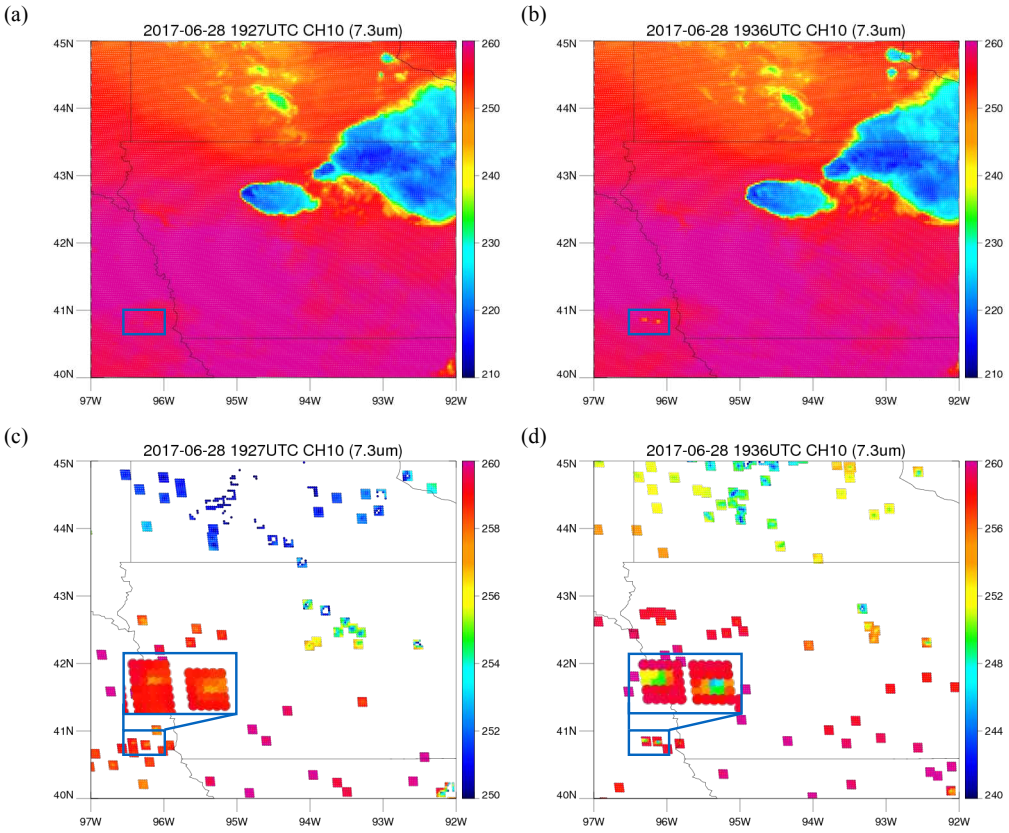

Figure 2.4 (a) GOES-ABI 7.3µm infrared channel imagery (K) at 1927UTC 28 June 2017. Blue box denotes regions where two convective clouds start to grow. (b) Same as Figure 2.4a, but at 1936UTC. (c) T_b matrices obtained from channel 10 (7.3µm) that have the Gaussian shape at 1927UTC 28 June 2017. Blue box denotes the same region as the blue box in Figure 2.4a. Note that the scale of the colorbar is adjusted from Figure 2.4a and 2.4b to better observe convective initiation. (d) Same as Figure 2.4c, but at 1936UTC.

Results for the detection of mature convective clouds are shown in a step by step fashion in Figure 2.5. Figure 2.5a is the same as in Figure 2.3a, but is mapped using a different color table for better comparisons between steps. Figure 2.5b shows the pixels retained after eliminating all the grid points that did not meet the reflectance and T_b thresholds (minimum reflectance over ten time steps greater than 0.8 and maximum T_b over ten time steps less than 250K). Figure 2.5c shows the horizontal gradient values after applying the Sobel operator. The colorbar is set to be within the range of 0.4 and 0.9 to display potential convective regions that passed these thresholds in colors. White regions are either regions that have average gradients greater than 0.9 such as cloud edges or thin cirrus clouds, or regions that have average gradients less than 0.4 such as clear sky or stratiform regions. Eventually, only the regions that meet both the criteria in Figure 2.5b and 2.5c are assigned to convection, and shown as white shade in Figure 2.5d. Using reflectance threshold sometimes limits the detection of shaded convective regions that exhibits lower reflectance than the threshold of 0.8. This is case for the small imbedded white regions in the midst of high reflectance regions shown in Figure 2.5b. However, these regions are relatively small, and once they are upsampled into 2km maps through nearest neighbour interpolation, some of these regions are included in the detection as shown in Figure 2.5d.

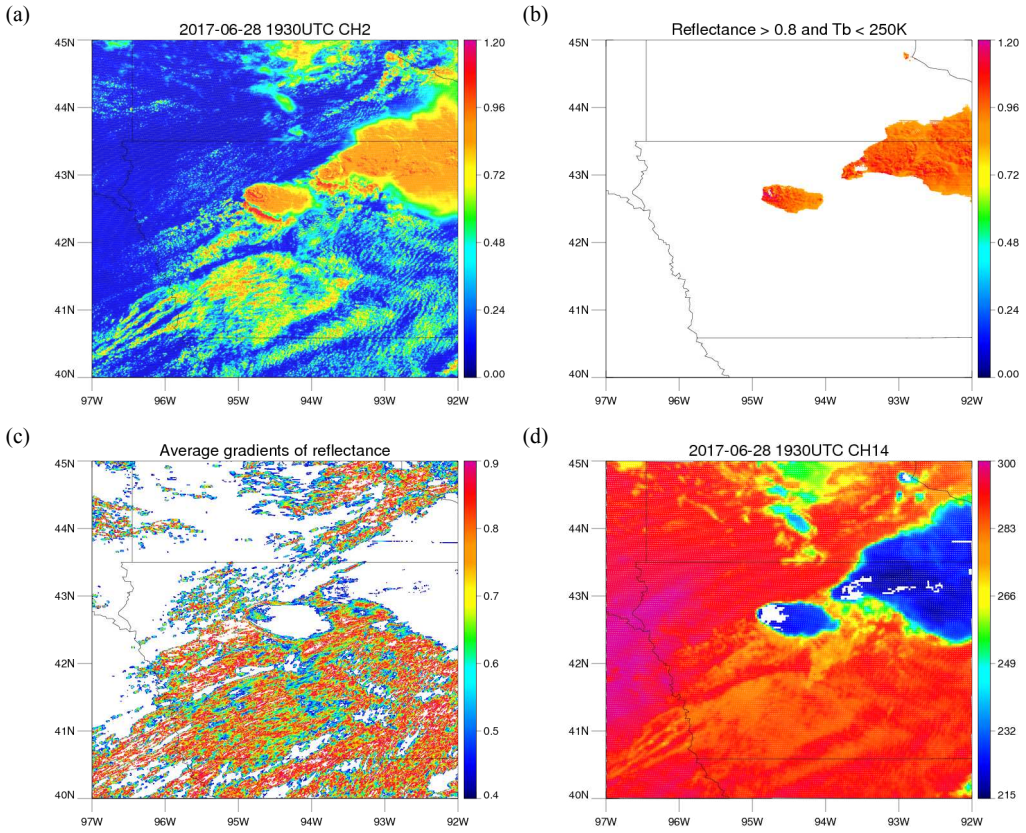

Figure 2.5 (a) Same as Figure 2.3a, but using different color table. (b) From the reflectance map in Figure 2.5a, regions that have reflectances less than 0.8 over 10 minutes or have T_bs greater than 250K over 10 minutes are assigned reflectance of zero, and therefore colored in white. (c) Map of average gradients of reflectances over 10 minutes. Regions with average gradient less than 0.4 or greater than 0.9 are colored in white. (d) GOES-ABI 11.2μm infrared channel imagery (K) at 1930UTC 28 June 2017. Regions that passed two criteria from Figure 2.5b and 2.5c are colored in white.

Detection from GOES and MRMS is compared in MRMS's resolution of 1km, and in such high resolution, the location of a cloud seen from GOES and MRMS can be slightly different due to parallax displacement. For a better comparison between detection from GOES and MRMS, parallax correction based on Vicente et al. 2002 is applied to GOES detection using a constant cloud top height of 10km. Convective regions detected by GOES (Figure 2.5d) are plotted with the parallax correction on top of the MRMS map (Figure 2.3d), and it is shown in

Figure 2.6. When compared to high reflectivity regions in Figure 2.3c and convective regions in Figure 2.3d, convective regions while not perfectly aligned due to a number of dynamic geometric reasons, do have a high degree of correspondence between the two detection methods. However, a straight line around 44N at the right edge of Figure 2.5d is definitely not a convective region, and it is due to unrealistically high reflectance in the raw satellite dataset. These kinds of artifacts were removed later in section 2.4.3 when the method was applied to a full month of data. However, multiple lines are difficult to remove at this stage in the processing and will result in false alarm. As quality control procedures on ABI are improved, this may no longer be a source of significant errors.

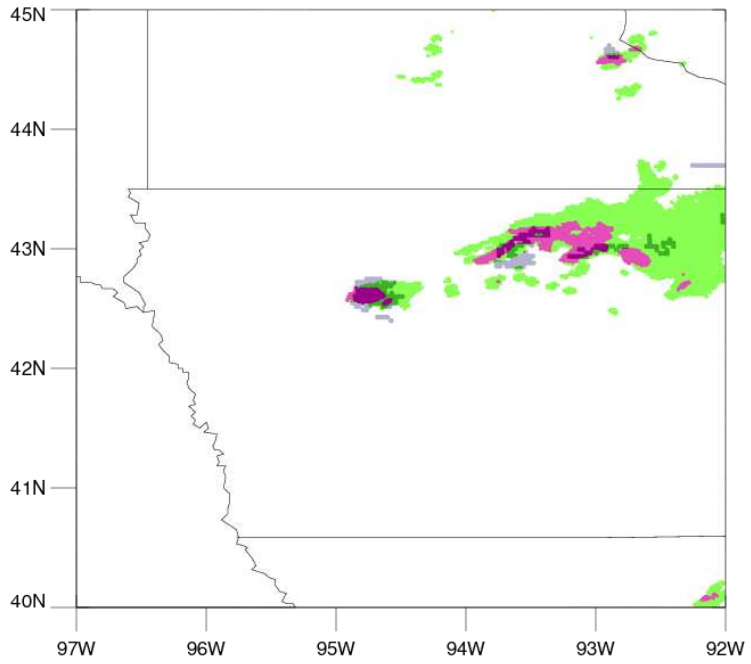

Figure 2.6 Convective regions detected by GOES-16 (white regions in Figure 2.5d) are colored in navy on top of MRMS PrecipFlag at 1930UTC 18 June 2018 (Same figure on Figure 2.3d. Pink represents convective while green represents stratiform)

2.4.2 June 18th, 2018

Another case was examined to evaluate the methods under different conditions. Severe storms developed over the Great Plains in June 18th, 2018, producing hail on the ground. At 22:30UTC, sporadic storms across Kansas and Oklahoma were observed by GOES-16. This scene contains both growing and mature convective clouds that are detected by MRMS during 22:30UTC ~ 22:40UTC period. Especially, four vertically growing clouds in this scene show different evolution and thus allow to elaborate more on the growing cloud detection method. MRMS PrecipFlag for the scene at 22:30UTC and 22:40UTC is shown in Figure 2.7a and 2.7b, respectively. Green color represents stratiform and pink color represents convective clouds. Figure 2.7c and 2.7d are T_b maps of the same scene at 22:30UTC and 22:40UTC, respectively. Growing clouds shown in purple, blue, yellow, and green boxes are detected by the growing cloud detection method, but all starting from different time. Times that each cloud is detected by GOES and MRMS are shown in Figure 2.7a. Time for the growing cloud detection method is a period as the method uses 10 consecutive 1-minute data. Convection in the purple box was detected six minutes earlier than MRMS detection considering the last data used in the growing cloud detection method at 22:28UTC. Similarly, a cloud in the green box was detected a little earlier by GOES than MRMS. The growing cloud in the yellow box was detected at the same time by GOES and MRMS. On the other hand, the growing cloud in the blue box was detected later than MRMS detection at 22:38UTC. This cloud did not grow rapidly enough during 22:30UTC ~ 22:40UTC period as shown in T_b maps of Figure 2.7c and 2.7d and did not meet the T_b threshold for channel 10 at the onset of convection. However, it was detected by channel 8 as it grew higher altitudes. This shows that a cloud that initially did not show high growth rate can have high growth rate as it vertically grows and can be detected by channel 8 later in time. These

results show that even though the thresholds for the growing cloud detection method can miss some convective clouds that grow slowly in the beginning, the thresholds were adequate for detecting rapidly growing convective storms which are of more interest during the forecast.

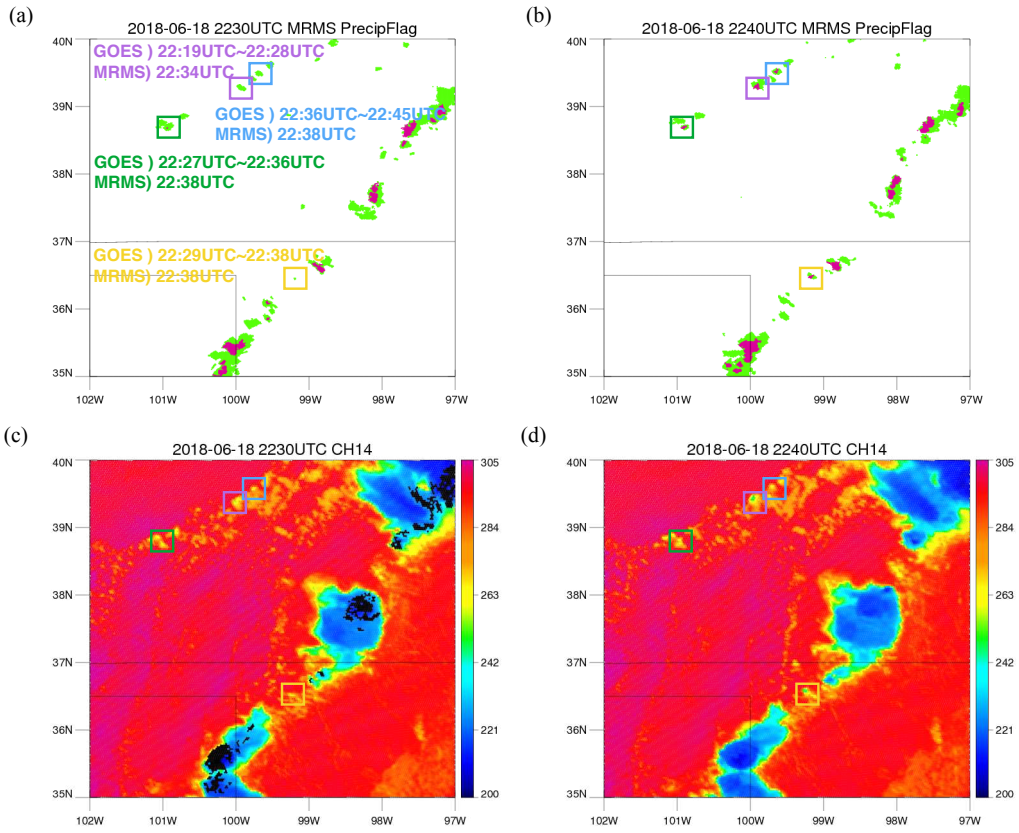

Figure 2.7 (a) MRMS PrecipFlag at 2230UTC 18 June 2018. Pink represents convective while green represents stratiform. Times next to each box represents the times of GOES data used in the mature cloud detection method and time of detection by MRMS. (b) MRMS PrecipFlag at 2240UTC 18 June 2018. (c) GOES-ABI 11.2µm infrared channel imagery (K) at 2230UTC 18 June 2018 over the Great Plains. (d) Same as Figure 2.7c, but at 2240UTC.

Black regions superimposed on the brightness temperature map in Figure 2.7c represent convective regions identified by the mature convection method, and Figure 2.8 shows overlay figure of the black regions on top of the MRMS PrecipFlag map (Figure 2.7a). There are slight misalignments of detected convective clouds between MRMS PrecipFlag products and GOES

results possibly due to sheared vertical structures of the storms. One other thing to note here is that convective area detected by the mature cloud detection method is greater than what is detected in the previous case. This could be due to dependency of lumpiness on solar zenith angle or latitude. Lumpiness increases as solar zenith angle increases, and since the spatial resolution of GOES data increases with latitude due to viewing angle, lumpiness appears less clear in high latitude regions. However, the method generally finds convective core region correctly.

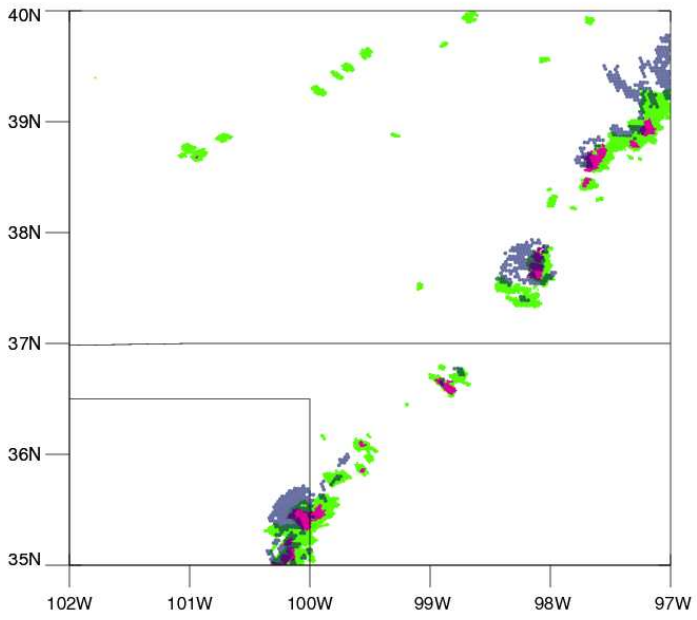

Figure 2.8 Convective regions detected by GOES-16 (in Figure 2.7c) are colored in navy on top of MRMS PrecipFlag at 2230UTC 18 June 2018 (Figure 2.7a). Pink represents convective while green represents stratiform)

2.4.3 Statistical results with one-month data

Pixel-based validation of the two methods is conducted using one month of data during June of 2017. Results are validated against MRMS data as ground-based radar is used to detect convective regions during the short-term forecast, and precipitation is a rather direct indicator of convection in all stages. Since MRMS detection comprises convection in all stages, MRMS data are compared with GOES detection combining the two methods. Table 2.3 is a contingency table applying both methods to one month data and comparing in MRMS's grids with a spatial resolution of 1km. C represents convection detected by either GOES or MRMS, and NC represents non-convective regions. GOES-C/MRMS-C is "hits" that both MRMS and GOES methods detected as convective within 5km. In case of the growing cloud detection method, on the other hand, hits are defined if MRMS assigned convective within 30 minutes due to earlier detection by this method. GOES-NC/MRMS-C is "misses" that GOES missed detecting convection while MRMS assigned as convective. GOES-C/MRMS-NC is "false alarm" that GOES detected as convective, but MRMS did not. Lastly, GOES-NC/MRMS-NC is "correct negative case" that both MRMS and GOES did not detected as convective. From the contingency table, verification metrics of probability of detection (POD) and false alarm rate (FAR) can be calculated as below.

$$POD = \frac{hits}{hits + misses} \qquad FAR = \frac{false\ alarm}{hits + false\ alarm}$$

POD and FAR are useful tools in evaluating detection skill of a binary problem. POD and FAR calculated from Table 2.3 are 45.3% and 14.4%. Since POD and FAR can vary depending on the thresholds used in each method, choosing different thresholds is examined further.

Table 2.3. Contingency table of results applying both of GOES detection methods and validating against MRMS data during June of 2017. Pixel-based validation is conducted to produce this table. C and NC represent convective and non-convective, respectively.

	MRMS-C	MRMS-NC
GOES-C	2.73%	0.46%
GOES-NC	3.30%	93.51%

Most of the detection is from the mature cloud detection method as mature convective clouds account for much larger area. The mature cloud detection method alone has FAR of 14.2% and POD of 43.7%. FAR and POD of the growing cloud detection method including 30-minute data are 22.2% and 3.9%, respectively. Relatively small FAR compared to Tables 2.1 and 2.2 would be because Tables 2.1 and 2.2 are obtained based on each cloud while FAR and POD are calculated based on each grid point. Two PODs do not add up to 45.3%, POD from Table 2.3 due to overlapped detection. Since the mature cloud detection method resort to several thresholds, results using different combinations of the three thresholds (reflectance at channel 2 and T_b at channel 14 to remove shallow and low clouds, and horizontal gradients of reflectance at channel 2 to remove cloud edges as well as clouds with flat cloud top surfaces) are presented to show how they differ from the chosen thresholds. Two thresholds for cloud top texture, which is essentially horizontal gradients of reflectance, are evaluated first. The upper threshold does not change results much (not shown), and cloud edges are effectively removed by the threshold of 0.9. The lower bound of the texture thresholds are varied, keeping the upper threshold and the T_b and reflectance thresholds constant. Resulting FAR and POD are shown in Figure 2.9. Using 0.5 (yellow) misses significant amounts of convective regions while using lower values (blue and red) substantially misclassifies stratiform regions with flat cloud tops as convective, although their PODs are much higher. Using 0.2 gives the closest results from the pixel-based validation

in Zinner et al. 2013 using lightning data. However, FAR of 45.6% when using 0.2 is almost a random chance that it is no longer useful, while POD of 29.9% when using 0.5 will not give much information. Therefore, values of 0.4 and 0.9 (green diamond in Figure 2.9) were chosen as a reasonable compromise between POD and FAR.

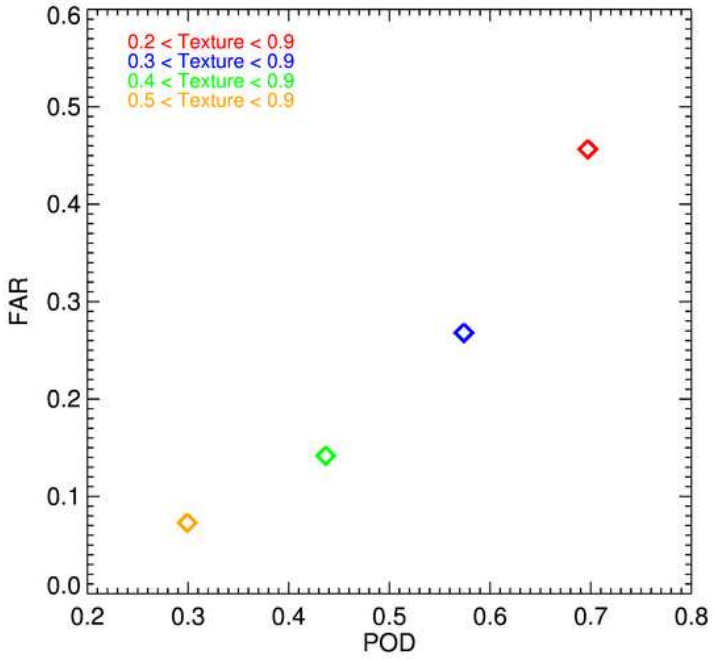

Figure 2.9 Plot of probability of detection (POD) and false alarm ratio (FAR) using different texture thresholds of the mature cloud detection method. The T_b and reflectance thresholds are kept constant with 250K and 0.8, respectively.

POD and FAR using different combinations of T_b and reflectance thresholds are plotted in Figure 2.10, and this time texture thresholds are kept constant with 0.4 and 0.9. The T_b threshold is varied from 230K to 250K, and the reflectance threshold is varied from 0.7 to 0.9. There is a trade-off between detecting more convective clouds that are transitioning into mature stage and incorrectly assigning cumulus clouds as convective clouds. Having lower value for the T_b threshold or higher value for the reflectance threshold leads to small FAR, but also leads to small POD. To make this method effective and reduce FAR as much as possible for its potential use in the short-term forecast, 250K for the T_b and 0.8 for the reflectance threshold (black

diamond in Figure 2.10) are chosen. It is better to not give any information and let the model to resolve convection by itself than to lead the model into the wrong direction with a false information and initiate convection in the wrong place. 240K and 0.7 (orange) also showed similar results, but 250K and 0.8 were chosen due to lower FAR.

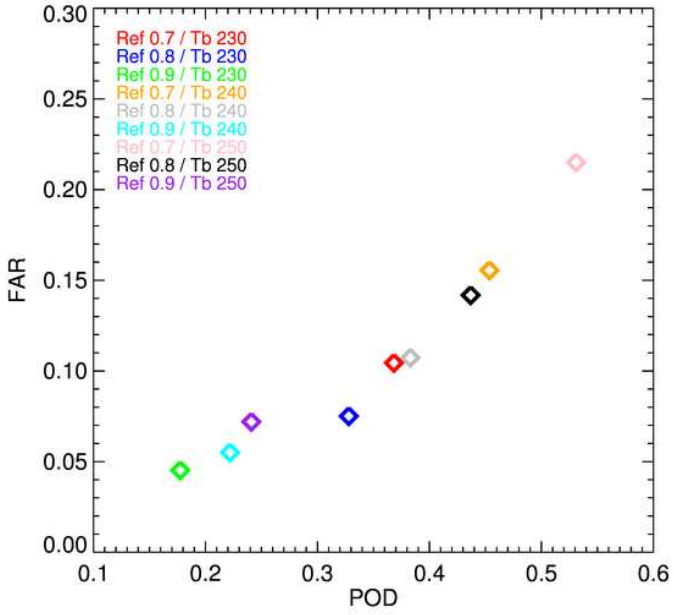

Figure 2.10 Plot of probability of detection (POD) and false alarm ratio (FAR) for different combinations of T_b and reflectance thresholds. The texture threshold of 0.4 and 0.9 are kept constant.

Despite its FAR being relatively small, the method misses significant amounts of convective areas observed by MRMS. Therefore, regions that were missed are evaluated further to investigate which threshold contributed most to missing those regions. Figure 11 shows histograms of T_b, reflectance, and texture in the convective regions that were missed by the above method. It is clear from the figure that the largest number of misses were due to low texture values (87.6% of all missed regions has lower gradients than 0.4). There are many reasons why convective regions appear to have flat cloud top surfaces. Anvil or thick cirrus

clouds above convective regions can smooth out or cover bubbling cloud tops, and there is simply no way to avoid this problem. Another reason may be the nature of the classification method. Since classification by MRMS is determined by rain rate, even if convective clouds are in a decaying mode and do not bubble anymore, clouds can still continue to precipitate considerable amounts, which would lead to convective category in the MRMS product. It is also possible that it is due to a misclassification of trailing stratiform regions using radars. It is indeed an ongoing research in the radar community since better convective/stratiform classification scheme improves QPE retrieval (Qi et al., 2013; Veljko et al., 2019).

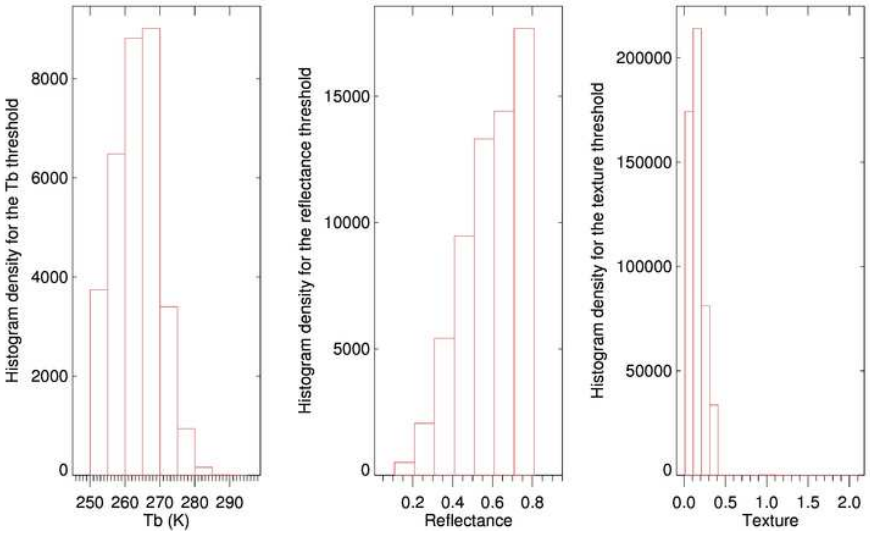

Figure 2.11 Histograms of T_b, reflectance, and texture values if a pixel was assigned to be convective by MRMS, but not detected by the mature cloud detection method due to each of the thresholds.

As shown from these results, there are no perfect thresholds that can separate convective and stratiform clouds. Nevertheless, threshold values were chosen in line with our main objective - to avoid high FAR as much as possible and have decent POD comparable to radar products. Avoiding FAR is a higher priority than reaching higher POD as giving false information is most detrimental during data assimilation. Low FAR of 14.4% is achieved, and among those misclasified pixels, 96.4% of them are at least raining. Since the main objective of data assimilation is to have good initialization of precipitation, applying these methods during data assimilation can still be beneficial in case the forecast model did not produce precipitation. Unfortunately, significant amounts of convective areas assigned by the radar product are missed. As shown in Fig. 11, most of the missed regions are excluded due to flat surface, and this is an intrinsic problem of using VIS and IR bands. If a convective cloud is developing in a less cloudy scene, it can be detected by the method most of the time. However, in case of a hurricane where cloud tops are rather flat, or multi-layer clouds where cloud top information is decoupled from what is underneath, convection will be missed by the detection method. Furthermore, flat cloud top regions close to bubbling area might still be convective by MRMS due to high reflectivity, leading those regions to be classified as missed. The thresholds can be adjusted for other applications that may require higher POD.

2.5 Conclusion and Summary

This study explores two methods to detect convective clouds using GOES-R ABI data with one minute interval. Using such high temporal resolution data facilitates cloud tracking and helps the accuracy of the detection method when calculating decreases in T_b of the same cloud. Convective clouds in the early stage were detected using T_bs of ABI channels 8 and 10. These

channels were used to find cloud scenes with the developing shape of convective clouds. They were then used again to calculate the T_b decrease for those which maintained the developing shape for ten minutes. A cloud scene that had a consistent developing shape and a large decrease in T_b over ten minutes was classified as convective by this method. Mature convective clouds were detected by masking out regions with high T_b in ABI channel 14 and low reflectance in ABI channel 2 and finding regions with high horizontal gradients of reflectance over the course of ten minutes. Results from this reflectance method were mostly consistent with the radar-derived products, although this method is limited to daytime use only. Nevertheless, it detects a wide range of convective area, not just regions with overshooting tops.

These methods work well for well-structured convective clouds, but there are limitations to this method as with most algorithms using IR and VIS sensors have. Cirrus cloud shields are the biggest problem as they block T_b decreases underneath and smooth out lumpy reflectance surfaces. However, these methods can still be extremely useful for defining convection for assimilation into models where radar data is not available. Because regions identified as convective are most likely convective (~85% accuracy), this can easily be assimilated while setting cloudy regions to "missing" since the accuracy of detecting convection under large cirrus shields is poor. Furthermore, results using Sobel operator, which is commonly used in image processing, implies that applying machine learning can be beneficial if the model can be set up to learn lumpy texture of convective clouds during training.

CHAPTER 3: APPLYING MACHINES LEARNING METHODS TO DETECT CONVECTION USING GOES-16 ABI DATA

3.1 Introduction

Artificial intelligence (AI) is flourishing more than ever as we live in the era of big data and increased processing power. Atmospheric science, with vast amounts of satellite and model data, is not an exception. In fact, numerical weather prediction and remote sensing are ideally suited to machine learning as weather forecasts can be generated on demand, and satellite data are available around the globe (Boukabara et al., 2019). Applying machine learning to forecast models can be beneficial in many ways. It can improve computational efficiency of model physics parameterizations (Krasnopolsky et al., 2005) as well as developing new parameterizations (O'Gorman et al., 2018; Brenowitz and Bretherton, 2018; Beucler et al., 2019; Gentine et al., 2018; Rasp et al., 2018; Krasnopolsky et al., 2013). On the other hand, applying machine learning techniques to satellite data can help overcome limitations with both pattern recognition as well as multi-channel information extraction.

Detecting convective regions from satellite data is of great interest as convection resolving models begin to be applied on global scales. Historically, these models were only regional, and surface radars within dense radar networks were used. Radars are useful because of the direct relationship between radar reflectivity and precipitation rates and their ability to provide vertical information about convective systems. However, ground-based radars are not available over oceanic or mountainous regions, and radars on polar-orbiting satellites have been limited to very narrow swaths. Therefore, many studies have suggested methods for using geostationary visible and infrared imagery that has good temporal and spatial coverage.

Visible and infrared data from geostationary satellites are available nearly anywhere and in near-real time. They have provided an enormous amount of weather data, but due to the lack of vertical information, their use in forecasting has been limited largely to providing cloud top temperature or atmospheric motion vectors in regions without convection (Benjamin et al., 2016). Some studies have tried to identify convective regions using these sensors by finding overshooting tops (Bedka et al., 2010; Bedka et al., 2012; Bedka and Khlopenkov, 2016) or enhanced-V features (Brunner et al., 2007). However, since not all the convective clouds have such features, and never until they reach a very mature stage, some studies have tried to detect broader convective regions by using lumpy cloud top surfaces (Bedka and Khlopenkov, 2016). Studies have also looked at convective initiation by observing rapidly decreasing cloud top heights (Mecikalski et al., 2010; Sieglaff et al., 2011) but were limited by tracking problems when only 15-, 30-, or even just 60-minute data were available.

Current operational geostationary satellites, the Geostationary Operational Environmental Satellite-R (GOES-R) series, foster the use of visible and infrared sensors in detecting convection as their spatial and temporal resolutions are much improved from their predecessors. Currently operational GOES-16 and GOES-17 carry the advanced baseline imager (ABI), whose 16 channels comprise wavelengths from visible to infrared. Data is collected every 10 minutes over the full disk area, 5 minutes over Contiguous United States (CONUS), and every minute in mesoscale sectors defined by the National Weather Service as containing significant weather events. When humans look at image loops of reflectance data with such high temporal resolution, most can point at convective regions because they know from past experiences that bubbling clouds resemble bubbling pots of water that imply convective heating. A recent study by Lee et al. 2020a uses several features of convective clouds such as high reflectance, low brightness

temperature, and lumpy cloud top surface to detect convection from GOES-16 data in mesoscale sector. In their method, respective thresholds for reflectance, brightness temperature, and lumpiness are determined empirically. Here we seek to automate the process of detecting convection using AI, which, provided with the same type of information that humans use in this decision process, might be able to learn similar strategies as humans. Thus this study applies machine learning techniques to detect convection using high temporal resolution visible and infrared data in ABI.

Machine learning, and in particular neural networks, are emerging in many remote sensing applications for clouds (Mahajan and Fataniya, 2020). Application of neural networks has led to more use of geostationary satellite data in cloud-related products such as cloud type classification or rainfall rate estimation which has been challenging in the past (Bankert et al., 2009; Gorooh et al., 2020; Hayatbini et al., 2019; Hirose et al., 2019). Especially using GOES-16, raining cloud is detected by Liu et al. 2019 with a deep neural network model, and radar reflectivity is estimated by Hilburn et al. 2020 using a model with convolutional layers. Spectral information from several channels in geostationary satellites has been useful to deduce cloud physics along with the spatial context that can be extracted using convolutional layers.

Machine learning techniques have recently been viewed as solving every existing problem without the need for physical insight, but in practice, physical knowledge of the system is usually essential to solve problems effectively. These properties that are associated with mature convection have temporal aspects; continuously high reflectance, high or growing cloud top height and bubbling cloud top surface over time. Therefore, these time-evolving properties are considered when selecting and processing the input and output dataset as well as in constructing the model setup.

This study explores a machine learning model with a convolutional neural network (CNN) architecture to detect convection from GOES-16 ABI data. The model is trained using Multi-Radar Multi-Sensor (MRMS), one of the radar-based products, as outputs. After training, the model results on validation and testing dataset are compared to examine its detection skill, and two scenes from the testing data are presented to further explore which feature of convection the model uses to detect convective regions.

Features that distinguish this work from existing work are: (1) Studies using machine learning with geostationary satellite data are typically designed for the goal of rainfall rate estimations or classification of various cloud types, while our goal is detecting convection so that appropriate heating can be added to initiate convection in the forecast model; (2) We feed temporal sequences of GOES-16 imagery into the neural network model to provide the algorithm with the same information a human would find useful to detect the bubbling texture in GOES-16 imagery indicative of convection; (3) We use a two-step loss function approach which makes the model's performance less sensitive to threshold choice.

3.2 Data

GOES-16 ABI data are used as inputs to the CNN model, while the outputs are obtained from the Multi-Radar Multi-Sensor (MRMS) dataset. Three independent datasets are prepared for training, validation, and testing. Data are collected over the central and eastern part of CONUS where GOES-16 focuses on. Tables 3.1 and 3.2 list time and location of 20 significant weather events to span a broad set of deep convective storms that are used to create the dataset. Input data are obtained every 20 minutes so that the dataset contains overall evolution of convection from convective initiation to mature stage of convection. As shown in the table,

training data are selected mostly over the southern and eastern part of CONUS to effectively train the model with higher quality of radar data over those regions. A total of 19,987 training data are collected from 10 convective cases in Table 3.1, but only 10,019 images that contain raining scenes, which means that any precipitation type is assigned by MRMS in at least one grid point, are used during the training, and the remaining scenes are discarded. This is done to force the model to focus more on distinguishing between convective core and surrounding stratiform clouds, rather than training with redundant non-precipitation scenes. For validation and testing, a total of 9,192 and 7,914 data samples are collected, respectively, each from five convective cases in Table 3.2. Similarly to training data, around half of both validation and testing dataset are clear regions, but no scenes are discarded in that case, whether they contain rain or not.

Table 3.1. A description of ten convective cases used for training data.

Date	Time	Mainly affected area
2019-05-28	2000 ~ 2350UTC	OK, KS, IA
2019-07-05	2000 ~ 2350UTC	CO, WY, NM, KS
2019-07-10	1600 ~ 2350UTC	OK, AR, MO, TX
2020-05-12	1600 ~ 2350UTC	TX
2020-05-15	1400 ~ 2350UTC	OK, TX
2020-05-24	1900 ~ 2350UTC	TX
2020-06-19 (M1)	1900 ~ 2350UTC	PA, MD, VA, NC
2020-06-19 (M2)	1900 ~ 2350UTC	TX, OK, CO
2020-06-21	1900 ~ 2350UTC	KS
2020-07-12	1900 ~ 2050UTC	AL, MS

Table 3.2. A description of ten convective cases used for validation (upper five) and testing (lower five) data.

Date	Time	Mainly affected area
2019-05-23	2100 ~ 2350UTC	TX, OK, KS
2019-05-24	1900 ~ 2350UTC	TX, OK, KS
2019-08-20	1800 ~ 2150UTC	MO, IL, IN
2020-07-22	1800 ~ 2350UTC	VA, MD, PA, DE, JN
2020-07-31	1800 ~ 2350UTC	TX, LA, MS, AL
2019-06-22	1900 ~ 2350UTC	MS, AL, GA
2019-06-23	2000 ~ 2350UTC	TX, OK, AR, LA
2019-08-13	1900 ~ 2150UTC	TN, NC, SC, VA
2020-07-02	2000 ~ 2350UTC	CO, KS, NE, SD

2020-08-06	1900 ~ 2350UTC	NC, VA, DE

3.2.1 The Geostationary Operational Environmental Satellite R series (GOES-R)

GOES-R series, consisting of GOES-16 and GOES-17, carry the ABI with 16 channels. Channel 2 is referred to as the "red" band, and its central wavelength is at 0.65μm. It has the finest spatial resolution of 0.5km, and therefore provides the most detailed image for a scene. Any data with sun zenith angle higher than 65° is removed, and reflectance data at this channel are divided by the cosine of the sun zenith angle to normalize the reflectance data. Since normalized reflectance values rarely exceed 2, any data with a reflectance value greater than 2 is truncated at 2. All data is subsequently scaled to a range from 0 to 1. Although we can observe bubbling from reflectance images at channel 2 (0.65μm), additional brightness temperature data can effectively remove some low cumulus clouds that appear bright. These clouds are not distinguishable from high clouds in the visible image, but they appear distinct in an infrared T_b map. Therefore, brightness temperature data at channel 14 are also inserted as input for the AI model. Note that the spatial resolution of channel 14 is 2km, i.e. four times coarser than that of channel 2. Channel 14 is a "longwave window" band, and its central wavelength is located at 11.2μm. This channel is usually used to retrieve cloud top temperature, and therefore is used to eliminate low cumulus clouds. Channel 14 data are also scaled linearly from 0 to 1, corresponding to a minimum value of 180K and a maximum value of 320K.

Input data of channels 2 and 14 are created by separating the whole image into multiple 64km×64km images corresponding to 128×128 and 32×32 pixels at channels 2 and 14, respectively. We will refer to these small images as *tiles*. Each input sample then consists of five consecutive tiles at channel 2, at two-minute interval, and five consecutive tiles at channel 14, also at two-minute interval, but lower resolution.

3.2.2 Multi-Radar/Multi-Sensor (MRMS)

MRMS data, developed at NOAA's National Severe Storms Laboratory, are produced combining radar data with atmospheric environmental data, satellite, lightning, and rain gauge data (Zhang et al., 2016). "PrecipFlag", one of the available variables in MRMS, classifies surface precipitation into seven categories; 1) warm stratiform rain, 2) cool stratiform rain, 3) convective rain, 4) tropical-stratiform rain mix, 5) tropical-convective rain mix, 6) hail, and 7) snow. A detailed description of the classification can be found in Zhang et al. (2016). The classification goes beyond using a simple reflectivity threshold as it considers vertically integrated liquid, composite reflectivity, and reflectivity at 0°C or -10°C according to radar's horizontal range. In addition, the quality of the product is further improved by effectively removing trailing straitiform regions with high reflectivity or regions with bright band or melting graupel (Qi et al., 2013).

This radar-based product is used as output or truth with slight modifications. Since our model is set up to produce a binary classification of either convection or non-convection, the seven MRMS categories are reconstructed into two classes. Precipitation types of convective rain, tropical-convective rain mix, and hail are assigned as convection, and everything else are assigned as non-convection excluding grid points with snow class. A value of either 0 (non-convective) or 1 (convective) is assigned to each grid point of the 128x128 tile (64×64km), after applying a parallax correction with an assumed constant cloud top height of 10km. Grid points are assigned to 1 if the grid point is assigned as convective at least once during the five time steps. In order to remove low quality data, only the data with "Radar quality index (RQI)" greater than 0.5 are used in the study.

As mentioned in the beginning of this section, non-precipitating scenes that are not classified to any of the precipitation type are removed during training. Otherwise, the number of non-convective scenes greatly exceeds the number of convective scenes, and misclassification penalties calculated from misclassified convective cases have less impact in updating the model.

3.3 Machine learning model

The problem we are trying to solve can be interpreted as an image-to-image translation problem, namely converting the GOES-R images to a map indicating convective regions. *Neural networks* have been shown to be a powerful tool for this type of task. A neural network can be thought of as a function approximator, that learns, from a large number of input-output data pairs, to emulate the mapping from input to output. Just like a linear regression model seeks to learn a linear approximation from input to output variables, neural networks seek to achieve approximations that are non-linear and might capture highly complex input-output relationships.

Convolutional neural networks (CNNs) are a special type of neural network developed for working with images, designed to extract and utilize spatial patterns in images. CNNs have different layer types that implement different types of image operations, four of which are used here, namely convolution (C), pooling (P), upsampling (U), and batch normalization (BN) layers. Convolution layers implement the type of mask and convolution operation as used in classic image processing. However, in classic image processing the masks are predefined to achieve a specific purpose, such as smoothing or edge detection, while the masks in convolutional layers have adjustable mask values that are trained to match whatever functionality is needed. Pooling layers are used to reduce the resolution of an image. For example, a so-called “maxpooling” layer of size 2×2 takes non-overlapping 2×2 patches of an image and maps each to a single pixel

containing the maximum value of the 2×2 patch. Upsampling layers seek to invert pooling operations. For example, an upsampling layer of size 2×2 expands the resolution of an image by replacing each original pixel by a 2×2 patch through interpolation. Obviously, as information is lost in the pooling operation, an upsampling layer alone cannot invert a pooling layer, it just restores the image *dimension*, but additional convolution layers are needed to help fill in the remaining information. Batch normalization layers apply simple transformations to intermediate results in the CNN to avoid extremely large or small values, which tend to speed up neural network training.

The type of CNN used here is an encoder-decoder model. Encoder-decoder models take as input one or more images, feed them through sequential layers (C,P and U) that transform the image into a series of intermediate images, that finally lead to one or more images at the output. Encoder-decoder models use an encoder section with several convolution and pooling layers that reduces image dimension in order to extract spatial patterns of increasing size from the input images. The encoder is followed by a decoder section with several convolution and upsampling layers that expands the low resolution intermediate images back into the original input image size, while also expanding it in a different representation, such as converting the GOES-16 images to a map indicating convective regions.

Here an encoder-decoder model is built to produce a map of convective regions from two sets of five consecutive GOES-R images with two-minute interval: one set from channel 2 (0.65μm) and the other from channel 14 (11.2μm). The encoder-decoder model is implemented using the framework of Tensorflow and Keras. Figure 3.1 shows the architecture of the encoder-decoder model, and a model summary is shown in Table A1. Note that each convolution layer in Figure 3.1 is followed by a batch normalization layer. Those batch normalization layers are not

shown in Figure 3.1 to keep the schematic simple, but are listed in Table A1. In the input layer, only the reflectance data are read in. After two sets of two convolution layers (the first set with 16 filters and the second set with 32 filters), each set followed by a maxpooling layer, the spatial resolution of the feature maps is reduced to the same resolution as the T_b data. The T_b data are added at that point to the 32 feature maps from the previous layer, producing 37 feature maps. After another two sets of two convolution layers (each set respectively with 64 and 128 filters), each set followed again by one maxpooling layer, we reach the bottleneck layer of the model, i.e. the layer with the most compressed representation of the input. The bottleneck layer is the end of the encoder section of the model, and the beginning of the decoder section. The decoder section consists of four sets of two convolution layer (with a decreasing number of 128, 64, 32, and 16 filters). The first three sets of convolution layers are each followed by an upsampling layer, but the last set is followed by a transposed convolution layer with one filter to match with the 2D output. The single transposed convolution layer used here contains both upsampling and a convolution layer. Every layer uses the Rectified Linear Unit (ReLu) activation function except for the last transposed convolution layer, which uses a sigmoid function instead. A sigmoid function is chosen for the last layer so that the model produces a 128×128 map with continuous values between 0 and 1. These continuous values imply how close each pixel is to being non-convective (0) or convective (1). The values rarely reach 1, and therefore, a threshold has to be set to determine whether a grid point is convective or not. Higher threshold can increase the accuracy of the model, but more convective regions can be missed. Using different thresholds will be discussed in the next section.

A neural network is trained, i.e. its parameters are optimized, such that it minimizes a cost function that measures how well the model fits the data. It is very important to choose this

cost function, generally called *loss function* for neural networks, to accurately represent the performance we want to achieve. We investigate using a standard or two-step training approach, as described below. The standard approach minimizes a single loss function throughout the entire training. In this case, we use the mean squared error (MSE) as the loss function which penalizes misses and false alarms equally:

$$Loss = MSE = \sum(y_{true} - y_{predictedd})^2 \qquad (3.1)$$

where y_{true} is true output image and $y_{predicted}$ is the predicted output image, and the sum extends over all pixels of the true/predicted image.

The two-step training approach also starts out using the MSE as loss function (Equation (3.1)). However, once the MSE on the validation data converges to a low steady value, the neural network training continues with the loss function in Equation (3.2) which adds an extra penalty when the model misses convective regions (but not when it overestimates), in an effort to reduce missed regions:

$$Loss = MSE + \sum Maximum\left(\left(y_{true} - y_{predicted}\right), 0\right) \qquad (3.2)$$

where the sum again extends over all pixels of the true/predicted image. The additional term in Equation (3.2) is a positive for all pixels where the prediction is too small and 0 otherwise, thus it is expected to guide the model to detect more convective regions. The idea of using two different loss functions for coarse training and subsequent finetuning, or, more generally, to adjust loss functions throughout different stages of training, is discussed in more detail for example by Bu et al. 2020.

Results using one model trained with the standard approach and one trained with the two-step approach are compared in the next section. Detailed evaluation of the results is only presented for the two-step approach, as that represents our preferred model.

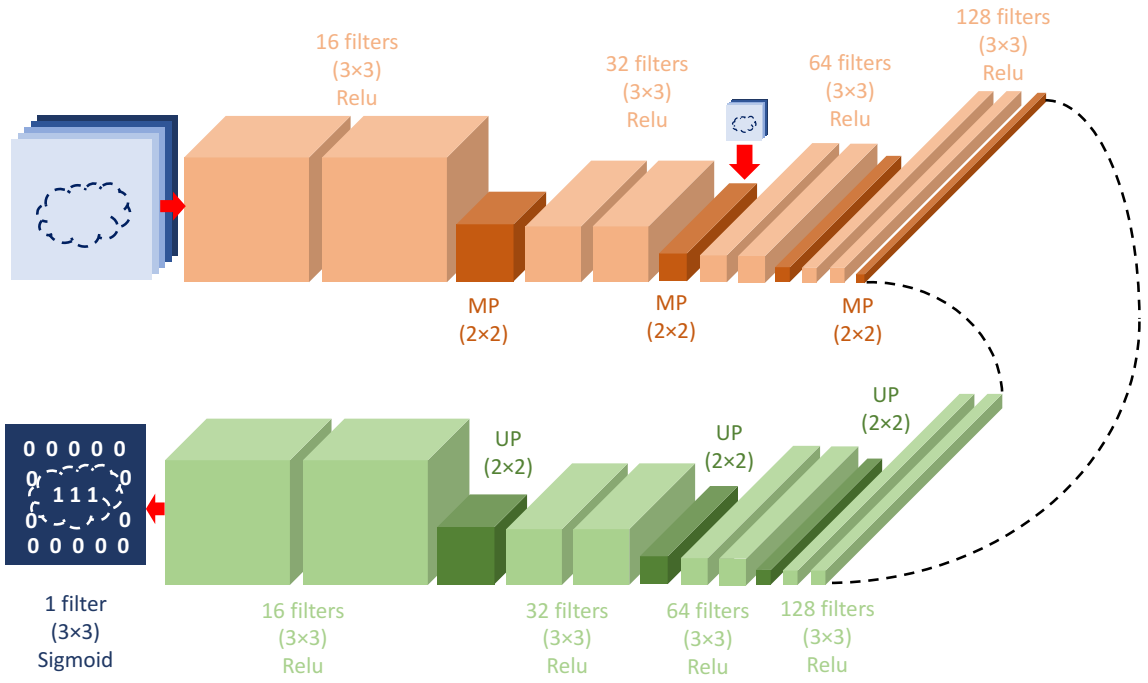

Figure 3.1 Description of the encoder-decoder model. (3×3) represents the dimension of a filter used in convolutional layers. MP refers to the maxpooling layer and UP refers to the upsampling layer, both with a window size of (2×2). Starting from five channel 2 images (upper left), the encoder section is presented in the upper row with the additional five channel 14 images entering after the second maxpooling layer. The decoder section is shown in the lower row from right to left with the output layer at the end (lower left).

3.4 Results

3.4.1 Overall performance using standard approach and two-step approach

In order to evaluate detection skill of the model, false alarm ratio (FAR), probability of detection (POD), success ratio (SR), and critical success index (CSI) are calculated for the training, validation, and testing dataset. FAR, POD, SR, and CSI can be calculated from the equations below.

$$FAR = \frac{false\ alarms}{hits + false\ alarms} \qquad (3.3)$$

$$POD = \frac{hits}{hits + misses} \qquad (3.4)$$

$$SR = 1 - FAR = \frac{hits}{hits + false\ alarms} \qquad (3.5)$$

$$CSI = \frac{hits}{hits+false\ alarms+misses} \qquad (3.6)$$

"Hits" are grid points that are classified as convective both by the model and MRMS. Considering slight mismatch due to different views by GOES and MRMS, hits are defined for a grid point deemed convective by the CNN model if MRMS assigns convective within 2.5km (5 grid points apart) even if MRMS classifies as non-convective at the actual grid point. "Misses" are grid points that are assigned as convective by MRMS but not by the model within 2.5km. "False alarms" are grid points that are predicted as convective by the model but not by MRMS within 2.5km. Figure 3.2 shows a performance diagram (Roebber, 2009) for a model using the two-step training approach demonstrating the effect of different thresholds for the training and validation dataset. As shown in the figure, there is a trade-off between fewer false alarms and more correctly detected regions. A higher threshold prevents the model from resulting in high FAR, but at the same time, POD becomes lower, and vice versa. Compared to SR and POD of 0.86 and 0.45 from Lee et al. 2020a that uses GOES-16 data as well, POD is much improved.

To compare results using the additional term in the loss function, a performance diagram for the testing dataset is shown in Figure 3.3a for the same two-step model as in Figure 3.2, together with a performance diagram using a model trained using the standard approach (only using MSE) in Figure 3.3b. Figure 3.3a and 3.3b show similar curves and thus similar detection skills, but the model trained with the standard approach needs a lower threshold to achieve similar detection skill. In Figure 3.3b, SR starts to degrade as the threshold becomes higher than 0.75, indicating that grid points with higher values, which are supposed to have the highest possibility to be convective, might be falsely detected ones in the model. This effect is also observed in the two-step model for extremely large thresholds (higher than 0.95), but those are

not shown in Figure 3.3a. The two-step model has slightly higher maximal CSI value of 0.62 than the model trained with standard approach which has CSI of 0.61. Even though adding the second term in Equation (3.2) does not seem to improve overall detection skill significantly, the resulting two-step model has less variation in FAR and POD between the thresholds, and more thresholds in the two-step model show CSI exceeding 0.6. We thus prefer the two-step model, as it delivers good performance without being overly sensitive to the specific threshold choice, so likely to perform more robustly across different data sets. Only results using the two-step model are further discussed.

The overall FAR and POD using the two-step approach are similar for the validation (Figure 3.2b) and testing dataset (Figure 3.3a), which implies the model is consistent, but they tend to fluctuate between different convective cases. Further examination on what the model has learned to identify convection is conducted by taking a closer look at two different scenes from the testing dataset in the following subsection. For each scene, results using different thresholds are presented, and several tiles in the scene are shown for discussion.

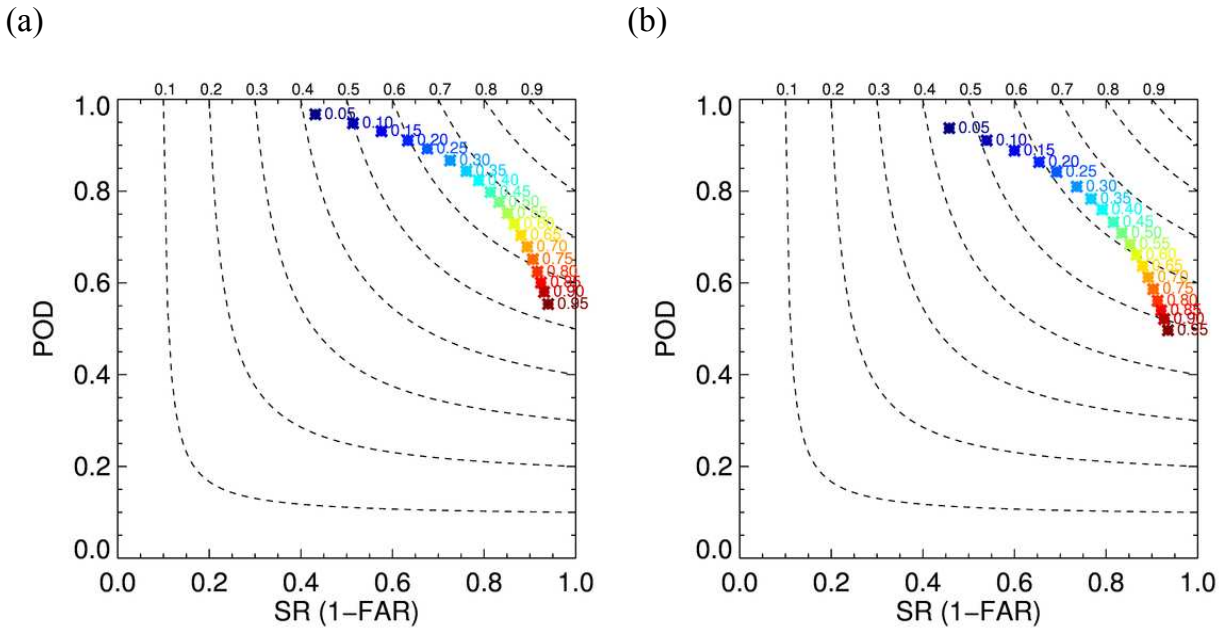

Figure 3.2 Performance diagrams using the two-step training approach for (a) training and (b) testing dataset. Numbers next to the symbol are thresholds used to get corresponding SR and POD. Dashed lines represent CSI contours with labels at the top.

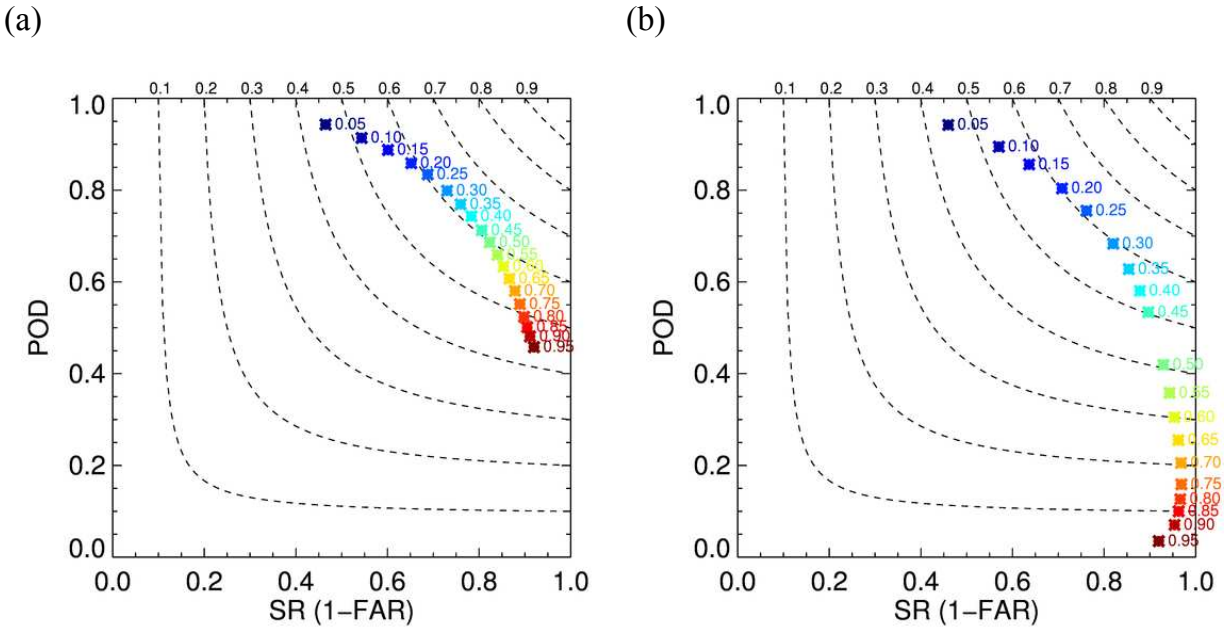

Figure 3.3 Performance diagrams using a model trained with (a) two-step training approach and (b) standard approach for testing dataset. Numbers next to the symbol are thresholds used to get corresponding SR and POD. Dashed lines represent CSI contours with labels at the top. The maximum CSI value is (a) 0.62 and (b) 0.61. CSI above 0.6 is achieved in (a) for thresholds from 0.25 to 0.45 and in (b) only for thresholds from 0.2 to 0.25. POD, FAR, SR, and CSI for all thresholds shown here are provided in Tables A2 and A3.

3.4.2 Exploring results for different scenes

Figure 3.4a shows GOES-16 visible imagery at channel 2 on 20th August, 2019 when a eastward moving low pressure system produced torrential rain. Some regions look discontinuous in the figure as 128×128 tiles with lower radar quality were eliminated from the dataset. Comparing with convective regions (pink) assigned by MRMS PrecipFlag in Figure 3.4b, convective clouds in the south of Missouri and Illinois or over Indiana show clear bubbling features while some over the Great Lakes do not. This is reflected in the results using different thresholds as the lower threshold tends to allow less bubbling regions to be convective. FAR and POD when using 0.5 are 11.0% and 51.4%, while they are 15.0% and 67.7% with 0.3. Additional detection made by 0.3 that contributed to increase in POD mostly occurred in less bubbling regions. Convective regions predicted by the model using two different thresholds of 0.5 and 0.3 are shown in Figure 3.5a and 3.5b, respectively. Colored regions in Figure 3.5 are convective regions predicted by the model, and the colors represent a scale of how much it is close to being convective (values close to 1 are more convective and values close to 0 are more stratiform). It is evident from the figures that using 0.3 as the threshold detects more convective regions than using 0.5. The colored boxes in Figure 3.5b indicate six scenes selected for further study, namely two scenes that are correctly identified as convection (green boxes), two scenes detected using the threshold of 0.3, but not of 0.5 (yellow boxes), and two scenes missed at both thresholds (red boxes).

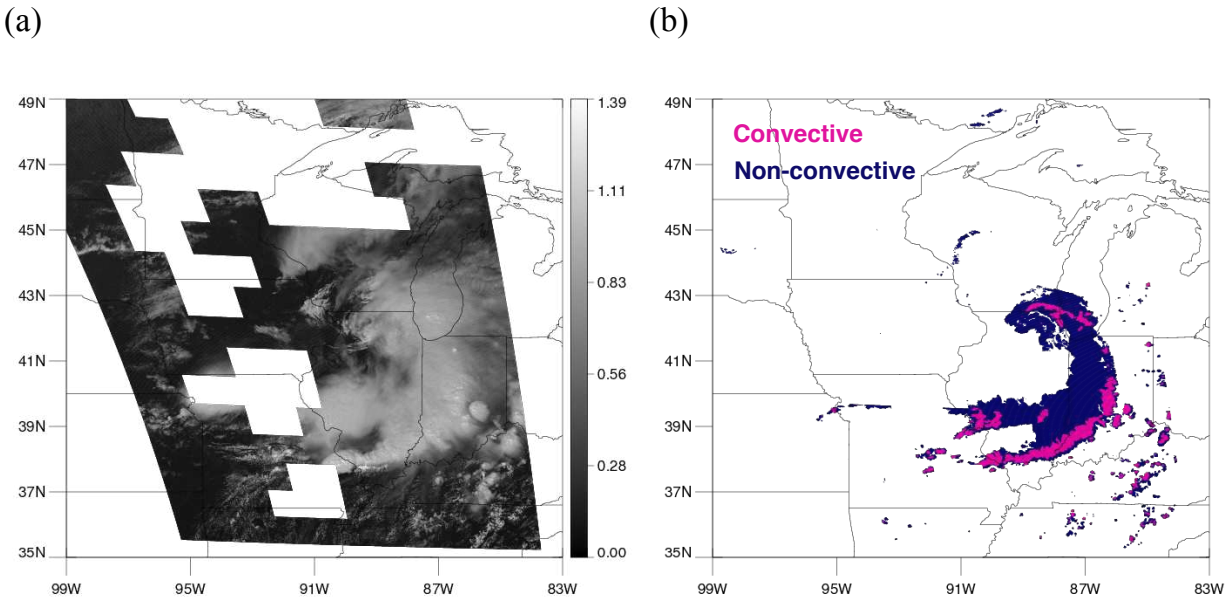

Figure 3.4 A scene at 19:00UTC on August 20th, 2019 (a) Visible imagery at channel 2 from GOES-16. (b) Precipitation type (convective or non-convective) classified by the MRMS PrecipFlag product. Tiles that do not appear on the map (missing square regions) are excluded due to low RQI.

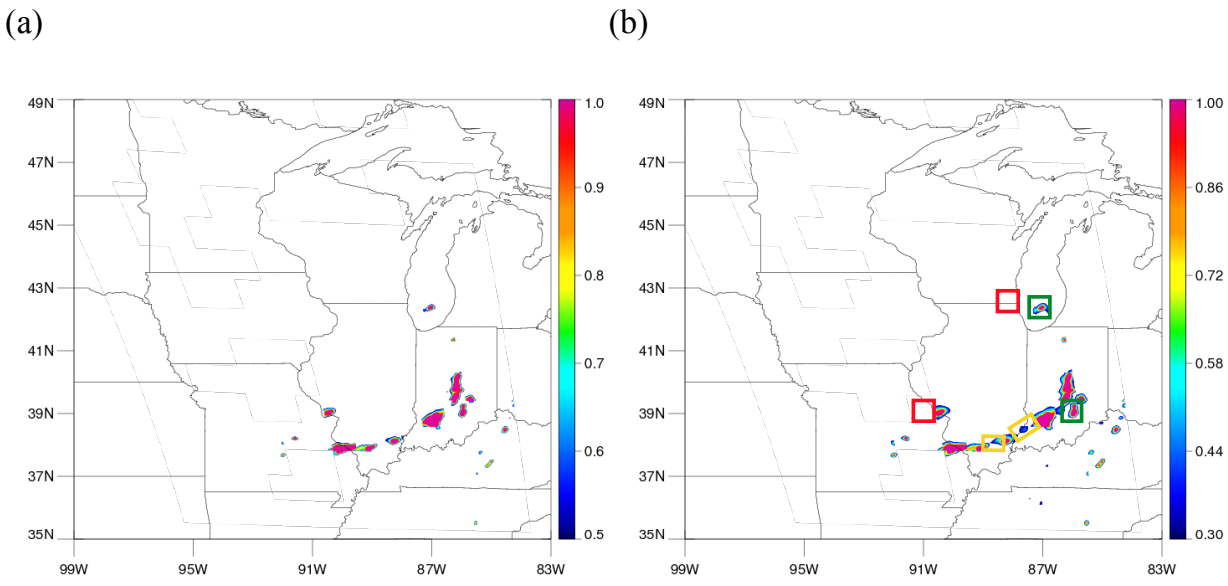

Figure 3.5 Predicted convective regions by the model using a threshold of (a) 0.5 and (b) 0.3. Colors represent a scale of being convective (1 being convective and 0 being non-convective). The colored boxes in (b) indicate six scenes selected for further study, namely two scenes that are correctly identified as convection (green boxes), two scenes detected using the threshold of 0.3, but not of 0.5 (yellow boxes), and two scenes missed at both thresholds (red boxes).

As mentioned above, the two yellow boxes in Figure 3.5b are regions that are missed by the model using a threshold of 0.5, but detected by the model using 0.3. Figure 3.6 shows a map of MRMS PrecipFlag, reflectance, and predicted results corresponding to the 128×128 tile of the yellow box on the left. In Figure 3.6c, some of the rainbands around 38°N are missed, but they appear in Figure 3.6d with the threshold of 0.3. Figure 3.7 shows a scene for the right yellow box. Again, more regions with less bubbling are predicted as convective with the threshold of 0.3.

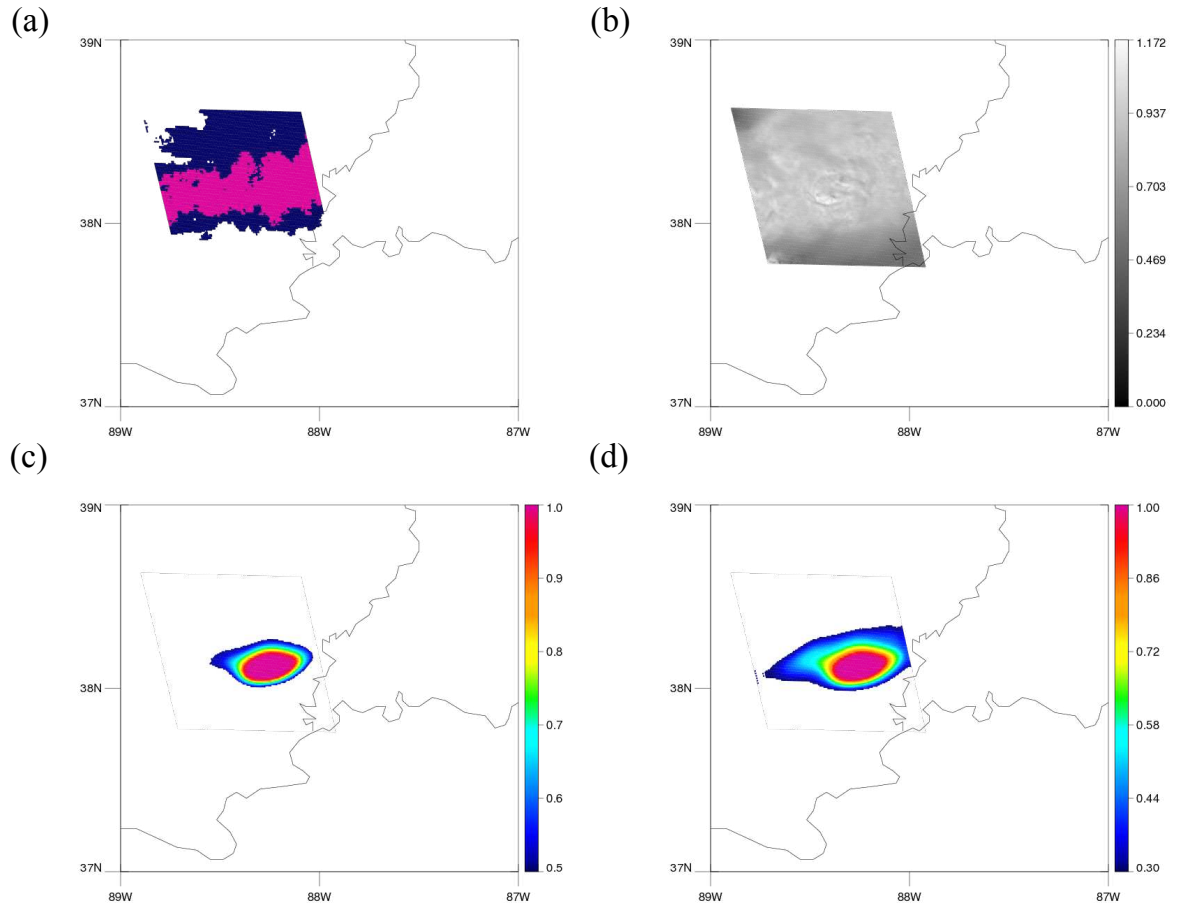

Figure 3.6 A 128×128 tile corresponding to the left yellow box in Figure 3.5b. (a) MRMS PrecipFlag. (b) Reflectance at channel 2. (c) Predicted convective regions using 0.5. (d) Predicted convective regions using 0.3.

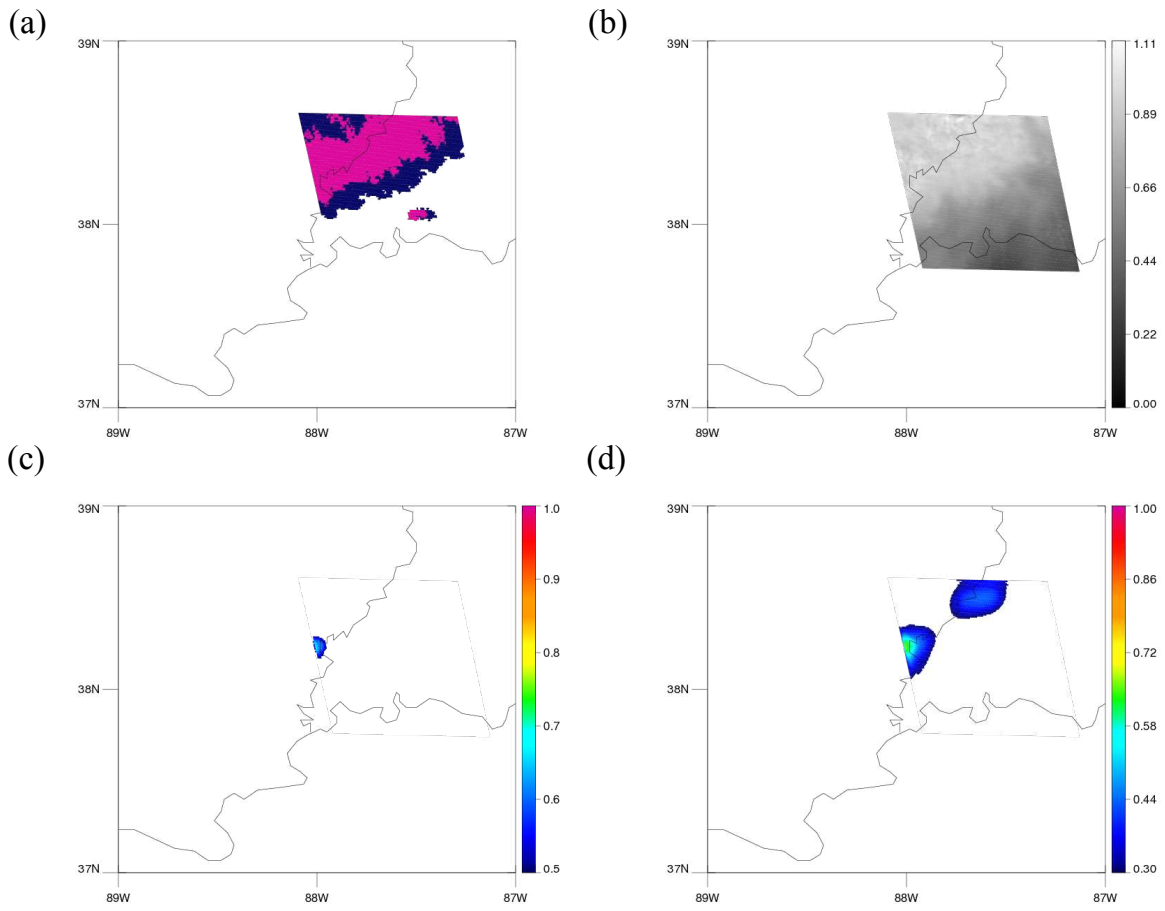

Figure 3.7 Same as Figure 3.6 but for the right yellow box in Figure 3.5b

The two green boxes in Figure 3.5b are regions that are correctly predicted by the model using both thresholds. Figure 3.8 shows 128×128 tiles for the upper green box. Although the predicted regions do not perfectly align with convective regions in MRMS, each model still predicts high values in contiguous regions around the bubbling area. Convective clouds in the lower green box show clear bubbling and even overshooting top feature in Figure 3.9b. Predicted convection using 0.5 as the threshold matches well with the bubbling regions in Figure 3.9c, while using 0.3 in Figure 3.9d predicts broader regions as convective. The region on the left in Figure 3.9d that is additionally predicted by using 0.3 does not actually show bubbling, but

MRMS also assigns it to be convective as well. Therefore, it seems that the model also learned other features that make the scene convective such as high reflectance or low brightness temperature.

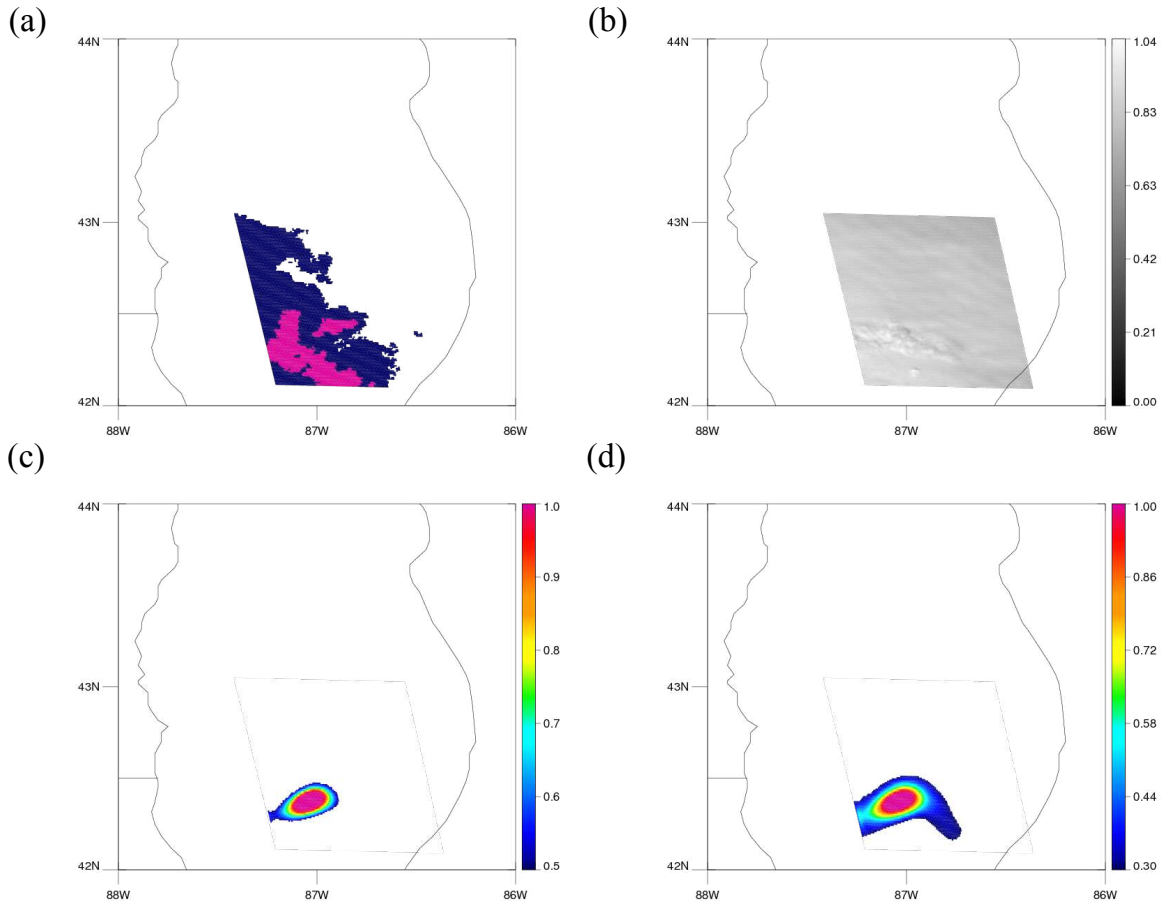

Figure 3.8 Same as Figure 3.6 but for the upper green box in Figure 3.5b.

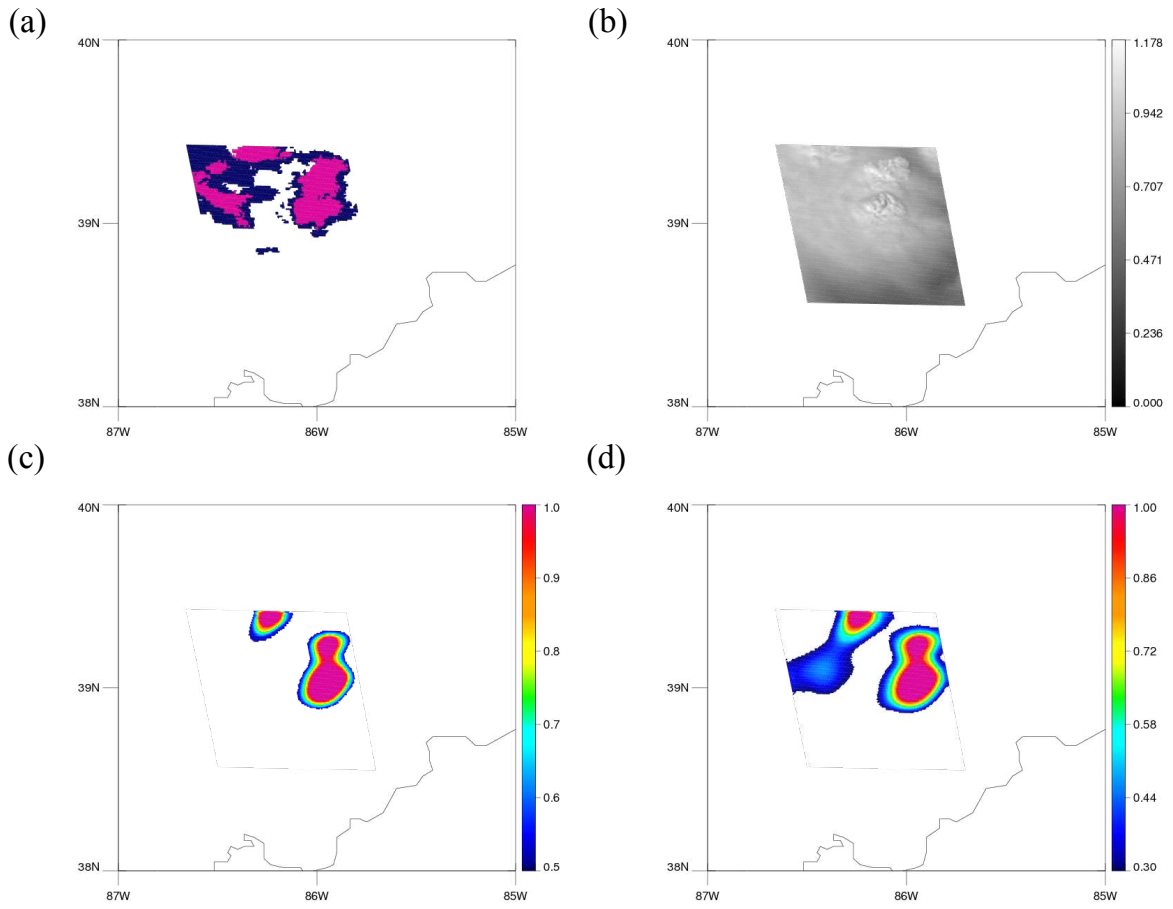

Figure 3.9 Same as Figure 3.6 but for the lower green box in Figure 3.5b.

Nevertheless, some regions are still missed even with the lower threshold, and they are shown in red boxes. Figure 3.10a and 3.10b display MRMS PrecipFlag and reflectance image of the 128×128 tile of the upper red box. While a long convective rainband is shown in the MRMS PrecipFlag, no bubbling is observed in the reflectance image even though the reflectance appears high. In addition, lower part of convection in the lower red box (Figure 3.10c and 3.10d) is also totally missed in the model prediction due to no bubbling observed in the reflectance image. These examples suggest that the model mostly looks for the bubbling feature of convective clouds to make a decision.

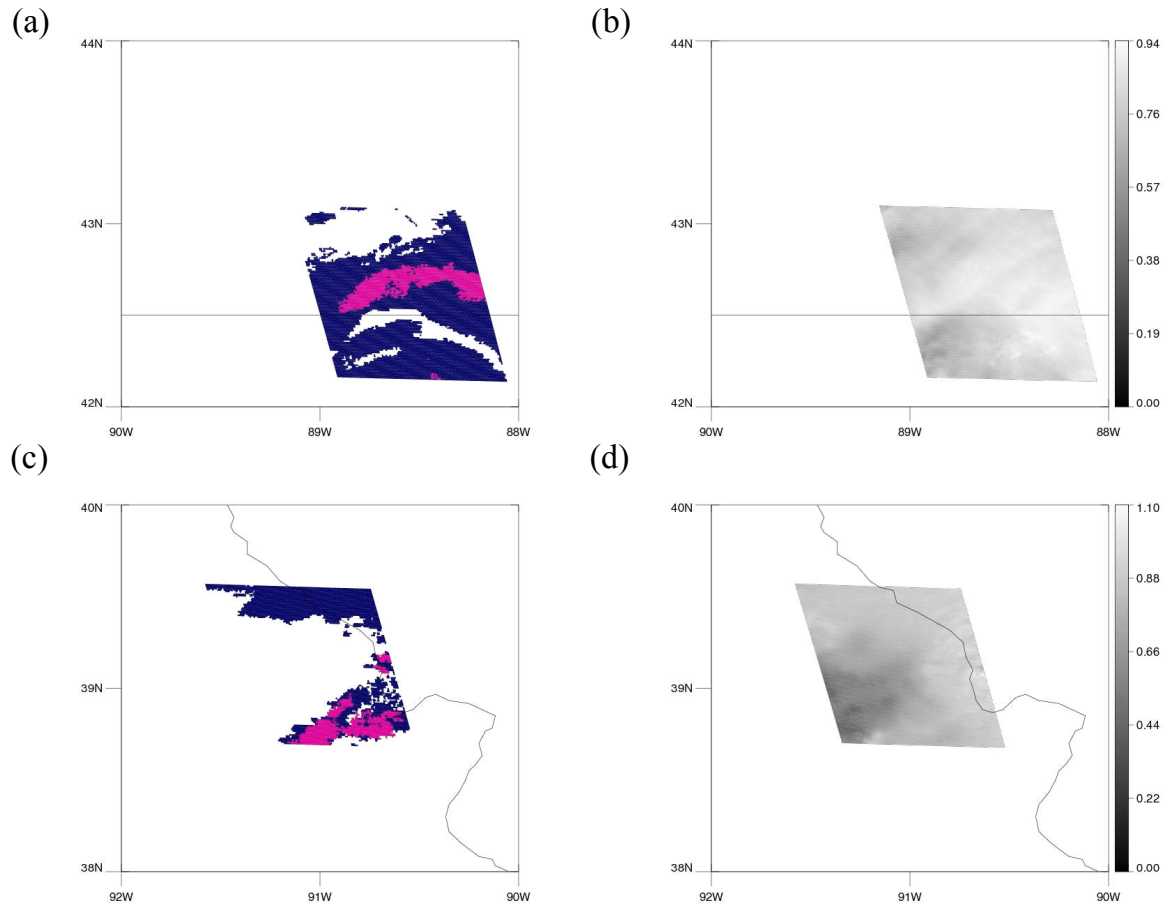

Figure 3.10 (a) MRMS PrecipFlag and (b) reflectance at channel 2 of the upper red box in Figure 3.5b. (c) MRMS PrecipFlag and (d) reflectance at channel 2 of the lower red box in Figure 3.5b.

Another scene on 24th of May, 2019 is presented in Figure 3.11. Severe storms occurred over Texas, Oklahoma, and Kansas producing hail over Texas. Unlike the previous case, most convective clouds show clear bubbling, and accordingly, FAR is very low and POD is very high in this case, even with the threshold of 0.5. With 0.5, FAR and POD are 11.0% and 89.0%, and they increase to 23.9% and 95.7% by using 0.3, respectively. More increase in FAR than in POD seems to imply that it might be wrong to use 0.3 in this case. However, the increase is mostly from detecting broader regions of mature convective clouds, and since they are further from the

convective core, sometimes they do not overlap with MRMS convective regions. In addition, earlier detection by the model than MRMS contributes to the increase. MRMS tends to define early convection as straitiform before it classifies as convective due to its low reflectivity. Convective regions in the blue boxes in Figure 3.12b are such regions that did not have strong enough echoes yet to be classified as convective by MRMS, but later they are assigned as convective from 19:12UTC once they start to produce intense precipitation. Convective regions in green boxes in Figure 3.12b are additional correctly detected regions but only with the threshold of 0.3.

(a) (b)

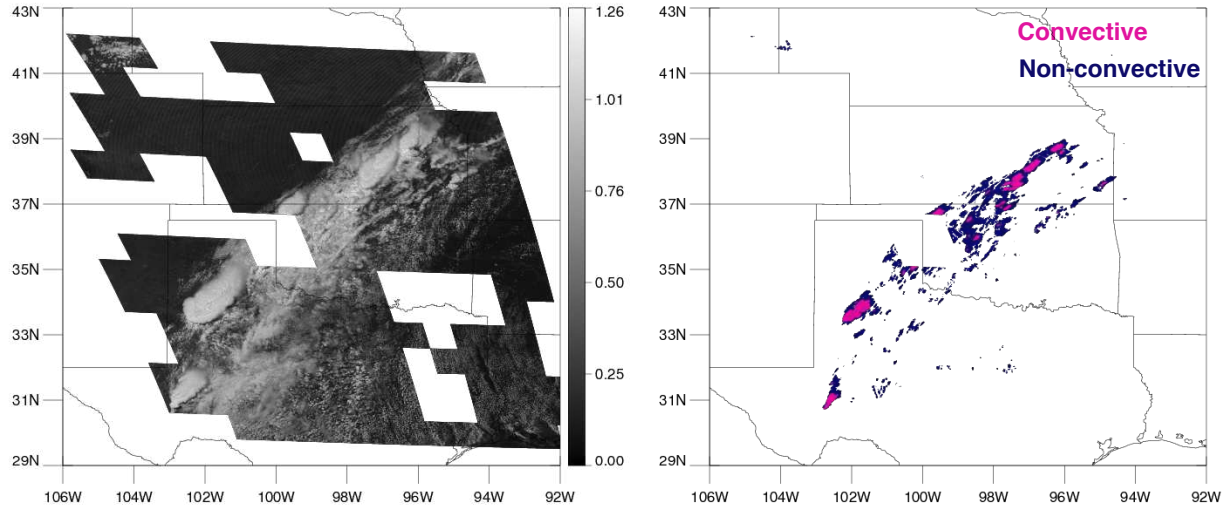

Figure 3.11 A scene at 19:00UTC on May 24th, 2019 (a) Visible imagery at channel 2 from GOES-16. (b) Precipitation type (convective or non-convective) classified by the MRMS PrecipFlag product. Again, tiles that do not appear on the map (missing square regions) are excluded due to low RQI.

(a) (b)

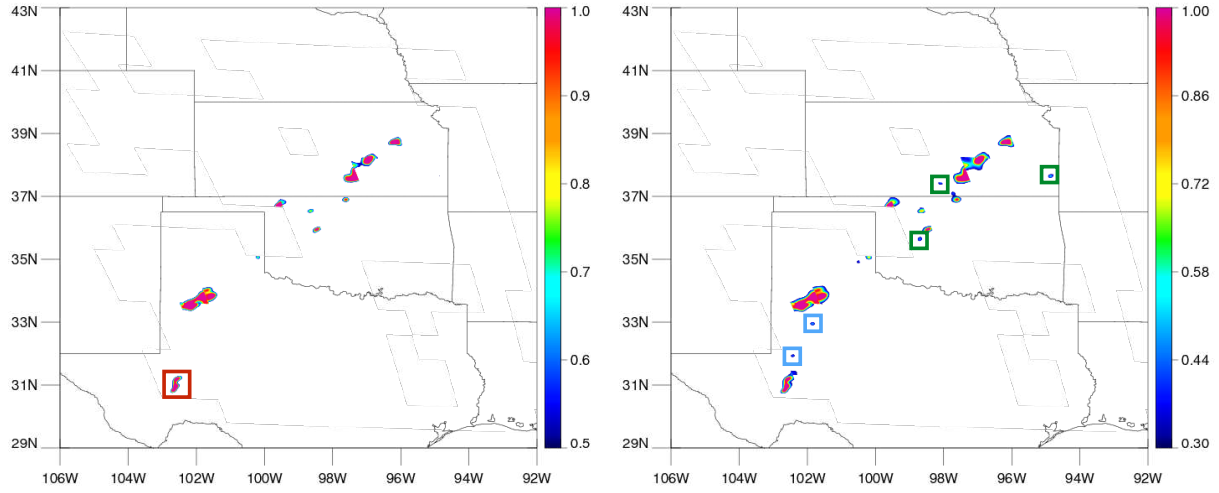

Figure 3.12 Predicted convective regions by the model using a threshold of (a) 0.5 and (b) 0.3. Colors represent a scale of being convective (1 being convective and 0 being non-convective).

Furthermore, in some true positive cases, interesting patterns are observed. Convection in the red box in Figure 3.12a is one of the true positive cases that are classified as convective both by the model and MRMS. The location of predicted convective regions matches well with MRMS. However, once the 128×128 tiles of MRMS and model detection are overlaid on reflectance image, detection area is not precisely on top of the bubbling convective core, but slightly askew. In Figure 3.13a and 3.13b, MRMS PrecipFlag and model prediction are plotted on top of the first and the last reflectance image respectively to show the temporal evolution of the convective cloud. Both MRMS and the model assign convection in the region a little to the right of the convective core and even in the dark area shadowed by the mature convective cloud. This is expected from MRMS as lumpy cloud top surfaces do not always perfectly match with precipitating location due to sheared structure of the cloud and two instruments have different views (radar from below and satellite from above), but it is surprising that the model does predict

convection in the same location as in MRMS. The model seemed to have learned about the displacement in locations and figured out where to predict convection in radar perspective. Although it is not ideal that the prediction is not made in the bubbling area, these results can be beneficial when this product is used in the short-term forecast to initiate the convection as it resembles the radar product.

(a) (b)

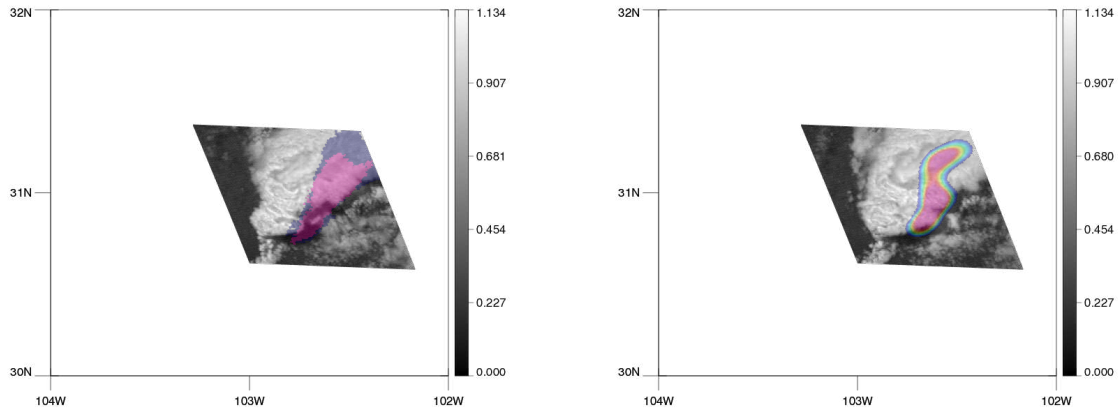

Figure 3.13 A 128×128 tile corresponding to the red box in Figure 3.12a. (a) MRMS PrecipFlag on top of the first reflectance image. (b) Predicted convective regions using a threshold of 0.5 on top of the last reflectance image.

3.5 Conclusion

An encoder-decoder type machine learning model is constructed to detect convection using GOES-16 ABI data with high spatial and temporal resolutions. The model uses five temporal images from channel 2 reflectance data and channel 14 brightness temperature data as inputs and is trained with the MRMS PrecipFlag as outputs. Low FAR and high POD are achieved by the model, considering they are calculated in 0.5km resolution. However, FAR and POD can vary depending on the threshold chosen by the user. Higher POD is accompanied by higher FAR, but it was shown that some of the additional false alarms were not totally wrong

because they are usually either the extension of mature convective clouds or earlier detection by the model. Earlier detection by the model actually raises a question whether the model is well trained for early convection. If early convections were in the training dataset with a label of stratiform, then the model could learn early convective features as the feature of stratiform. However, it seemed that the model was able to correctly learn bubbling as the main feature of convection due to much larger portions of mature convective regions in the dataset.

Unlike typical objects in classic training images for image processing, e.g., cats and dogs, that have clear edges and do not change their shapes, clouds have ambiguous boundaries and varying shapes as they grow and decay. These properties of clouds make the classification problem harder. However, bubbling feature of convective clouds are usually very clear in high spatial and temporal resolution data, and the model was able to sufficiently learn the spatial context over time within the high-resolution data, which led to good detection skill. FAR and POD presented in this study are shown to be better than results applying non-machine learning method to GOES-16 data. These results show that using GOES (or similar sensors) in identifying convective regions during the short-term forecast can be beneficial especially over regions where radar data are not available.

CHAPTER 4: LATENT HEATING PROFIELS FROM GOES-16 AND ITS COMPARISON TO HEATING FROM NEXRAD AND GPM

4.1 Introduction

As the spatial resolution of numerical weather prediction models becomes finer, and even operational models are run at resolutions of a few kilometer, an effective way to assimilate observation data at this fine resolution has been sought (Gustafsson et al., 2018). At a few kilometer resolution, convection can be resolved explicitly (Seity et al., 2011). However, if the model environment is not favorable for convection, updrafts and clouds will not develop in the right place. In order to correctly initiate convection in operational regional models where both accuracy and speed are fairly important, observed latent heating (LH) can be added in the model in the data assimilation cycle. LH is not only important to initiate convection, it also contributes to the intensification of convection. Adding LH increases buoyancy in the atmospheric column, thereby inducing convection, and it has become an important procedure that many operational models use for the initialization of convective events (Gustafsson et al., 2018).

National Oceanic and Atmospheric Administration (NOAA)'s operational models, the Rapid Refresh (RAP) and High-Resolution Rapid Refresh (HRRR), both use observed latent heating to drive convection, but in different ways (Benjamin et al., 2016). RAP uses digital-filter initialization (Peckham et al., 2016) while HRRR simply replaces modeled temperature tendency with the observed LH (Benjamin et al., 2016). For this operational purpose, LH data have to be available continuously in near-real time. Therefore, ground-based radars which have high spatial and temporal resolutions similar to HRRR's resolutions are used to calculate LH from reflectivity in HRRR. While suitable for the HRRR region of interest, the method is not

applicable to regions beyond radar coverage such as the Gulf of Mexico and even some mountainous areas. It also limits the model's applicability to global scales.

The Precipitation Radar (PR) on the Tropical Rainfall Measuring Mission (TRMM) has been used to retrieve LH from space. PR is the first meteorological radar in space, designed to provide vertical distribution of precipitation over the tropics (Kummerow et al., 1998). From its three-dimensional precipitation data, vertical profiles of LH have been retrieved. There are several retrieval algorithms using PR: Goddard Convective-Stratiform heating (CSH; Tao et al., 1993), Spectral Latent Heating (SLH; Shige et al., 2004), Hydrometeor heating (HH; Yang and Smith, 1999), and Precipitation Radar Heating algorithm (PRH; Satoh and Noda, 2001). Among these algorithms, CSH and SLH are the two most widely used products. Most recent versions of monthly gridded CSH and SLH products have spatial resolution of 0.25°×0.25° and 0.5°×0.5° respectively with 80 vertical layers and have been used to provide valuable insights to heat budget or atmospheric dynamics over Tropics. Two algorithms have improved since their first development, and both algorithms are also applied to Dual-frequency Precipitation Radar (DPR) data on Global Precipitation Measurement (GPM), the successor of TRMM, to continue the climate record of LH and expand the regions of interest to mid-latitude.

CSH and SLH both rely on the lookup table (LUT) based on cloud resolving model simulations. Inputs that are used to look for LH profiles in the LUT are different, but their common inputs to the LUT are echo top height and surface rainfall rate. Echo top height is important in determining the depth of heating in the vertical, and surface rainfall rate is a good indicator for intensity of maximum heating rate. Even though the methods use different model simulations to create the LUT, and differ in other details, they seem to exhibit similar distributions when they are averaged spatially or temporally (Tao et al., 2016).

Although these products are considered instantaneous heating, their temporal resolutions are poor compared to 15-minute or hourly observations available from ground-based radars. Geostationary data is required to achieve the sampling of ground-based radars. The visible and infrared sensor on geostationary satellite, unfortunately, cannot provide much vertical information as active sensor do in the presence of thick clouds, but their data contain cloud top information, and rapid refresh provides important information about a cloud's convective nature. Cloud top information from geostationary data is included when creating cloud analysis during data assimilation (Benjamin et al., 2016), and thus LH retrieved based on cloud top temperature, can be useful in the forecast model by keeping consistency of retrieved LH with the updated cloud analysis.

This study examines if cloud convective identification from the cloud's one-minute evolution from the Advanced Baseline Imager (ABI), coupled with cloud top information on Geostationary Operational-Environmental Satellite-16 (GOES-16), can be sufficient to approximate NEXRAD-derived LH. Following the lead of spaceborne radar LH algorithms, a LUT is created using model simulations. Once convective clouds are determined by using 10 consecutive one-minute ABI data, LH profiles for convective clouds are looked for in the LUT based on cloud top temperature of the convective cloud. Unlike DPR products that has temporal resolution of a day, ABI data in mesoscale sector are provided with one-minute interval, and thus LH can be obtained from GOES-16 as frequently as NEXRAD, thereby eligible for initiating convection during the forecast. LH from GOES-16 can be beneficial over the regions without radar such as ocean or mountainous regions where the quality of radar data degrades.

Detailed descriptions of CSH, SLH and how NEXRAD converts reflectivity to LH are provided, followed by the retrieval process using GOES-16 ABI. LH from GOES-16 are then examined to see if it is comparable to other radar products.

4.2 Existing LH retrieval methods

4.2.1 Radiosonde networks

LH is not a measurable quantity as it is almost impossible to single out temperature changes by phase changes from the total observed temperature changes. However, heat and moisture budget studies are conducted using sounding network in a field campaign, and apparent heat source (Q_1) and apparent moisture sink (Q_2) from the budget study are related to LH (Yanai et al., 1973; Johnson 1984; Demott 1996). It can be done using a diagnostic heat budget method which is first presented by Yanai et al. 1973 (Tao et al., 2006). Over a certain horizontal area, Q_1 can be expressed as the equation below that includes LH (Tao et al., 2006)

$$Q_1 - Q_R = \bar{\pi}\left[-\frac{1}{\bar{\rho}}\overline{\left(\frac{\partial \bar{\rho} w'\theta'}{\partial z}\right)} - \overline{\nabla \cdot V'\theta'}\right] + \frac{1}{c_p}\left[L_v(c-e) + L_f(f-m) + L_s(d-s)\right] \qquad (4.1)$$

where prime denotes deviations from horizontal averages, which is denoted by upper bar. Q_R is the radiative heating rate, θ is potential temperature, π is non-dimensional pressure, ρ is air density, c_p is specific heat at constant pressure and R is gas constant for dry air. L_v, L_f, and L_s represent the latent heats of condensation, freezing, and sublimation while c, e, f, m, d, and s represent each microphysical process of condensation, evaporation, freezing, melting, deposition, and sublimation, respectively. The last six terms on the right-hand side that include these microphysical processes are LH from phase changes. Since Q_1 can be obtained using vertical profiles of temperature, moisture, and wind data observed during the field campaign (Tao et al.,

2006), the observed Q_1 is used to indirectly validate GPM LH products that are retrieved together with Q_1.

4.2.2 CSH and SLH from GPM DPR

DPR has two operational LH algorithms: the Goddard Convective-Stratiform Heating (CSH) and Spectral Latent Heating (SLH). In the GPM products, LH is provided along with additional variables: Q_1-Q_r and Q_2 in SLH and Q_1-Q_r-LH, Q_r, and Q_2 in CSH (Tao et al., 2019). These algorithms are first developed for TRMM data, but have been adapted to GPM data. Both algorithms use cloud resolving model simulations to create a LUT relating hydrometeor profiles to cloud model heating rates. Although there is no direct measurement for LH to validate the results, retrieved Q_1 and Q_2 are compared instead with sounding data from various field campaigns through a method mentioned in section 2.1. The evolution of these products is well summarized in (Levizzani et al., 2020), but each algorithm is briefly explained here.

The Goddard Convective-Stratiform Heating (CSH) is first introduced by Tao et al. 1993. Initial algorithm by Tao et al.1993 uses surface rainfall rate and amount of stratiform rain as inputs to the LUT, but the LUT has been improved by increasing the number of LH profiles, using finer resolution in simulations, and adding new inputs such as echo-top heights and low-level vertical reflectivity gradients (Tao et al., 2019). For high-latitude regions observed by GPM satellite, new LUT is created with simulations from NASA Unified-Weather Research and Forecasting model which is known to be suitable for high latitude weather system (Levizzani et al., 2020). Inputs to this LUT are surface rainfall rate, maximum reflectivity height, freezing level height, echo top height, decreasing flag, and maximum reflectivity intensity (Levizzani et al., 2020).

The SLH algorithm is based on Shige et al. 2004 and Shige et al. 2007. For tropical regions, the LUT is created for three different rain types; convective, shallow stratiform, and anvil (or deep stratiform) clouds. Inputs to the LUT are precipitation top height (PTH), precipitation rate at the surface (P_s), precipitation rate at the level that separates upper-level heating and lower-level heating (P_f) and precipitation at the melting level (P_m). Once non-convective rain is separated into either shallow stratiform or anvil, a vertical profile for anvil cloud is chosen based on P_m, and magnitudes of upper level heating and lower level cooling are normalized by P_m and (P_m - P_s), respectively. For convective and shallow stratiform clouds, a vertical profile corresponding to the PTH is chosen, and then upper-level heating and lower-level heating are normalized by P_f and P_s, respectively. For DPR, a new LUT is created for mid and higher latitude to account for expanded latitudinal coverage by GPM. For higher latitude regions, six precipitation types (convective, shallow stratiform, three types of deep stratiform, and other) instead of three are used, and therefore six respective LUTs exist. Inputs to these LUTs are precipitation type, PTH, precipitation bottom height, maximum precipitation, and P_s.

Figure 4.1 shows monthly gridded products from these two algorithms over CONUS for July of 2020 at four different heights. Overall horizontal pattern in the two products looks similar. However, there is a difference in the vertical. At 5km or 8km, CSH tends to show higher heating rate especially over mid-latitude, while at 10km, SLH shows higher heating rate. In addition, SLH tends to have larger cooling rate throughout the layers, although it is not clear from the figure. These discrepancies would be attributed to different configuration setup such as microphysical scheme used to run simulations for the LUT. This again shows that there is no true heating rate that we can trust, and vertical profiles of LH highly depend on the simulations that comprise the LUT.

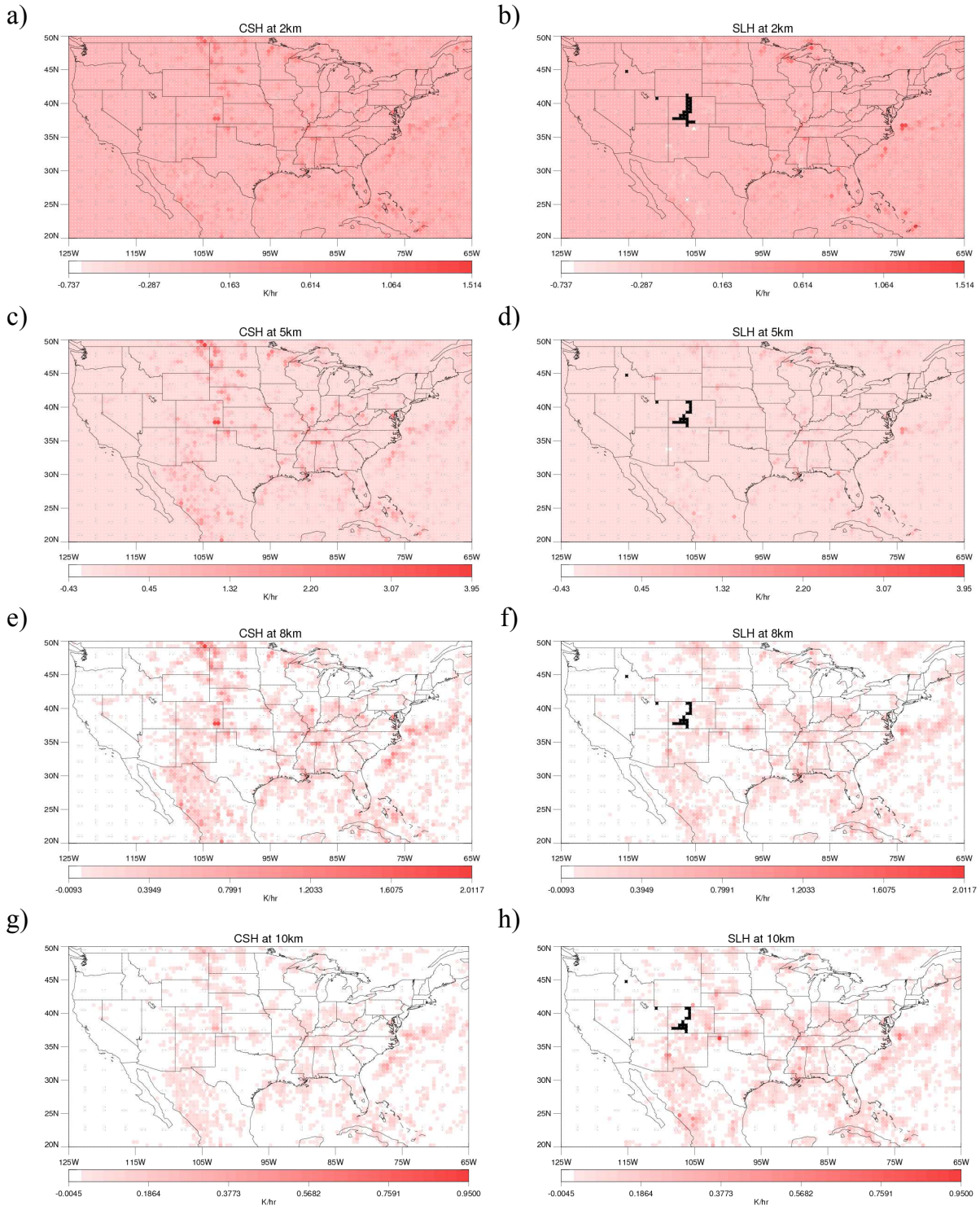

Figure 4.1 Monthly gridded LH from CSH at (a) 2km, (c) 5km, (e) 8km, and (g) 10km and LH from SLH at (b) 2km, (d) 5km, (f) 8km, and (h) 10km.

Orbital data for these products have finer spatial resolution of 5km, but their temporal resolution is too coarse to be used in the forecast model, which typically has a spatial resolution of few kilometers and time step of few seconds. The closest that can meet the resolutions of the forecast model is ground-based radar data, and this is the reason why LH derived from ground-based radar is used to initiate convection during the short-term forecast.

4.2.3 LH from NEXRAD

In the operational forecast model, LH profiles retrieved using radar reflectivity replace modeled LH profiles so that appropriate heating rate can help initiate convection. LH profiles in this case are obtained through a simple empirical formula that converts radar reflectivity to LH. In Equation (4.2), reflectivity is converted to potential temperature tendency using model pressure field. This equation is only applied when radar reflectivity exceeds 28dBZ. The threshold of 28dBZ was chosen based on the effectiveness of adding heating from reflectivity in HRRR (Bytheway et al., 2017).

$$T_{ten} = \frac{1000}{p}^{R_d/c_{pd}} \frac{(L_v+L_f)Q_s}{n \cdot c_{pd}} \qquad (4.2)$$

where $Q_s = 1.5 \times \frac{10^{z/17.8}}{264083}$

z : grid radar/lightning-proxy reflectivity

T_{ten} : temperature tendency

p : background pressure (hPa)

R_d : specific gas constant for dry air

c_{pd} : specific heat of dry air at constant pressure

L_v : latent heat of vaporization at 0°C

L_f : latent heat of fusion at 0°C

N : number of forward integration steps of digital filter initialization

T_{ten} in Equation (4.2) is produced in K/s to meet the needs during the short-term forecast. Although heating rate is not a general output in the forecast model, it is calculated every time step by dividing temperature change from microphysical scheme by time step which is usually on the other of few tens of seconds. Therefore, this empirical formula is developed to produce LH comparable to the modeled heating rate in K/s so that added LH does not blow up the model when it is ingested.

4.3 LH profiles from GOES-16

Current operational geostationary satellite, GOES-16, carries the Advanced Baseline Imager (ABI), an instrument with 16 VIS and IR channels. Mesoscale sectors, which are manually moved around to observe interesting weather events, provide data in one-minute intervals. Such high temporal resolution data have helped observe cloud developments in more detail. Using this high temporal resolution ABI data, convective clouds are detected, and LH profiles for the detected clouds are assigned from a lookup table. The lookup table is created running the Weather Research and Forecasting (WRF) model simulations. While CSH and SLH algorithm look for LH profiles in a model-based LUT according to precipitation type and precipitation top height, the LUT for GOES is created for convective clouds that appear bright and bubbling from ABI according to brightness temperature at channel 14 (11.2μm), which is a good indicator of cloud top temperature. LH is not assigned for stratiform clouds from GOES-16 as it is not important in initiating convection in the forecast. Once convective clouds are detected using temporal changes in reflectance and brightness temperature, LH profile corresponding to the T_b of the detected cloud is assigned from the LUT.

4.3.1 Definition of convection in GOES-16 ABI and model simulations

When using LH to drive convection in the operational forecast model, LH derived from radar reflectivity is applied only in convective regions. In HRRR, a simple threshold of 28dBZ determines where to put LH, but there is no such simple threshold for visible or infrared channels that can determine convective regions. However, there are several convection detecting algorithms for GOES-16 ABI, including Lee et al. 2020a. It uses mesoscale sector data with one-minute interval to detect convections from ABI. Two separate detecting methods are proposed for vertically growing clouds in early stages and mature convective clouds that move rather horizontally once it reaches the tropopause and often have overshooting tops. The method for vertically growing clouds measures T_b decrease over ten minutes for two water vapor channels, and if the decrease is greater than the designated threshold, it assigns the pixel as convective. For mature convective clouds, the method looks for grid points that have continuously high reflectance, low brightness temperature, and lumpy cloud top over ten minutes. Combining the two methods provides results comparable to radar product, and these methods are rather simple and fast. Therefore, this algorithm is used to detect convective regions from ABI.

However, this method is not applicable to model simulations due to unreliable reflectance simulated by the CRTM. Instead, convection is defined with vertical velocity, which is one of prognostic variables in the model. It is actually the most direct and accurate way to define convection (Zipser & Lutz, 1994; LeMone &Zipser, 1980; Xu & Randall, 2001; Wu et al., 2009; Delgenio et al., 2010; Schumacher et al., 2015), but not widely used since vertical velocity is not always available in observation data. A threshold is usually defined at a certain altitude or over certain range of altitudes for a general use. However, vertical velocity tends to peak at different height at different stages of convection (Schumacher et al. 2015), and not one altitude works for

all the convection. Therefore, an appropriate threshold for the model simulation that is also consistent with the observed scene is determined in this study, not pursuing values from previous studies.

T_b at 11.2μm which is used to construct the LUT is mostly sensitive to hydrometeors or water vapor. Accordingly, the signal received by the channel will be largely from layers with high cloud water contents. Considering that cloud water is produced after an updraft followed by condensation, an altitude that has maximum cloud water contents can be regarded as an altitude with the strongest updraft. Since vertical velocity at a layer with maximum cloud water contents can be beneficial in both determining convection at all stages and matching with the observation, it is used in this study with a threshold that can keep consistency between model outputs and observation. The threshold is chosen comparing fractions of convective regions. Table 4.1 shows convective fractions using the GOES-16 convection detecting algorithm and using different vertical velocity thresholds in the model outputs. Using higher thresholds can prevent including non-convective grids, but at the same time, it will only include the strongest part of convective regions. Using 1.5m/s shows a fraction closest to the observed fraction, and therefore, 1.5m/s is used to define convection in the model output. This number is actually similar to values used in some previous studies (1m/s in LeMone and Zipser 1980, Xu and Randall 2001, and Wu et al., 2009)

Table 4.1. Fraction of convective regions in observation and using different vertical velocity thresholds in the model output.

Observation	1m/s	1.5m/s	2m/s	3m/s	4m/s
0.96%	1.53%	1.04%	0.77%	0.47%	0.31%

4.3.2 Model simulations used to create a lookup table

11 convective cases are simulated using WRF to obtain stable mean LH profiles. The convective cases are chosen over CONUS within NEXRAD network during May to August in 2017 or 2018. All simulations use the same configuration in Table 4.2 to avoid discrepancy between simulation results, and their T_bs at 11.2μm are calculated using the Community Radiative Transfer Model (CRTM). In each scene, convective grid points are defined by the threshold found in the previous section, and neighboring convective grid points are clustered to form a convective cloud. Minimum T_b of each cloud is calculated, and LH profiles from the clouds with the same minimum T_b are averaged to produce mean profiles for each T_b bin of the LUT. LH profiles gathered in the LUT are provided in K/s as for NEXRAD.

Table 4.2. Table for WRF simulation setup.

Version	WRFv3.9
Spatial resolution	3km
Time step	10 seconds
Microphysical scheme	Aerosol-aware Thompson scheme (The original scheme is modified to produce vertical profiles of LH as outputs)
Planetary boundary layer	Mellor-Yamada Nakanishi Niino (MYNN) Level 2.5 and Level 3 schemes
Land surface model	Rapid update cycle (RUC) land surface model
Long wave and short wave radiation physics	Rapid radiative transfer model for general circulation models (RRTMG) schemes

4.3.3 Mean LH profiles according to cloud top temperature

LH profiles of convective clouds from 11 WRF simulations are collected according to 16 bins of the minimum cloud top temperature at 11.2μm. 16 bins range from below 200K to above 270K with a bin size of 5K. Figure 4.2 shows mean vertical profiles of LH in each bin. All profiles exhibit slightly negative LH near the ground due to evaporation, but positive LH is shown at most layers. It is also nicely shown in the figure that as the T_b decreases, the profile stretches up in the vertical. Interestingly though, the maximum heating rate is not perfectly proportional to T_b. However, considering the maximum LH that is allowed in HRRR model, which is 0.02K/s, these values seem quite reasonable. Table 4.3 shows average of maximum surface precipitation rate and mean surface precipitation rate for each bin. Precipitation rate is mostly inversely proportional to T_b in Table 4.3. This is expected as deeper and higher clouds tend to precipitate more. This again shows that mean LH profiles for each bin are properly obtained from GOES-16.

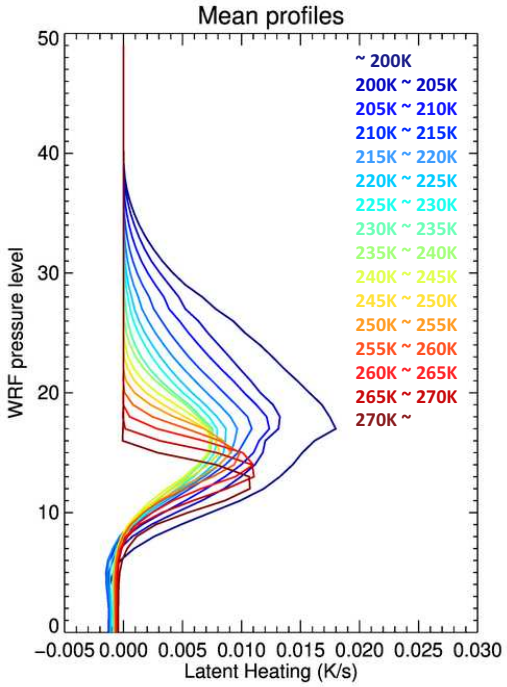

Figure 4.2 Mean vertical profiles for each cloud top temperature bin.

Table 4.3. Table of maximum precipitation rate and mean precipitation rate for each cloud top temperature bin.

	Maximum precipitation rate (mm/hour)	Mean precipitation rate (mm/hour)
~200K	137.4	48.8
200K ~ 205K	99.7	41.2
205K ~ 210K	88.0	47.2
210K ~ 215K	60.9	40.0
215K ~ 220K	41.6	30.3
220K ~ 225K	31.1	23.5
225K ~ 230K	24.9	18.9
230K ~ 235K	20.1	15.5
235K ~ 240K	16.4	12.6
240K ~ 245K	14.0	13.4
245K ~ 250K	10.8	10.9
250K ~ 255K	10.4	10.9
255K ~ 260K	7.9	7.4
260K ~ 265K	6.4	6.0
265K ~ 270K	4.8	4.1
270K ~	3.4	3.1

4.4 Comparisons between products

LH from three different instruments, GOES-16, NEXRAD, and DPR are examined for comparison. Methods using GOES-16 and DPR products are similar in a way that they use cloud top height or PTH to look for mean profiles in the LUT created with model simulations, although DPR has additional parameters such as surface rain rate which is used to vary the magnitude of the heating rate. In contrast, NEXRAD uses an empirical formula to convert radar reflectivity to LH regardless of PTH. They are all instantaneous heating, but provided in different units. LH from GOES-16 and NEXRAD is in K/s to easily match with modeled heating rate, while DPR

products are in K/hour. Therefore, LH in K/hour from DPR products are converted to K/s for comparison.

A scene on 18th June, 2019 is shown in Figure 4.3 to compare how each product determines precipitation type (convective or stratiform) which is a one of the major factors in estimating LH profiles. The regions with reflectivity greater than 28dBZ in Figure 4.3a are regions where LH is estimated from NEXRAD reflectivity to be used in HRRR, but not necessarily convective regions. These regions are larger than convective regions defined by DPR products in Figure 4.3c and include some of the stratiform regions assigned by DPR. Pink regions on top of visible image at channel 2 (0.65μm) in Figure 4.3b are convective regions detected by GOES-16, and they encompass smallest regions compared to others. Even though areal coverage differs by the method, locations of convective core matches well between the products.

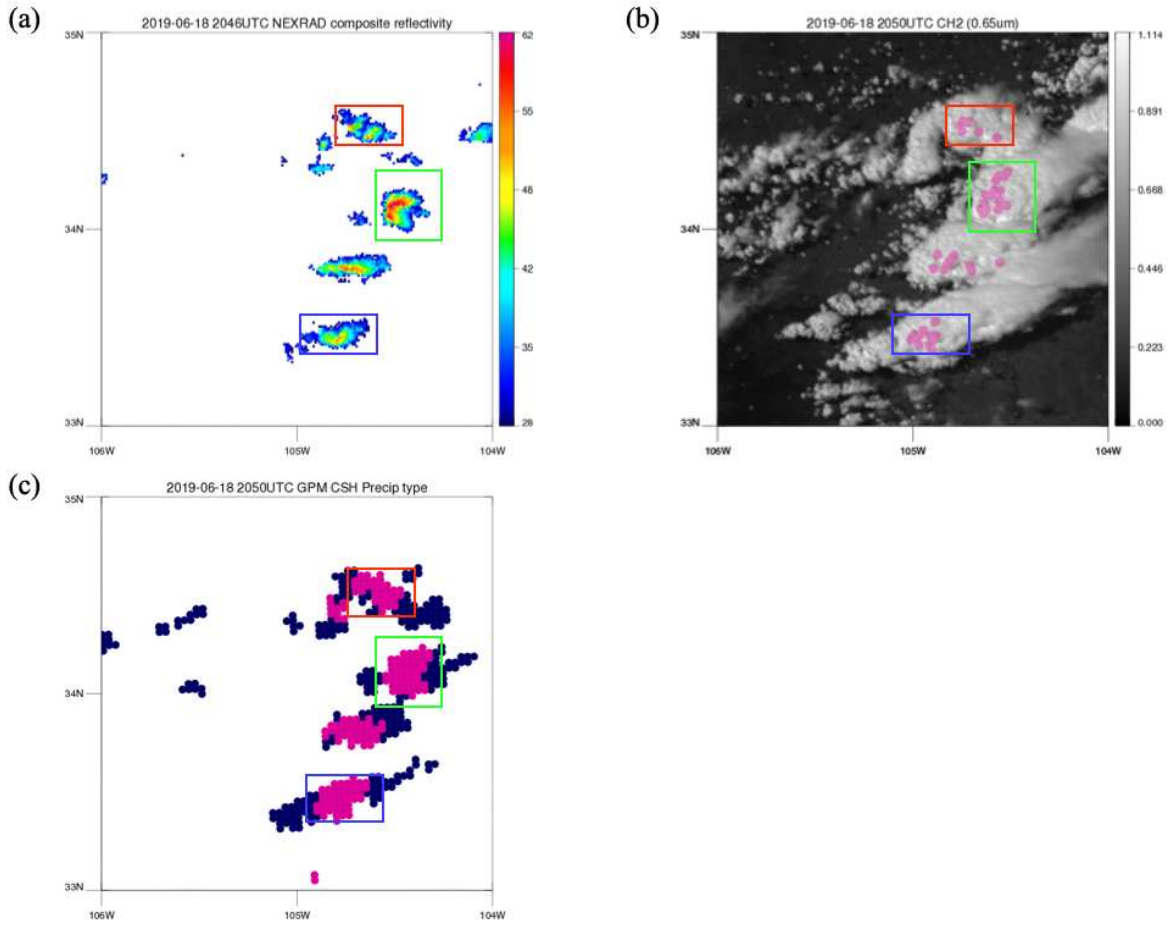

Figure 4.3 A scene on June 18st, 2019. (a) NEXRAD composite reflectivity. Only the regions with reflectivity greater than 28dBZ are shown with colors. Color bar is in dBZ. (b) Convective regions detected by GOES-16 are colored in pink on top of GOES-16 visible image at channel 2 (0.65μm). (c) Precipitation type defined by CSH. Convective regions are colored in pink while stratiform regions are colored in navy.

Clouds in colored boxes in Figure 4.3 are all convective clouds, but in different evolutional stages. Clouds in red, green, and blue box respectively have high, low, and mid-level cloud top temperature. LH profiles from NEXRAD, GOES-16, and CSH for these clouds are interpolated into the same WRF grid with 3km resolution for comparison in Figure 4.4, 4.5, and 4.6. CSH and SLH provide LH for both convective and stratiform regions, and thus different colors of lines in Figure 4.4c, 4.5c, and 4.6c represent different cloud type. Lines with light blue

color are each LH profiles of convective grid points in the red box, and blue line is the mean of these profiles. Similarly, LH profiles of each stratiform gird point are in light green, and the mean of these profiles is in dark green. The total mean LH profile is colored in red. Convective LH profiles from CSH shows heating throughout the vertical layers as expected, except near the surface due to evaporation at lower levels. LH profiles in stratiform regions show cooling at low levels below a melting level and heating above. LH profiles from GOES-16 corresponding to the three convective clouds are shown in Figure 4.4b, 4.5b, and 4.6b, light blue line being each profile and blue line representing the mean. Even though mean profile is assigned from GOES-16 for each convective cloud, a number of different lines are shown in the figure due to spatial interpolation. When LH profiles from GOES-16 and CSH are compared, mean profile of convective LH from CSH in blue (Figure 4.4c, 4.5c, and 4.6c) is similar to GOES LH in red (Figure 4.4b, 4.5b, and 4.6b) both in terms of the magnitude and the vertical shape.

On the other hand, LH from NEXRAD shows different vertical shape from GOES-16 or CSH which uses the LUT consisting of model simulations. LH profiles from GOES-16 or CSH peak around the middle of the atmosphere while NEXRAD LH in convective core (Figure 4.4a, 4.5a, and 4.6a) tends to peak at low levels where radar reflectivity is high. At low levels where model simulations have cooling, NEXRAD LH does not show cooling due to Equation (4.2) which is designed to only produce positive values. This heating at lower levels can help increase buoyancy in lower atmosphere, and thus, convection can be effectively initiated from the added heating.

Although their vertical shape is different, the magnitude of LH is within similar magnitude. Overall values of mean LH profile from NEXRAD in red is slightly smaller than mean profile from GOES-16 or mean convective LH profile from CSH (blue line), but are closer

to the total mean profile of CSH (red line), which indicates that 28dBZ threshold might include some stratiform regions as well. Smaller mean of NEXRAD LH is mainly attributed to anvil regions where reflectivity greater than 28dBZ only exist at few vertical layers and 0dBZ elsewhere.

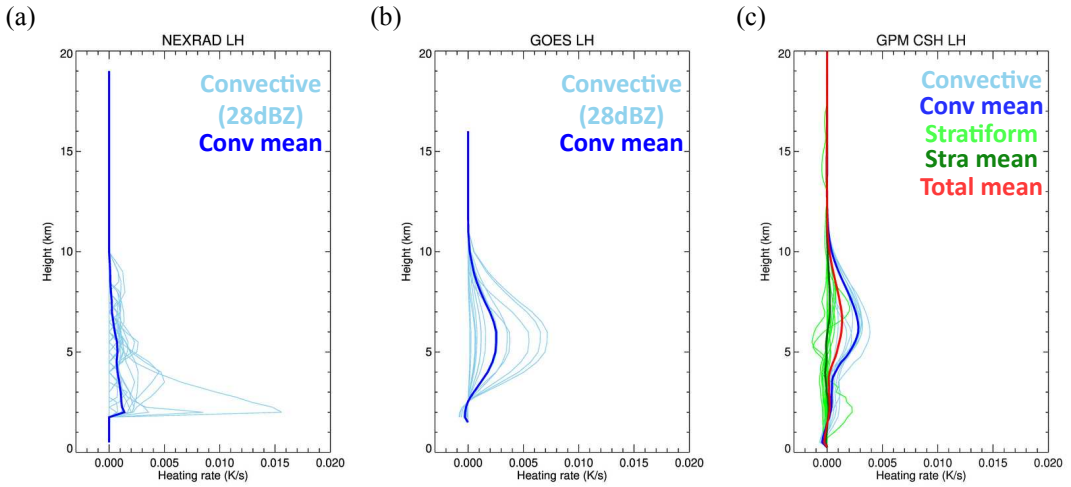

Figure 4.4 LH profiles from (a) NEXRAD, (b) GOES-16, and (c) CSH for the red box region. Light blue lines in (a) and (b) are each LH profile and blue line is a mean profile of the light blue lines. In (c), each LH profile for convective grid point is colored in light blue and the mean of these lines are colored in blue while each LH profile for stratiform grid point is colored in light green and its mean profile is colored in dark green.

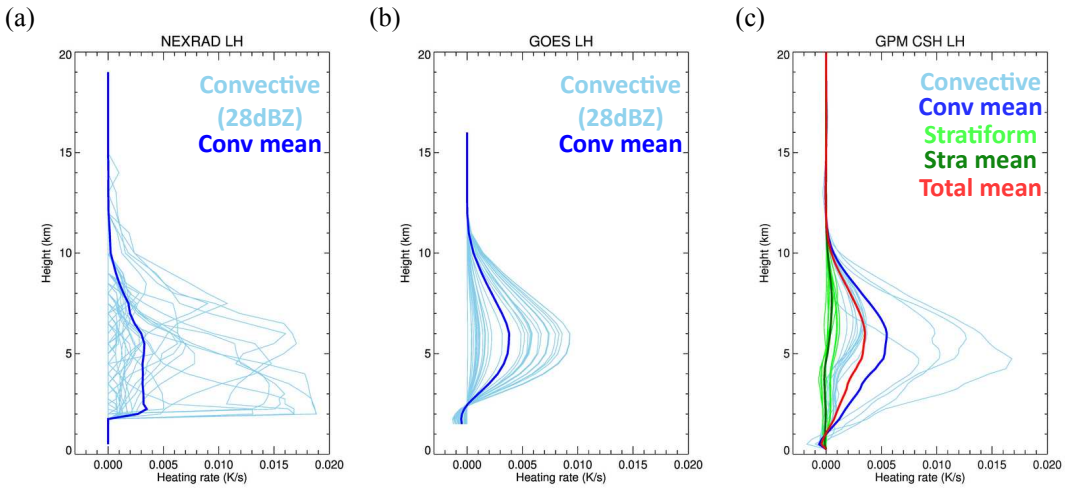

Figure 4.5 Same as Figure 4.4, but for the green box region.

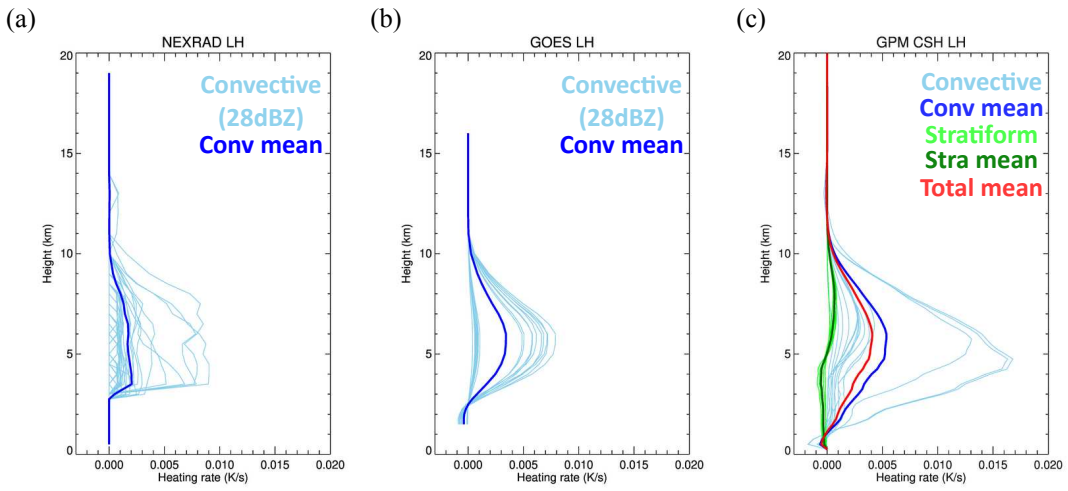

Figure 4.6 Same as Figure 4.4, but for the blue box region.

Even though the mean LH from NEXRAD is smaller, the total LH for the region can be similar when it is added up over the region due to broader area determined by the threshold of 28dBZ in Figure 4.3a than GOES-16 detection in Figure 4.3b. Therefore, the total LH of each cloud is compared between GOES-16 and NEXRAD. Figure 4.7 shows vertical profiles of LH that is horizontally summed over each convective cloud, each color representing colors of the three box regions. As mentioned before, the altitude that LH peaks is different, but the magnitude of the total heating is very similar. Finally, the total LH of each region is obtained by summing up the vertical profiles in Figure 4.7 and presented in Table 4.4. The total LH is shown to be similar between NEXRAD and GOES-16. Despite the smaller mean LH from NEXRAD that was shown in Figure 4.4, 4.5, and 4.6, it shows a good agreement in total heating between GOES-16 and NEXRAD.

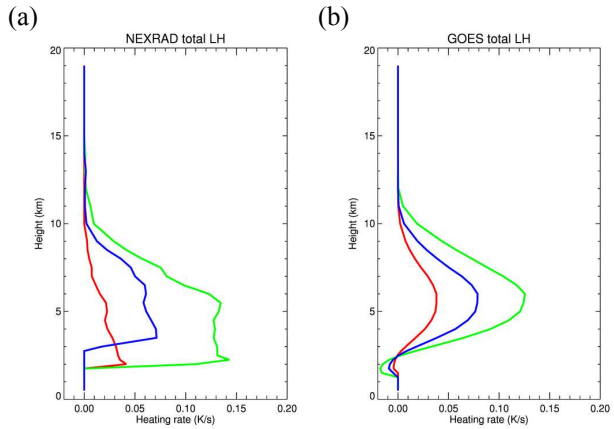

Figure 4.7 Vertical profiles of the total heating in the boxed regions from (a) NEXRAD and (b) GOES-16. Different colors represent the color of the box region.

Table 4.4. Total LH (K/s) from NEXRAD and GOES-16 in the red, green, and blue box regions.

	Red	Green	Blue
NEXRAD	0.31	1.41	0.68
GOES-16	0.34	1.83	0.64

4.3 Conclusions

A method to obtain vertical profiles of LH from GOES-16 ABI data was described. Convective clouds are first detected using temporal changes in reflectance and brightness temperature, and LH profiles for the detected cloud is found by searching a LUT created using WRF model simulations. The LUT contains LH profiles of convective clouds that are defined by a threshold of 1.5m/s for the modeled vertical velocity, and these convective LH profiles are sorted according to T_b at 11.2μm, which is a good indicator of cloud top height. Mean profiles that represent each T_b bin show good correlation with cloud top temperature, with lower the T_b bin having deeper LH profiles. Precipitation rates corresponding to each bin are also well correlated to T_b. In addition, maximum LH in the LUT is well within the range that is allowed in HRRR to initiate convection using NEXRAD.

Even though this method is not designed for assigning LH profiles at each grid point as radar products do, it can assign mean values for each cloud. Since the convection detection method for GOES-16 tends to detect convective core region, each cloud is defined separately by combining neighboring grid points, and mean LH is assigned for the cloud. LH from GOES-16,

NEXRAD, and CSH are compared in three convective clouds with different cloud top heights. Vertical profiles of convective LH from GOES-16 are very similar to those from CSH that use model simulations in the LUT. Their vertical profiles show heating throughout the vertical layer except near the surface where evaporation occurs, and heating peaks around the middle of the atmosphere. This vertical pattern differs from when using an empirical formula with radar reflectivity. Vertical profiles of LH from NEXRAD highly depend on vertical profiles of reflectivity which typically peaks near surface in convective regions, and thus, maximum LH is usually observed at lower level, which is not commonly shown in the modeled heating rate. Even though their vertical shape is slightly different, the total LH over convective clouds is shown to be similar. Similar magnitude of LH between GOES-16 and NEXRAD suggests a potential use of LH from GOES-16 in initiating convection in the regions where ground-based radar data are not available.

CHAPTER 5: IMPACTS OF LATENT HEATING OBTAINED FROM GOES-16 IN THE WRF MODEL

5.1 Introduction

Numerical weather prediction model has experienced tremendous improvements over the past decades with the help of enhanced computing resources and advanced technology to make high quality observation data (Bauer et al., 2015). Since weather system is highly non-linear, and even a small change in initial condition can impact forecast result significantly, observation data have been assimilated to guide the model into the right direction. Plenty of observation data are available around the globe, but depending on the purpose, different types of observation data need to be assimilated, and how to assimilate data has become as important as what to assimilate. Reanalysis data include as many observation data as possible as its goal is to provide the best quality of data for a long-term record and for validation purpose. On the other hand, operational models need to carefully select a type of observation data or an assimilation method to reach a compromise between accuracy and speed.

In operational models, one of the most important variable forecast is precipitation as it can cause damage even if correctly forecasted. Precipitation-related products are assimilated in the model, but they are mostly ground-based observation such as ground-based radars or meteorological aerodrome reports (METARs). Cloud-affected satellite data are not as much used due to less vertical information in presence of thick clouds (Gustafsson et al., 2018). However, these data from space are certainly useful as it is not affected by topography and not all regions have dense ground-based radar network.

Current operational forecast models at National Oceanic and Atmospheric Administration (NOAA), Rapid Refresh (RAP) and High-Resolution Rapid Refresh (HRRR), include precipitation-affected observation data, but only to infer cloud top properties. RAP is run to cover North America with a spatial resolution of 13km and provide boundary conditions for HRRR, which has smaller spatial resolution of 3km and run only over Contiguous United States (CONUS). Cloud analysis in RAP during the one-hour assimilation cycle is created assimilating data from METAR, geostationary satellite, and ground-based radars (Benjamin et al., 2016). Cloud top information from infrared sensor on geostationary satellite is used to infer cloud top temperature and pressure while METAR and radars are used to assign hydrometeor water contents at each level (Benjamin et al., 2016). Followed by hydrometeor assimilation, three-dimensional profiles of latent heating (LH) retrieved from radar reflectivity is assimilated through a digital filter initialization technique in RAP. HRRR also uses LH profiles, but not through digital filter initialization. HRRR simply replaces the prognostic temperature tendency from microphysical scheme with the observed LH profiles every 15 minute. This helps trigger convection where high reflectivity is observed by radar. Where to put these LH profiles is determined using a threshold of 28dBZ. Even though this threshold does not necessarily indicate convective regions, it is found to effectively initiate convection in HRRR.

LH for HRRR is obtained from an empirical formula that converts reflectivity to temperature change in K/s. Since HRRR uses reflectivity from Next Generation Weather Radar (NEXRAD) which is a ground-based radar over CONUS, LH is not available over ocean or the quality degrades over mountainous regions. Especially, the southern part of the United States suffers from storms that develop over Gulf of Mexico during the summer, and lack of data over the region can lead to degrading forecast quality compared to forecast made over land.

Geostationary satellite data are still available over such regions even though it only carries passive sensors that are lack of vertical information. However, current operational geostationary satellite, Geostationary Operational Environmental Satellite (GOES)-16, can observe convective activity more in detail with high temporal and spatial resolutions. A method from Chapter 4 derives LH profiles from GOES-16 by detecting convective cloud using one-minute data and finding a profile for the cloud in the lookup table based on the cloud top temperature. Even though vertical distribution of LH is different between NEXRAD and GOES-16, the amount of total heating over the same cloud is shown to be similar.

This study examines impacts of using LH from GOES-16 in the Weather Research and Forecasting (WRF) Model. Fraction skill score, which is one of the neighbourhood-based precipitation verification metrics, is used to validate the results against one-hour accumulated rain from Multi-Radar/Multi-Sensor System (MRMS). Results using LH from GOES-16 and NEXRAD are compared to examine whether LH from GOES-16 behaves similarly to LH from MRMS, and it can be used to improve forecast over regions without radar coverage. Two case studies are presented in the study: one over CONUS that has high quality NEXRAD data and one over Gulf of Mexico. The case with radar coverage is used to demonstrate its ability to improve forecast as NEXRAD does, and the case over Gulf of Mexico is presented to show the potential to improve forecast over Gulf of Mexico where radar data are not available. Section 5.2 and 5.3 explains how LH is obtained from GOES-16 and NEXRAD, followed by description of MRMS that is used for validation in section 5.4. Experiment setup is delineated in section 5.5, and comparison between experiments for two case studies are presented in section 5.6.

5.2 Latent heating from GOES-16

GOES-16 carries the Advanced Baseline Imager (ABI) which has 16 channels from visible to infrared range. Reflectance at channel 2 has the finest spatial resolution of 0.5km, and other visible or near-IR channels and IR channels have a spatial resolution of 1km and 2km, respectively. ABI is run in three operation modes of full disk, CONUS, and Mesoscale. Although mesoscale sector covers small portion of 1000km×1000km domain, it has the finest temporal resolution of one minute. This study uses mesoscale sector data to exploit its high temporal resolution to the full extent. Using this data, however, limits the analysis to be for short period since the mesoscale sector is manually moved around to observe regions with interesting weather.

This study follows a convection detection method by Lee et al. 2020a. They use 10 consecutive one-minute mesoscale sector data to detect convection. Their method to detect actively growing clouds finds a region with a shape of convective storm, and if the cloud shows decrease in brightness temperature over time at either channel 8 (6.2μm) or 10 (7.3μm), then it defines as convective cloud. Other method from the study that detects mature convective clouds uses continuously high reflectance at channel 2 (0.65μm), low brightness temperature at channel 14 (11.2μm), and lumpy cloud top texture seen from channel 2 to detect convection. Once convective clouds are detected by these methods, following Chapter 4, LH is obtained from a lookup table according to the cloud top temperature of the convective cloud.

5.3 Latent heating from NEXRAD

NEXRAD is an operational radar network that is available over CONUS and few other regions. HRRR uses radar reflectivity from NEXRAD to retrieve vertical profiles of LH with

following Equation (5.1), and the retrieved LH is added in the regions with reflectivity higher than 28dBZ to initiate convection.

$$T_{ten} = \frac{1000}{p}^{R_d/c_{pd}} \frac{(L_v+L_f)Q_s}{n \cdot c_{pd}}, \qquad (5.1)$$

where $Q_s = 1.5 \times \frac{10^{z/17.8}}{264083}$

z : grid radar/lightning-proxy reflectivity

T_{ten} : temperature tendency

p : background pressure (hPa)

R_d : specific gas constant for dry air

c_{pd} : specific heat of dry air at constant pressure

L_v : latent heat of vaporization at 0°C

L_f : latent heat of fusion at 0°C

N : number of forward integration steps of digital filter initialization

This study implements HRRR way of adding heating from radar to compare results adding GOES-16 LH.

5.4 Multi-Radar/Multi-Sensor System (MRMS)

MRMS developed at NOAA's National Severe Storms Laboratory provide high-quality precipitation-related data. It is created by integrating radar mosaic from the NEXRAD with atmospheric environment data, satellite data, lightning, and rain gauge observations (Zhang et al., 2016). One-hour accumulated rain from MRMS is used for validation, along with the radar quality index from MRMS, which is an indicator for radar quality in the region and ranges from 0 to 1. Regions with radar quality index less than 0.5 are excluded when validating the result.

5.5 Model experiments

WRF model is run for two case studies with a configuration summarized in Table 5.1. HRRR analysis data every hour are used as initial boundary condition over a 500×500 (1500km×1500km) domain.

Table 5.1. Summary of WRF configuration.

Version	WRFv3.9
Spatial resolution	3km
Time step	10 seconds
Microphysical scheme	Aerosol-aware Thompson scheme (The original scheme is modified to produce vertical profiles of LH as outputs)
Planetary boundary layer	Mellor-Yamada Nakanishi Niino (MYNN) Level 2.5 and Level 3 schemes
Land surface model	Rapid update cycle (RUC) land surface model
Long wave and short wave radiation physics	Rapid radiative transfer model for general circulation models (RRTMG) schemes

Three experiments are run for each case study using different LH in the WRF model: control (CTL), GOES-16 LH (GL), and NEXRAD LH (NL). WRF model is run from at least six hours before adding LH to allow a spin up time. In GL and NL runs, LH from GOES-16 or MRMS are added in the model during the day when LH can be obtained from GOES-16 ABI visible and infrared data. As HRRR puts radar derived heating every 15 minutes, LH profiles from GOES-16 or MRMS are replaced with the modeled LH profiles every 15 minute whenever there is observation.

5.6 Results

Results are validated against one-hour accumulated rain from MRMS using one of the neighbourhood-based precipitation verification metrics, which is fraction skill score (FSS). FSS

is introduced by Roberts and Lean (2008) to assess precipitation forecast skill with respect to different spatial scale used in the evaluation. It is less strict than the traditional verification metrics that does a grid by grid comparison such as root mean square error as it takes neighboring grid points into consideration. $FSS_{(n)}$ over a $N_x \times N_y$ domain is defined as

$$FSS_{(n)} = 1 - \frac{\frac{1}{N_x N_y}\sum_{i=1}^{N_x}\sum_{j=1}^{N_y}[O_{i,j} - P_{i,j}]^2}{\frac{1}{N_x N_y}\left[\sum_{i=1}^{N_x}\sum_{j=1}^{N_y} {O_{i,j}}^2 + \sum_{i=1}^{N_x}\sum_{j=1}^{N_y} {P_{i,j}}^2\right]}, \qquad (5.2)$$

where $O_{i,j}$ and $P_{i,j}$ are respectively an observed and model forecast fraction calculated over a small $n \times n$ domain. A value of n determines the number of neighboring grid points that is allowed when comparing with observation. These fractions can be calculated by dividing the number of grid points that meet a certain threshold by the total number of grid points of $n \times n$. FSS ranges between 0 and 1, 1 being the prefect forecast. In this study, FSS values are calculated for several thresholds of 0.01 (0.254), 0.1 (2.54), 0.25 (6.35), 0.5 (12.7), and 1 (25.4) inch/hour (mm/hour) over 5×5 domain (15km×15km).

5.6.1 Case study on 10th July, 2019

On 10th July, 2019, severe thunderstorms developed throughout the southcentral region of the United States. Maps of brightness temperature at 11.2μm from GOES-16 and mosaic composite reflectivity from NEXRAD at 22UTC are shown in Figure 5.1 to describe the scene. Mesoscale sector of GOES-16 was able to observe these storms as well as a small portion of a tropical system developed over Gulf of Mexico, which eventually became Hurricane Barry.

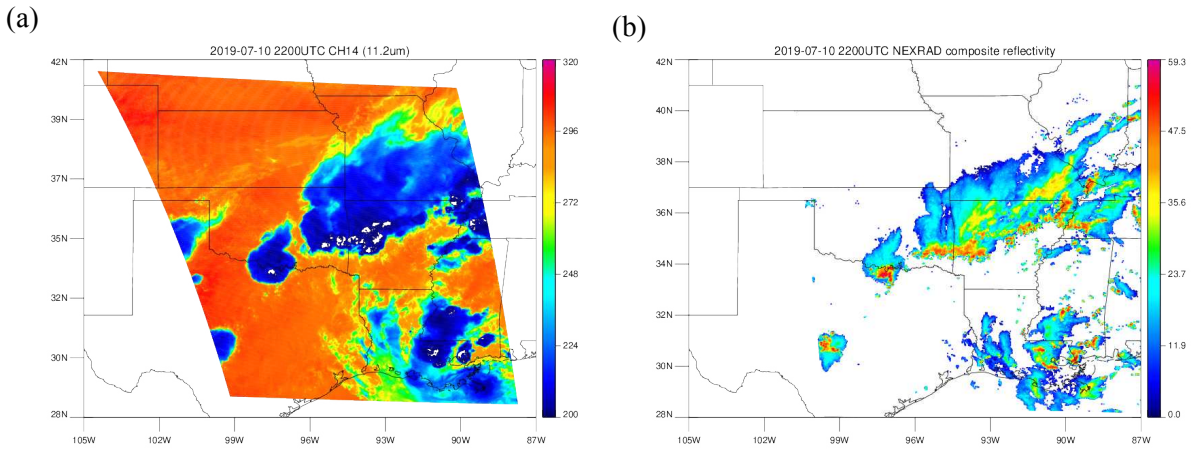

Figure 5.1 A scene on 10th July, 2019. (a) GOES-16 brightness temperature (K) at channel 14. (b) NEXRAD composite reflectivity (dBZ).

FSS is calculated from 14:00UTC when LH from GOES-16 and NEXRAD is added to 00:00UTC on 25th July and shown in Figure 5.2. Black, red, and blue lines represent CTL, NL, and GL runs, respectively. Both NL and GL show improvements in FSS for most of the thresholds. In this case, LH from NEXRAD is most effective in initiating convection as its FSS is increased significantly, but it seems that LH is not sufficient to develop into a deep convective storm and produce heavy rain. LH from GOES-16 is not as good as NEXRAD LH in initiating convection, but it is better in producing deep convective clouds. This is further examined through comparing LH from GOES-16 and NEXRAD and resulting one-hour accumulation rain from MRMS.

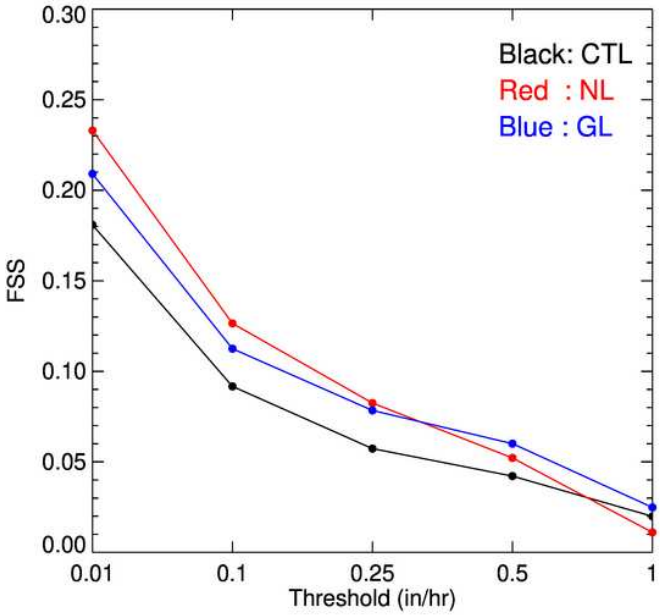

Figure 5.2 FSS calculated over a scene on 10th July, 2019 for CTL (black), NL (red), GL (blue) runs.

Maximum LH from GOES-16 and NEXRAD at 22:30UTC is shown in Figure 5.3. As discussed in Chapter 4, GOES tends to put higher LH in smaller area while NERAD tends to put smaller LH in larger area. One-hour accumulation rain at 23:00UTC that would have been affected by LH in Figure 5.3 is presented in Figure 5.4. More rain is produced in the blue box region for GL and NL runs as it should since heating is added, but GL run produces more rain in this region as in observation. In the green box region, GL run does not produce rain on the left half of the region, even though it adds LH, but it produces more rain than NL run on the right half of the region. Similarly, in the red box region, both runs produces more rain than CTL run, but convection is initiated in larger area by NEXRAD LH. These results can be explained by larger magnitude of LH from GOES-16 or different vertical distribution between GOES LH and NEXRAD LH. GOES LH tends to peak at higher level than NEXRAD LH because NEXRAD

LH is exponentially proportional to reflectivity, which usually peaks at low levels in convective regions. Therefore, LH added at higher level in GL can lead to deeper convection, while LH added at lower level in NL can initiate convection in more area determined by 28dBZ.

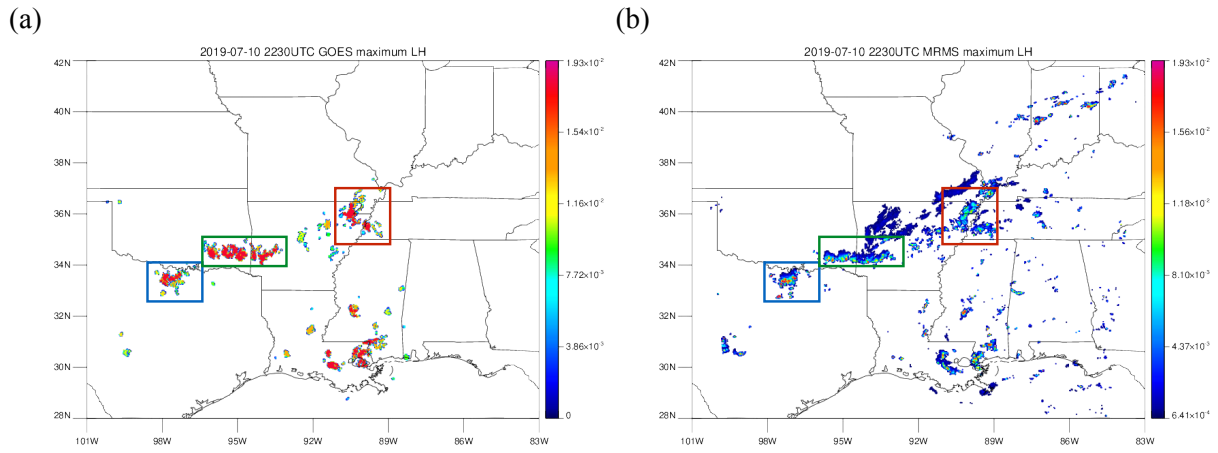

Figure 5.3 Maximum LH over the scene by (a) GOES-16 and (b) NEXRAD.

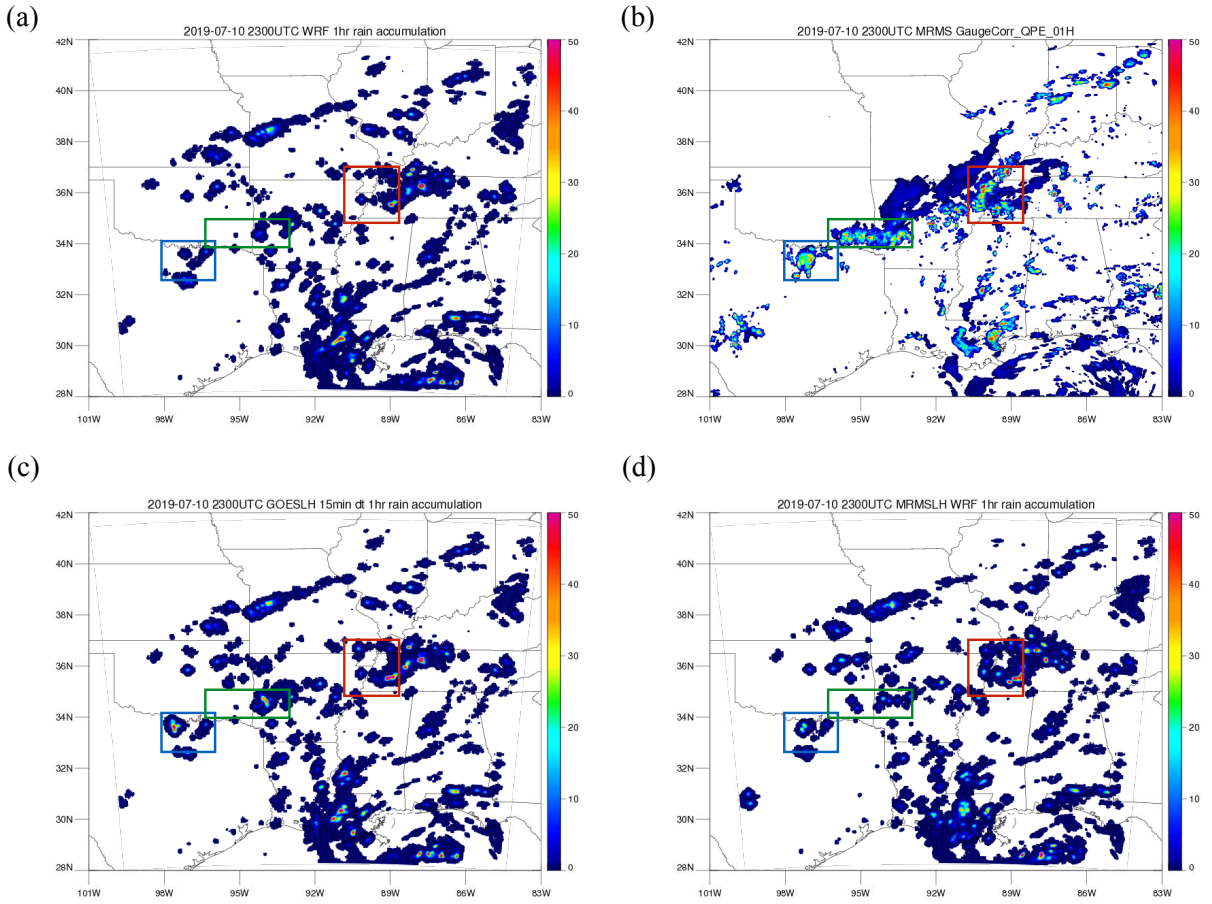

Figure 5.4 One-hour accumulated rain (mm/hour) on 10th July, 2019 2300UTC from (a) CTL, (b) MRMS, (c) GL, and (d) NL.

5.6.2 Case study on 24th July, 2019

On 24th July, 2019, sea breeze storms started over Gulf of Mexico moved east, producing heavy rainfall on Florida. This is a case where GOES-16 data might be useful as there is no continuous radar observation over the Gulf of Mexico. Even though radar data is limited in this case, it is still compared to GL runs. Figure 5.5 is a plot of FSS for CTL, NL, and GL runs. In this case, since radar data are lacking in regions where storms are moving from, GL run generally shows more improvements than NL run. As the added heating in GL run induces

convection over the west of Florida and it moves to the east, more precipitation is produced over Florida in GL run. This is shown in Figure 5.6 where one-hour accumulated rain from MRMS and CTL, NL, and GL runs at 16:00UTC is compared. Overall, GL tends to produce more light rain as in MRMS, especially over red and green box regions, but deeper convection is developed than it should over the red box region. This again is possibly due to more LH added in upper level in convective regions in GL run. Nevertheless, in this case, LH added over Gulf of Mexico in GL run seems to help bringing moisture to Florida from West.

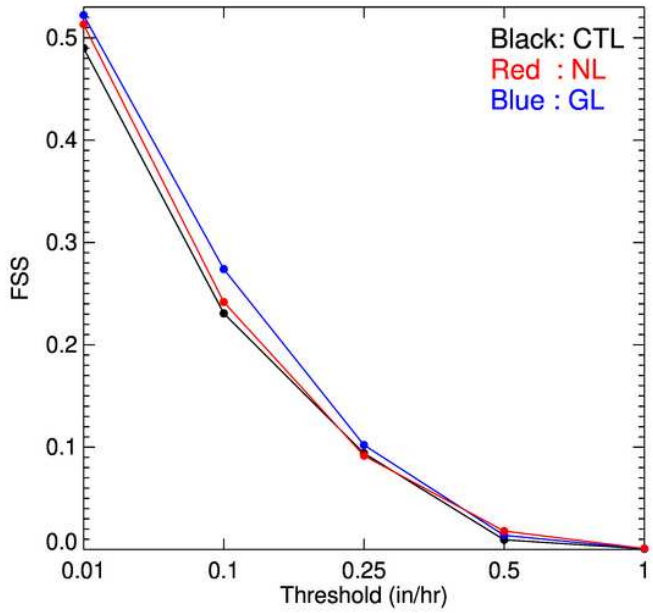

Figure 5.5 FSS calculated over a scene on 24th July, 2019 for CTL (black), NL (red), GL (blue) runs.

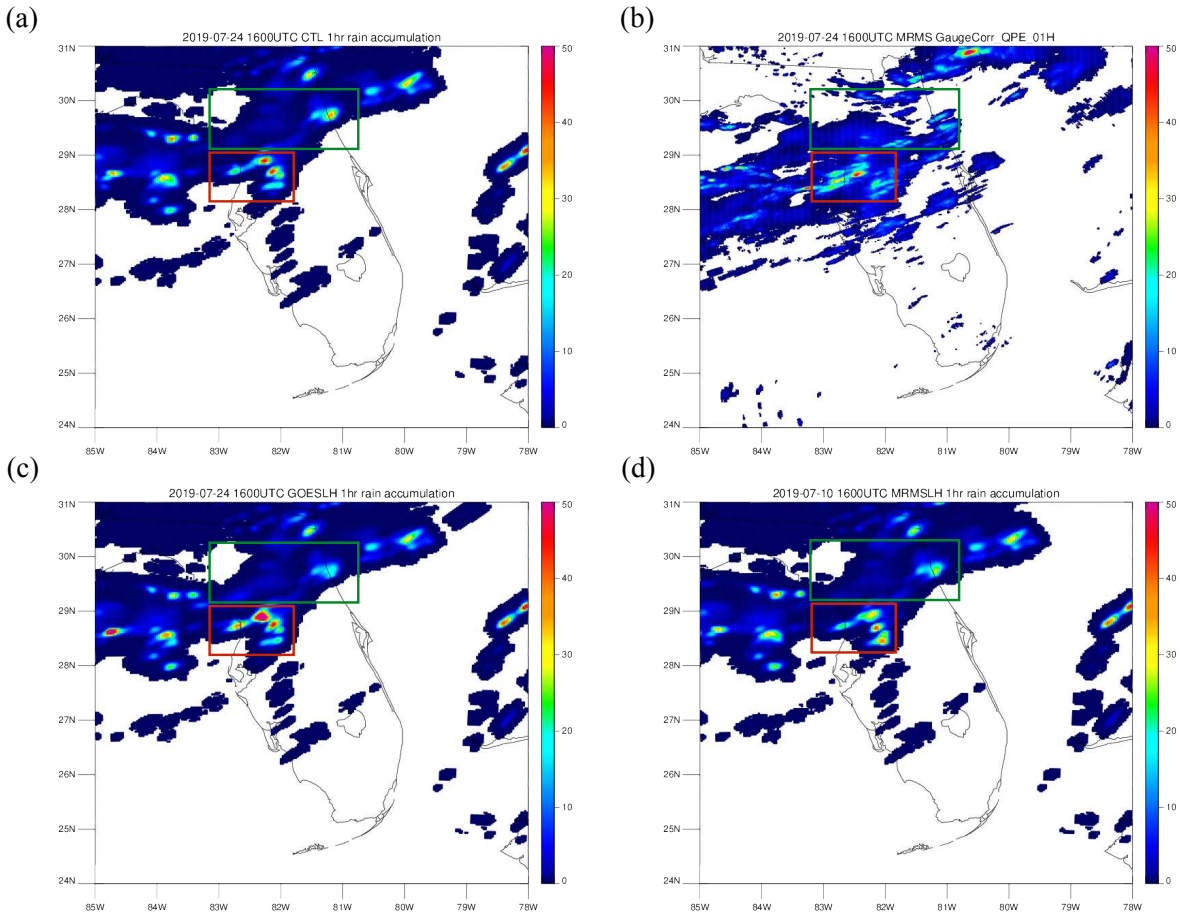

Figure 5.6 One-hour accumulated rain (mm/hour) on 24th July, 2019 1600UTC from (a) CTL, (b) MRMS, (c) GL, and (d) NL.

5.7 Conclusion

Results from two case studies suggests that adding LH from GOES-16 behave similarly as radar and can improve forecast. NL run results in higher FSS in the first case study, but in the second case study when radar data are not available in the region where convection develops, GL run shows higher FSS. In both cases, GL run generally shows improvements, but sometimes it produces deeper convection than it should. Even though the magnitudes of LH from GOES-16 and NEXRAD are similar, size or intensity of convective cloud that develops from adding LH is different possibly due to different height that LH is added. NEXRAD puts heating at lower level

thereby helping initiate convection while GOES-16 puts heating at higher level, which makes it effective in generating deep convection.

5.8 Summary

This study suggests another way to use precipitation-affected data from geostationary satellite. Over land, reflectivity from ground-based radar is used to estimate LH and initiate convection by adding LH in the forecast model. Although a lot of regions over the globe do not have dense ground-based radar network, many of these regions are covered by geostationary satellite. With the improved spatial and temporal resolutions of GOES-16 data, more information on convective clouds can be obtained. Using one-minute mesoscale sector data from GOES-16, LH profiles are obtained for convective clouds, and results adding these profiles are compared with adding LH from NEXRAD. When there is abundant radar data over land, LH from NEXRAD improves forecasts the most, but adding LH from GOES-16 is also shown some improvements. On the other hand, in the regions without radar data such as Gulf of Mexico, GOES LH can instead initiate convection over the region and improve the forecast.

CHAPTER 6: CONCLUSION

As the spatial resolution of forecast models become finer than a few kilometers, being able to resolve convective scale motion, a way to effectively assimilate observations at such fine spatial resolution has been sought in recent years. With improved resolution of the model grids, it has become harder to correctly initiate convection in the model. At NOAA, operational models use latent heating profiles derived from ground-based radars to initiate convection in the regional model, and adding observed heating profile has proven to be effective in improving precipitation forecasts. However, this is only done over land where ground-based radars are located, and not all continental regions have dense radar networks. This becomes an even larger issue as high resolution models are adapted for global domains. Therefore, this dissertation seeks a way to use visible and infrared channels from the current operational geostationary satellite, GOES-16, over the regions without radar data to initiate convection in forecast model as radar does today. As ground-based radars are used to find the location of convection, estimate latent heating in those regions, and finally uses the estimated heating to initiate convection in the detected convective regions, this dissertation follows the same procedure of how radars are used, and thus, consists of three main parts of convection detection, latent heating estimation, and applying estimated heating into the regional model. Since the main goal of the dissertation is to improve forecasts as in using ground-based radars, every part of the dissertation includes a comparison to the radar product.

The first paper proposed two methods to detect convection in early and mature stages using one-minute data from GOES-16. Convective clouds in the early stage grow vertically exhibiting decrease in T_b, while in the mature stage, the main feature of convective clouds is no

longer the T_b decrease, but a bubbling cloud top. One method was used for detecting early convection by measuring decreases in T_b over 10 minutes at two water vapor channels. A second method was used to detect mature convective clouds using features of convective clouds observed by GOES-16, such as bright reflectance, low brightness temperature, and lumpy cloud top surfaces. Reflectance at channel 2 and brightness temperature at channel 14 are used to set thresholds for reflectance and brightness temperature, and lumpiness of cloud top surface is calculated by applying the Sobel operator to the reflectance data. Even though using both methods showed comparable results to the radar product, several threshold values had to be determined. In order to avoid having to choose several thresholds, a machine learning model was applied to automate the process in the second paper.

Just as people can point out convective clouds by looking at loops of visible satellite imagery, machine learning model can learn by itself given enough training data. Since it has been shown from the first paper that high reflectance, low brightness temperature, and lumpy cloud top that are observed over time are useful to detect convection, five temporal data at channel 2 and 14 with two-minute intervals were used as inputs to the machine learning model, and MRMS PrecipFlag data are used as output. Encoder-decoder architecture was used for the model to take five images as input and produce one map of convective regions as output. More convective regions are detected using the machine learning model than the first paper, although different dates are used for validation. The model correctly looks at bubbling regions to detect convective clouds, but sometimes it assigns convection in the regions slightly displaced from the bubbling area because it also learned that there is a slight displacement in location that is observed due to different viewing angle from GOES-16 and ground-based radar.

The third paper dealt with estimating latent heating from GOES-16 and compared with existing radar products to examine how it differs from the existing products. Once convective regions were detected by the methods from the first paper, latent heating profiles for each convective cloud were assigned from a lookup table created with model simulations. These profiles were compared to latent heating derived by NEXRAD and DPR CSH product. GOES LH is similar to mean LH from CSH in terms of magnitude and vertical distribution of heating since they both use model simulations in the lookup table. On the other hand, LH from NEXRAD, as applied by the HRRR team, has different vertical profiles from the two that use model simulations, and the magnitude of mean LH is slightly smaller than GOES LH. However, once the total LH of each cloud is compared, the magnitude is similar between GOES-16 and NEXRAD as convective area detected by GOES-16 is smaller than the regions with reflectivity greater than 28dBZ, which is the threshold that HRRR uses to compute LH.

Lastly, the fourth paper examines impacts of using different LH products in initiating convection in the WRF model. Three experiments are run for a comparison: control, NEXRAD LH, and GOES LH. LH obtained from GOES-16 is added to the WRF model every 15 minutes as HRRR does with radar-derived LH, and the results are compared to the model initialized with radar-derived LH. Adding GOES LH shows improvements over the control experiment, and it even shows improvements over NEXRAD LH run in a case where radar data are limited. While LH from NEXRAD tends to effectively initiate convection and produce light rain in broader regions, LH from GOES tends to produce deeper convection once initiated. This would be attributed to different vertical shapes of LH and different size of convective regions defined by NEXRAD and GOES, as observed in Chapter 4. Even though it was only tested for two case

studies, it is presented as a proof-of-concept study that GOES-16 data may indeed be used to initiate convection.

REFERENCES

Afzali Gorooh, V., Kalia, S., Nguyen, P., Hsu, K. L., Sorooshian, S., Ganguly, S., & Nemani, R. R. (2020). Deep Neural Network Cloud-Type Classification (DeepCTC) Model and Its Application in Evaluating PERSIANN-CCS. *Remote Sensing*, *12*(2), 316. https://doi.org/10.3390/rs12020316

Ai, Y., Li, J., Shi, W., Schmit, T. J., Cao, C., & Li, W. (2017). Deep convective cloud characterizations from both broadband imager and hyperspectral infrared sounder measurements. *Journal of Geophysical Research: Atmospheres*, *122*(3), 1700-1712. https://doi.org/10.1002/2016JD025408

Autonès, F. & Moisselin, J.-M. (2013). Algorithm Theoretical Basis Document for "Rapid Development Thunderstorms. Scientific documentation of SAF/NWC PGE 11 (RDT) v2011, code SAF/NWC/CDOP/MFT/SCI/ATBD/11, available on http://www.nwcsaf.org/

Bankert, R. L., Mitrescu, C., Miller, S. D., & Wade, R. H. (2009). Comparison of GOES cloud classification algorithms employing explicit and implicit physics. *Journal of applied meteorology and climatology*, *48*(7), 1411-1421. https://doi.org/10.1175/2009JAMC2103.1

Bauer, P., Thorpe, A., & Brunet, G. (2015). The quiet revolution of numerical weather prediction. *Nature*, *525*(7567), 47-55. https://doi.org/10.1038/nature14956

Bedka, K., Brunner, J., Dworak, R., Feltz, W., Otkin, J., & Greenwald, T. (2010). Objective satellite-based detection of overshooting tops using infrared window channel brightness temperature gradients. *Journal of applied meteorology and climatology*, *49*(2), 181-202. https://doi.org/10.1175/2009JAMC2286.1

Bedka, K. M., Dworak, R., Brunner, J., & Feltz, W. (2012). Validation of satellite-based objective overshooting cloud-top detection methods using CloudSat cloud profiling radar observations. *Journal of applied meteorology and climatology*, *51*(10), 1811-1822. https://doi.org/10.1175/JAMC-D-11-0131.1

Bedka, K. M., & Khlopenkov, K. (2016). A probabilistic multispectral pattern recognition method for detection of overshooting cloud tops using passive satellite imager observations. *Journal of Applied Meteorology and Climatology*, *55*(9), 1983-2005. https://doi.org/10.1175/JAMC-D-15-0249.1

Bedka, K., Yost, C., Nguyen, L., Strapp, J. W., Ratvasky, T., Khlopenkov, K., ... & Palikonda, R. (2019). Analysis and Automated Detection of Ice Crystal Icing Conditions Using Geostationary Satellite Datasets and In Situ Ice Water Content Measurements. *SAE*

International Journal of Advances and Current Practices in Mobility, *2*(2019-01-1953), 35-57. https://doi.org/10.4271/2019-01-1953

Benjamin, S. G., Weygandt, S. S., Brown, J. M., Hu, M., Alexander, C. R., Smirnova, T. G., ... & Lin, H. (2016). A North American hourly assimilation and model forecast cycle: The Rapid Refresh. *Monthly Weather Review*, *144*(4), 1669-1694. https://doi.org/10.1175/MWR-D-15-0242.1

Beucler, T., Rasp, S., Pritchard, M., & Gentine, P. (2019). Achieving conservation of energy in neural network emulators for climate modeling. *arXiv preprint arXiv:1906.06622*.

Bonavita, M., Trémolet, Y., Holm, E., Lang, S. T., Chrust, M., Janisková, M., ... & Hamrud, M. (2017). A strategy for data assimilation. European Centre for Medium-Range Weather Forecasts. http://doi.org/10.21957/tx1epjd2p

Boukabara, S. A., Krasnopolsky, V., Stewart, J. Q., Maddy, E. S., Shahroudi, N., & Hoffman, R. N. (2019). Leveraging modern artificial intelligence for remote sensing and NWP: Benefits and challenges. *Bulletin of the American Meteorological Society*, *100*(12), ES473-ES491. https://doi.org/10.1175/BAMS-D-18-0324.1

Brenowitz, N. D., & Bretherton, C. S. (2018). Prognostic validation of a neural network unified physics parameterization. *Geophysical Research Letters*, *45*(12), 6289-6298. https://doi.org/10.1029/2018GL078510

Brunner, J. C., Ackerman, S. A., Bachmeier, A. S., & Rabin, R. M. (2007). A quantitative analysis of the enhanced-V feature in relation to severe weather. *Weather and Forecasting*, *22*(4), 853-872. https://doi.org/10.1175/WAF1022.1

Bu, J., Elhamod, M., Singh, C., Redell, M., Lee, W. C., & Karpatne, A. (2020). Learning Neural Networks with Competing Physics Objectives: An Application in Quantum Mechanics. *arXiv preprint arXiv:2007.01420*.

Bytheway, J. L., Kummerow, C. D., & Alexander, C. (2017). A features-based assessment of the evolution of warm season precipitation forecasts from the HRRR model over three years of development. *Weather and Forecasting*, *32*(5), 1841-1856. https://doi.org/10.1175/WAF-D-17-0050.1

Churchill, D. D., & Houze Jr, R. A. (1984). Development and structure of winter monsoon cloud clusters on 10 December 1978. *Journal of the atmospheric sciences*, *41*(6), 933-960. https://doi.org/10.1175/1520-0469(1984)041<0933:DASOWM>2.0.CO;2

Del Genio, A. D., Wu, J., & Chen, Y. (2012). Characteristics of mesoscale organization in WRF simulations of convection during TWP-ICE. *Journal of climate*, *25*(17), 5666-5688. https://doi.org/10.1175/JCLI-D-11-00422.1

DeMott, C. A. (1996). The vertical structure and modulation of TOGA COARE convection: A radar perspective (Order No. 9638671). Available from Dissertations & Theses @ Colorado State University; ProQuest Dissertations & Theses Global. (304296065). Retrieved from https://search-proquest-com.ezproxy2.library.colostate.edu/dissertations-theses/vertical-structure-modulation-toga-coare/docview/304296065/se-2?accountid=10223

Dworak, R., Bedka, K., Brunner, J., & Feltz, W. (2012). Comparison between GOES-12 overshooting-top detections, WSR-88D radar reflectivity, and severe storm reports. *Weather and Forecasting*, *27*(3), 684-699. https://doi.org/10.1175/WAF-D-11-00070.1

Geer, A., Ahlgrimm, M., Bechtold, P., Bonavita, M., Bormann, N., English, S., ... & Janisková, M. (2017). Assimilating observations sensitive to cloud and precipitation. European Centre for Medium-Range Weather Forecasts. httop://doi.org/10.21957/sz7cr1dym

Gentine, P., Pritchard, M., Rasp, S., Reinaudi, G., & Yacalis, G. (2018). Could machine learning break the convection parameterization deadlock?. *Geophysical Research Letters*, *45*(11), 5742-5751. https://doi.org/10.1029/2018GL078202

Gustafsson, N., Janjić, T., Schraff, C., Leuenberger, D., Weissmann, M., Reich, H., ... & Mile, M. (2018). Survey of data assimilation methods for convective-scale numerical weather prediction at operational centres. *Quarterly Journal of the Royal Meteorological Society*, *144*(713), 1218-1256. https://doi.org/10.1002/qj.3179

Hayatbini, N., Kong, B., Hsu, K. L., Nguyen, P., Sorooshian, S., Stephens, G., ... & Ganguly, S. (2019). Conditional Generative Adversarial Networks (cGANs) for Near Real-Time Precipitation Estimation from Multispectral GOES-16 Satellite Imageries—PERSIANN-cGAN. *Remote Sensing*, *11*(19), 2193. https://doi.org/10.3390/rs11192193

Hilburn, K. A., Ebert-Uphoff, I., & Miller, S. D. (2020). Development and Interpretation of a Neural Network-Based Synthetic Radar Reflectivity Estimator Using GOES-R Satellite Observations. *arXiv preprint arXiv:2004.07906*.

Hirose, H., Shige, S., Yamamoto, M. K., & Higuchi, A. (2019). High temporal rainfall estimations from Himawari-8 multiband observations using the random-forest machine-learning method. *Journal of the Meteorological Society of Japan. Ser. II*. https://doi.org/10.2151/jmsj.2019-040

Johnson, R. H. (1984). Partitioning tropical heat and moisture budgets into cumulus and mesoscale components: Implications for cumulus parameterization. *Monthly weather review*, *112*(8), 1590-1601.

Jones, C. D., & Macpherson, B. (1997). A latent heat nudging scheme for the assimilation of precipitation data into an operational mesoscale model. *Meteorological Applications: A journal of forecasting, practical applications, training techniques and modelling*, *4*(3), 269-277. https://doi.org/10.1017/S1350482797000522

Krasnopolsky, V. M., Fox-Rabinovitz, M. S., & Chalikov, D. V. (2005). New approach to calculation of atmospheric model physics: Accurate and fast neural network emulation of longwave radiation in a climate model. *Monthly Weather Review*, *133*(5), 1370-1383. https://doi.org/10.1175/MWR2923.1

Krasnopolsky, V. M., Fox-Rabinovitz, M. S., & Belochitski, A. A. (2013). Using ensemble of neural networks to learn stochastic convection parameterizations for climate and numerical weather prediction models from data simulated by a cloud resolving model. *Advances in Artificial Neural Systems*, *2013*. https://doi.org/10.1155/2013/485913

Kummerow, C., Barnes, W., Kozu, T., Shiue, J., & Simpson, J. (1998). The tropical rainfall measuring mission (TRMM) sensor package. *Journal of atmospheric and oceanic technology*, *15*(3), 809-817. https://doi.org/10.1175/1520-0426(1998)015<0809:TTRMMT>2.0.CO;2

Lee, S., Han, H., Im, J., Jang, E., & Lee, M. I. (2017). Detection of deterministic and probabilistic convection initiation using Himawari-8 Advanced Himawari Imager data. https://doi.org/10.5194/amt-10-1859-2017

Lee, Y., Kummerow, C. D., & Zupanski, M. (2020a). A simplified method for the detection of convection using high resolution imagery from GOES-16. Submitted to *Atmospheric Measurement Techniques.*

Lee, Y., Kummerow, C. D., & Ebert-Uphoff, I. (2020b). Applying machine learning methods to detect convection using GOES-16 ABI data. Submitted to *Atmospheric Measurement Techniques.*

LeMone, M. A., & Zipser, E. J. (1980). Cumulonimbus vertical velocity events in GATE. Part I: Diameter, intensity and mass flux. *Journal of the Atmospheric Sciences*, *37*(11), 2444-2457. https://doi.org/10.1175/1520-0469(1980)037<2444:CVVEIG>2.0.CO;2

Levizzani, V., Kidd, C., Kirschbaum, D. B., Kummerow, C. D., Nakamura, K., & Turk, F. J. (2020). *Satellite Precipitation Measurement*. Springer. http://doi.org/10.1007/978-3-030-24568-9

Liu, Q., Li, Y., Yu, M., Chiu, L. S., Hao, X., Duffy, D. Q., & Yang, C. (2019). Daytime rainy cloud detection and convective precipitation delineation based on a deep neural Network method using GOES-16 ABI images. *Remote Sensing*, *11*(21), 2555. https://doi.org/10.3390/rs11212555

Mahajan, S., & Fataniya, B. (2019). Cloud detection methodologies: Variants and development—a review. *Complex & Intelligent Systems*, 1-11. https://doi.org/10.1007/s40747-019-00128-0

Mecikalski, J. R., & Bedka, K. M. (2006). Forecasting convective initiation by monitoring the evolution of moving cumulus in daytime GOES imagery. *Monthly Weather Review*, *134*(1), 49-78. https://doi.org/10.1175/MWR3062.1

Mecikalski, J. R., MacKenzie Jr, W. M., Koenig, M., & Muller, S. (2010). Cloud-top properties of growing cumulus prior to convective initiation as measured by Meteosat Second Generation. Part I: Infrared fields. *Journal of Applied Meteorology and Climatology*, *49*(3), 521-534. https://doi.org/10.1175/2009JAMC2344.1

Migliorini, S., Lorenc, A. C., & Bell, W. (2018). A moisture-incrementing operator for the assimilation of humidity-and cloud-sensitive observations: formulation and preliminary results. *Quarterly Journal of the Royal Meteorological Society*, *144*(711), 443-457. https://doi.org/10.1002/qj.3216

Minnis P. and Heck, P. W. (2012). GOES-R Advanced Baseline Imager (ABI) Algorithm theoretical basis document for nighttime cloud optical depth, cloud particle size, cloud ice water path, and cloud liquid water path. Available from: https://www.goes-r.gov/products/baseline-cloud-opt-depth.html

Müller, R., Haussler, S., & Jerg, M. (2018). The Role of NWP Filter for the Satellite Based Detection of Cumulonimbus Clouds. *Remote Sensing*, *10*(3), 386. https://doi.org/10.3390/rs10030386

Müller, R., Haussler, S., Jerg, M., & Heizenreder, D. (2019). A Novel Approach for the Detection of Developing Thunderstorm Cells. *Remote Sensing*, *11*(4), 443. https://doi.org/10.3390/rs11040443

O'Gorman, P. A., & Dwyer, J. G. (2018). Using machine learning to parameterize moist convection: Potential for modeling of climate, climate change, and extreme events. *Journal of Advances in Modeling Earth Systems*, *10*(10), 2548-2563. https://doi.org/10.1029/2018MS001351

Peckham, S. E., Smirnova, T. G., Benjamin, S. G., Brown, J. M., & Kenyon, J. S. (2016). Implementation of a digital filter initialization in the WRF Model and its application in the Rapid Refresh. *Monthly Weather Review*, *144*(1), 99-106. https://doi.org/10.1175/MWR-D-15-0219.1

Pincus, R., Patrick Hofmann, R. J., Anderson, J. L., Raeder, K., Collins, N., & Whitaker, J. S. (2011). Can fully accounting for clouds in data assimilation improve short-term forecasts by global models?. *Monthly Weather Review*, *139*(3), 946-957. https://doi.org/10.1175/2010MWR3412.1

Qi, Y., Zhang, J., & Zhang, P. (2013). A real-time automated convective and stratiform precipitation segregation algorithm in native radar coordinates. *Quarterly Journal of the Royal Meteorological Society*, *139*(677), 2233-2240. https://doi.org/10.1002/qj.2095

Rasp, S., Pritchard, M. S., & Gentine, P. (2018). Deep learning to represent subgrid processes in climate models. *Proceedings of the National Academy of Sciences*, *115*(39), 9684-9689. https://doi.org/10.1073/pnas.1810286115

Roebber, P. J. (2009). Visualizing multiple measures of forecast quality. *Weather and Forecasting*, *24*(2), 601-608. https://doi.org/10.1175/2008WAF2222159.1

Satoh, S., Noda, A., & Iguchi, T. (2001, July). Retrieval of latent heating profiles from TRMM radar data. In *Preprints, 30th Int. Conf. on Radar Meteorology, Munich, Germany, Amer. Meteor. Soc* (Vol. 6). Available online at https://ams.confex.com/ams/30radar/techprogram/paper_21763.htm

Scheck, L., Weissmann, M., & Bach, L. (2020). Assimilating visible satellite images for convective-scale numerical weather prediction: A case-study. *Quarterly Journal of the Royal Meteorological Society*. https://doi.org/10.1002/qj.3840

Schmit, T. J., Griffith, P., Gunshor, M. M., Daniels, J. M., Goodman, S. J., & Lebair, W. J. (2017). A closer look at the ABI on the GOES-R series. *Bulletin of the American Meteorological Society*, *98*(4), 681-698. https://doi.org/10.1175/BAMS-D-15-00230.1

Schumacher, C., Stevenson, S. N., & Williams, C. R. (2015). Vertical motions of the tropical convective cloud spectrum over Darwin, Australia. *Quarterly Journal of the Royal Meteorological Society*, *141*(691), 2277-2288. https://doi.org/10.1002/qj.2520

Seity, Y., Brousseau, P., Malardel, S., Hello, G., Bénard, P., Bouttier, F., ... & Masson, V. (2011). The AROME-France convective-scale operational model. *Monthly Weather Review*, *139*(3), 976-991. https://doi.org/10.1175/2010MWR3425.1

Setvák, M., Rabin, R. M., & Wang, P. K. (2007). Contribution of the MODIS instrument to observations of deep convective storms and stratospheric moisture detection in GOES and MSG imagery. *Atmospheric Research*, *83*(2-4), 505-518. https://doi.org/10.1016/j.atmosres.2005.09.015

Shige, S., Takayabu, Y. N., Tao, W. K., & Johnson, D. E. (2004). Spectral retrieval of latent heating profiles from TRMM PR data. Part I: Development of a model-based algorithm. *Journal of Applied Meteorology*, *43*(8), 1095-1113. https://doi.org/10.1175/1520-0450(2004)043<1095:SROLHP>2.0.CO;2

Shige, S., Takayabu, Y. N., Tao, W. K., & Shie, C. L. (2007). Spectral retrieval of latent heating profiles from TRMM PR data. Part II: Algorithm improvement and heating estimates over tropical ocean regions. *Journal of applied Meteorology and Climatology*, *46*(7), 1098-1124. https://doi.org/10.1175/JAM2510.1

Sieglaff, J. M., Cronce, L. M., Feltz, W. F., Bedka, K. M., Pavolonis, M. J., & Heidinger, A. K. (2011). Nowcasting convective storm initiation using satellite-based box-averaged cloud-

top cooling and cloud-type trends. *Journal of applied meteorology and climatology*, *50*(1), 110-126. https://doi.org/10.1175/2010JAMC2496.1

Steiner, M., Houze Jr, R. A., & Yuter, S. E. (1995). Climatological characterization of three-dimensional storm structure from operational radar and rain gauge data. *Journal of Applied Meteorology*, *34*(9), 1978-2007. https://doi.org/10.1175/1520-0450(1995)034<1978:CCOTDS>2.0.CO;2

Tao, W. K., Lang, S., Simpson, J., & Adler, R. (1993). Retrieval algorithms for estimating the vertical profiles of latent heat release. *Journal of the Meteorological Society of Japan. Ser. II*, *71*(6), 685-700. https://doi.org/10.2151/jmsj1965.71.6_685

Tao, W. K., Smith, E. A., Adler, R. F., Haddad, Z. S., Hou, A. Y., Iguchi, T., ... & Meneghini, R. (2006). Retrieval of latent heating from TRMM measurements. *Bulletin of the American Meteorological Society*, *87*(11), 1555-1572. https://doi.org/10.1175/BAMS-87-11-1555

Tao, W. K., Takayabu, Y. N., Lang, S., Shige, S., Olson, W., Hou, A., ... & Krishnamurti, T. (2016). TRMM latent heating retrieval: Applications and comparisons with field campaigns and large-scale analyses. *Meteorological Monographs*, *56*, 2-1. https://doi.org/10.1175/AMSMONOGRAPHS-D-15-0013.1

Tao, W. K., Iguchi, T., & Lang, S. (2019). Expanding the Goddard CSH algorithm for GPM: New extratropical retrievals. *Journal of Applied Meteorology and Climatology*, *58*(5), 921-946. https://doi.org/10.1175/JAMC-D-18-0215.1

Petković, V., Orescanin, M., Kirstetter, P., Kummerow, C., & Ferraro, R. (2019). Enhancing PMW Satellite Precipitation Estimation: Detecting Convective Class. *Journal of Atmospheric and Oceanic Technology*, *36*(12), 2349-2363. https://doi.org/10.1175/JTECH-D-19-0008.1

Weygandt, S. S., Alexander, C. R., Dowell, D. C., Hu, M., James, E. P., Benjamin, S. G., ... & Olson, J. B. (2016). Radar data assimilation impacts in the RAP and HRRR models, 20th Conf. on Integrated Observing and Assimilation Systems for the Atmosphere, Oceans, and Land Surface (IOAS-AOLS), New Orleans, Louisiana, United States, Amer. Meteor. Soc., 10-14 January 2016. Available online at https://ams.confex.com/ams/96Annual/webprogram/Paper289787.html

Wu, J., Del Genio, A. D., Yao, M. S., & Wolf, A. B. (2009). WRF and GISS SCM simulations of convective updraft properties during TWP-ICE. *Journal of Geophysical Research: Atmospheres*, *114*(D4). https://doi.org/10.1029/2008JD010851

Xu, K. M., & Randall, D. A. (2001). Updraft and downdraft statistics of simulated tropical and midlatitude cumulus convection. *Journal of the atmospheric sciences*, *58*(13), 1630-1649. https://doi.org/10.1175/1520-0469(2001)058<1630:UADSOS>2.0.CO;2

Yanai, M., Esbensen, S., & Chu, J. H. (1973). Determination of bulk properties of tropical cloud clusters from large-scale heat and moisture budgets. *Journal of the Atmospheric Sciences*, *30*(4), 611-627. https://doi.org/10.1175/1520-0469(1973)030<0611:DOBPOT>2.0.CO;2

Yang, S., & Smith, E. A. (1999). Moisture budget analysis of TOGA COARE area using SSM/I-retrieved latent heating and large-scale Q 2 estimates. *Journal of Atmospheric and Oceanic Technology*, *16*(6), 633-655. https://doi.org/10.1175/1520-0426(1999)016<0633:MBAOTC>2.0.CO;2

Yano, J. I., Ziemiański, M. Z., Cullen, M., Termonia, P., Onvlee, J., Bengtsson, L., ... & Homar, V. (2018). Scientific challenges of convective-scale numerical weather prediction. *Bulletin of the American Meteorological Society*, *99*(4), 699-710. https://doi.org/10.1175/BAMS-D-17-0125.1

Zhang, J., Langston, C., & Howard, K. (2008). Brightband identification based on vertical profiles of reflectivity from the WSR-88D. *Journal of Atmospheric and Oceanic Technology*, *25*(10), 1859-1872. https://doi.org/10.1175/2008JTECHA1039.1

Zhang, J., & Qi, Y. (2010). A real-time algorithm for the correction of brightband effects in radar-derived QPE. *Journal of Hydrometeorology*, *11*(5), 1157-1171. https://doi.org/10.1175/2010JHM1201.1

Zhang, J., Howard, K., Langston, C., Kaney, B., Qi, Y., Tang, L., ... & Arthur, A. (2016). Multi-Radar Multi-Sensor (MRMS) quantitative precipitation estimation: Initial operating capabilities. *Bulletin of the American Meteorological Society*, *97*(4), 621-638. https://doi.org/10.1175/BAMS-D-14-00174.1

Zinner, T., Mannstein, H., & Tafferner, A. (2008). Cb-TRAM: Tracking and monitoring severe convection from onset over rapid development to mature phase using multi-channel Meteosat-8 SEVIRI data. *Meteorology and Atmospheric Physics*, *101*(3-4), 191-210. https://doi.org/10.1007/s00703-008-0290-y

Zinner, T., Forster, C., De Coning, E., & Betz, H. D. (2013). Validation of the Meteosat storm detection and nowcasting system Cb-TRAM with lightning network data-Europe and South Africa. *Atmospheric Measurement Techniques*, *6*(6), 1567. https://doi.org/10.5194/amt-6-1567-2013

Zipser, E. J., & Lutz, K. R. (1994). The vertical profile of radar reflectivity of convective cells: A strong indicator of storm intensity and lightning probability?. *Monthly Weather Review*, *122*(8), 1751-1759. https://doi.org/10.1175/1520-0493(1994)122<1751:TVPORR>2.0.CO;2

APPENDIX A

Table A1. Model summary of the encoder-decoder model.

Layer	Output shape	Param #	Connected to
Input_1	(None, 128, 128, 5)	0	
Conv2d_1	(None, 128, 128, 16)	736	Input_1
Batch_normalization_1	(None, 128, 128, 16)	64	Conv2d_1
Conv2d_2	(None, 128, 128, 16)	2320	Batch_normalization_1
Batch_normalization_2	(None, 128, 128, 16)	64	Conv2d_2
Max_pooling2d_1	(None, 64, 64, 16)	0	Batch_normalization_2
Conv2d_3	(None, 64, 64, 32)	4640	Max_pooling2d_1
Batch_normalization_3	(None, 64, 64, 32)	128	Conv_2d_3
Conv2d_4	(None, 64, 64, 32)	9248	Batch_normalization_3
Batch_normalization_4	(None, 64, 64, 32)	128	Conv2d_4
Max_pooling2d_2	(None, 32, 32, 32)	0	Batch_normalization_4
Input_2	(None, 32, 32, 5)	0	
Concatenate_1	(None, 32, 32, 37)	0	Maxpooling2d_2 Input_2
Conv2d_5	(None, 32, 32, 64)	21376	Concatenate_1
Batch_normalization_5	(None, 32, 32, 64)	256	Conv2d_5
Conv2d_6	(None, 32, 32, 64)	36928	Batch_normalization_5
Batch_normalization_6	(None, 32, 32, 64)	256	Conv2d_6
Max_pooling2d_3	(None, 16, 16, 64)	0	Batch_normalization_6
Conv2d_7	(None, 16, 16, 128)	73856	Max_pooling2d_3
Batch_normalization_7	(None, 16, 16, 128)	512	Conv2d_7
Conv2d_8	(None, 16, 16, 128)	147584	Batch_normalization_7
Batch_normalization_8	(None, 16, 16, 128)	512	Conv2d_8
Max_pooling2d_4	(None, 8, 8, 128)	0	Batch_normalization_8
Conv2d_9	(None, 8, 8, 128)	147584	Max_pooling2d_4
Batch_normalization_9	(None, 8, 8, 128)	512	Conv2d_9
Conv2d_10	(None, 8, 8, 128)	147584	Batch_normalization_9
Batch_normalization_10	(None, 8, 8, 128)	512	Conv2d_10
Up_sampling2d_1	(None, 16, 16, 128)	0	Batch_normalization_10
Conv2d_11	(None, 16, 16, 64)	73792	Up_sampling2d_1
Batch_normalization_11	(None, 16, 16, 64)	256	Conv2d_11
Conv2d_12	(None, 16, 16, 64)	36928	Batch_normalization_11
Batch_normalization_12	(None, 16, 16, 64)	256	Conv2d_12
Up_sampling2d_2	(None, 32, 32, 64)	0	Batch_normalization_12
Conv2d_13	(None, 32, 32, 32)	51243	Up_sampling2d_2
Batch_normalization_13	(None, 32, 32, 32)	128	Conv2d_13
Conv2d_14	(None, 32, 32, 32)	25632	Batch_normalization_13
Batch_normalization_14	(None, 32, 32, 32)	128	Conv2d_14

Up_sampling2d_3	(None, 64, 64, 32)	0	Batch_normalization_14
Conv2d_15	(None, 64, 64, 16)	12816	Up_sampling2d_3
Batch_normalization_15	(None, 64, 64, 16)	64	Conv2d_15
Conv2d_16	(None, 64, 64, 16)	6416	Batch_normalization_15
Batch_normalization_16	(None, 64, 64, 16)	64	Conv2d_16
Conv2d_transpose_1	(None, 128, 128, 1)	145	Batch_normalization_16

Table A2. POD, FAR, SR, and CSI values for using different thresholds in the two-step training model.

Threshold	POD	FAR	SR	CSI
0.05	0.94298559	0.535044175	0.464955825	0.4522424
0.1	0.913858215	0.456447233	0.543552767	0.517060558
0.15	0.887655352	0.398784349	0.601215651	0.558702899
0.2	0.85875747	0.348113473	0.651886527	0.588760871
0.25	0.834369835	0.312095964	0.687904036	0.605253444
0.3	0.798756916	0.269845006	0.730154994	0.616706239
0.35	0.769121649	0.240217357	0.759782643	0.618677759
0.4	0.743219236	0.21689681	0.78310319	0.616344624
0.45	0.712533049	0.194027871	0.805972129	0.608205409
0.5	0.686385805	0.176749293	0.823250707	0.598228029
0.55	0.659030631	0.159993321	0.840006679	0.585532586
0.6	0.633640923	0.146901862	0.853098138	0.571304851
0.65	0.607174665	0.133743247	0.866256753	0.555134673
0.7	0.580303795	0.121656374	0.878343626	0.53713138
0.75	0.551572206	0.110995861	0.889004139	0.516034904
0.8	0.523822546	0.101982567	0.898017433	0.49441128
0.85	0.501165661	0.095021454	0.904978546	0.476111856
0.9	0.481326022	0.088852528	0.911147472	0.459746639
0.95	0.45801003	0.080131638	0.919868362	0.44043737

Table A3. POD, FAR, SR, and CSI values for using different thresholds in the standard training model.

Threshold	POD	FAR	SR	CSI
0.05	0.942117438	0.540193427	0.459806573	0.447173927
0.1	0.894713617	0.429747339	0.570252661	0.534392221
0.15	0.855999591	0.363530845	0.636469155	0.574913234
0.2	0.803875684	0.291727494	0.708272506	0.603916012
0.25	0.755258694	0.238557529	0.761442471	0.610744279
0.3	0.683399631	0.180284591	0.819715409	0.59410355
0.35	0.627938452	0.146008324	0.853991676	0.567059181
0.4	0.580581814	0.121687532	0.878312468	0.537357899
0.45	0.534164411	0.103516198	0.896483802	0.503131513
0.5	0.419381773	0.070663682	0.929336318	0.406421632
0.55	0.358005307	0.056815544	0.943184456	0.350447719
0.6	0.305014843	0.046418477	0.953581523	0.300552384
0.65	0.255235442	0.037863312	0.962136688	0.252697257
0.7	0.205429901	0.032025597	0.967974403	0.204043085
0.75	0.158849869	0.031320871	0.968679129	0.158038156
0.8	0.126544575	0.033665056	0.966334944	0.125989146
0.85	0.099957158	0.037122494	0.962877506	0.09957343
0.9	0.070457093	0.046153482	0.953846518	0.070217708
0.95	0.034891193	0.080737421	0.919262579	0.034784597